TRIBHUVAN UNIVERSITY
INSTITUTE OF ENGINEERING
PULCHOWK CAMPUS

B-07-BAS-2019/24

EXPERIMENTAL INVESTIGATION OF FLOW OVER A CYLINDER AND WING WITH VORTEX GENERATORS USING PIV

By:
Kshitish Chandra Devkota (076BAS018)
Praphul Mishra (076BAS027)
Sandip Adhikari (076BAS035)
Shreeju Banjade (076BAS041)

A PROJECT REPORT TO THE DEPARTMENT OF MECHANICAL AND AEROSPACE ENGINEERING IN PARTIAL FULFILLMENT OF THE REQUIREMENT FOR THE BACHELOR'S DEGREE IN AEROSPACE ENGINEERING

DEPARTMENT OF MECHANICAL AND AEROSPACE ENGINEERING
LALITPUR, NEPAL

March, 2024

COPYRIGHT

TRIBHUVAN UNIVERSITY
INSTITUTE OF ENGINEERING
CENTRAL CAMPUS PULCHOWK
DEPARTMENT OF MECHANICAL AND AEROSPACE ENGINEERING

The undersigned certify that they have read, and recommended to the Institute of Engineering for acceptance, a project report entitled **"Experimental Investigation of Flow over a Cylinder and Wing with Vortex Generators using PIV"** submitted by Kshitish Chandra Devkota, Praphul Mishra, Sandip Adhikari and Shreeju Banjade in partial fulfillment of the requirements for the degree of Bachelor of Aerospace Engineering.

.....

Supervisor, Er. Kamal Darlami
Assistant Professor and Deputy Head of Department
Department of Mechanical and Aerospace Engineering
Institute of Engineering, Pulchowk Campus

.....

External Examiner, Er. Ashish Manandhar
MPC Engineer
Himalaya Airlines

.....

Head of Department, Dr. Sudip Bhattrai
Assistant Professor
Department of Mechanical and Aerospace Engineering
Institute of Engineering, Pulchowk Campus

Date:12th March, 2024

ABSTRACT

Particle Image Velocimetry (PIV) is a non intrusive flow measurement technique used for qualitative and quantitative analysis of flow dynamics. In this study, PIV is employed to investigate flow behaviour around a circular cylinder and a wing, with and without vortex generators (VGs). The research pursues dual objectives: to characterize the PIV setup using the Strouhal number (a dimensionless parameter) and to analyze flow characteristics, particularly focusing on stall conditions. Systematically, a linear actuation mechanism is developed to facilitate experimentation on both models. Image processing, conducted in PIVLab alongside the development of necessary code written in MATLAB, are incorporated for detailed analysis, with time-dependent signals transformed into the frequency domain using Fast Fourier Transform (FFT) for comprehensive evaluation. The characterization of existing PIV setup was done through three sets of experimental data using strouhal number for analysis of flow around circular cylinder. The strouhal number obtained are 0.1897, 0.1952 and 0.1952 with 3.6777 %, 0.9137 % and 0.9137 % errors respectively. Velocity field and vorticity contours were studied for the aerodynamic flow analysis of baseline wing and wing with VG at the 15 degree angle of attack. The obtained Strouhal number for wing and wing with VGs are 0.1381 and 0.1571 respectively. The comparison concludes that vortex generators energize the boundary layer above the wing and delay the flow separation.

KEYWORDS: PIV, Vortex generator, Image Processing, Circular Cylinder, Strouhal Number, Vortex Shedding

ACKNOWLEDGEMENT

We would like to express our heartfelt gratitude to the **Department of Mechanical and Aerospace Engineering, IOE Pulchowk Campus** for the delightful opportunity provided to pursue our field of interest as the final year project, highlighting the use of PIV for flow study past a circular cylinder and wing.

We would also like to express our sincere gratitude to our supervisor, Deputy Head of Department, **Asst. Prof. Kamal Darlami** for the constant support, encouragement, and positive zeal throughout the time period & for providing the workspace for our experimentation at **Incubation, Innovation and entrepreneurship Center (IIEC)**. The constant guidance along with the provision of high-end equipment for our project facilitation has been immensely helpful to conduct the experiments. We would also like to express our thanks to our Head Of Department, **Asst. Prof. Sudip Bhattrai** for his assistance and support during the project. We would also like to thank **Asst. Prof. Neeraj Adhikari** for his willingness to assist us with the project from the very beginning. We would also like to extend our gratitude to **Mr. Salim Maharjan** and **Mr. Anup Pandey** for their continuous support throughout the project.

Additionally, we would also like to express our sincere gratitude to **Prof. Dr. Debopam Das** for his willingness to assist us with the provision of hollow glass spheres as seeding particles from the subsonic lab in IIT Kanpur.

Lastly, we are also grateful to our seniors, teachers and friends for their continuous support in various phases during the project.

TABLE OF CONTENTS

List of Figures

List of Tables

LIST OF ACRONYMS AND ABBREVATIONS

3D	Three Dimensional
AR	Aspect Ratio
BR	Blockage Ratio
CATIA	Computer Aided Three-Dimensional Interactive Application
CFD	Computational Fluid Dynamics
CNC	Computer Numerical Control
DCC	Direct Cross Correlation
DFT	Discrete Fourier Transform
FFT	Fast Fourier Transform
HD	High Definition
HVAC	Heating Ventilation and Air-Conditioning
ITTC	International Towing Tank Conference
LEV	Leading Edge Vortex
NACA	National Advisory Committee for Aeronautics
PIV	Particle Image Velocimetry
PSD	Power Spectral Density
TEV	Trailing Edge Vortex
VG	Vortex Generator

SYMBOLS

b	Span
$C(m,n)$	Discrete correlation function
C_s	Scattering cross section
g	Acceleration due to gravity
H	Shape factor
h	Vortex generator height
I_0	Intensity
m_p	Mass of seeding particle
P_s	Scattering power
p	pressure force
S	Source term
S_{Mx}	Source of x-momentum per unit volume
S_{My}	Source of y-momentum per unit volume
S_{Mz}	Source of z-momentum per unit volume
St	Strouhal Number
Stk	Stokes Number
t	Threshold
U	Velocity
u	x-direction velocity
v	y-direction velocity
V_T	Settling time
w	x-direction velocity
x	x-direction
xh	Horizontal distance
y	y-direction
Re_x	Reynolds Number
δ_{99}	99% Boundary layer thickness
δ^*	Displacement thickness
δ	Boundary layer thickness
θ	Momentum thickness
λ	Wavelength
μ	Dynamic Viscosity

ν	Kinematic Viscosity
ρ_f	Density of fluid
ρ_p	Density of particle
τ	Relaxation time
τ_{ij}	Stress component acting in j direction on a surface normal to i direction

CHAPTER ONE: INTRODUCTION

1.1. Background

The aerodynamic performance of a wing depends on multiple complex characteristics along with its general structure. One of the major issues which adversely affects the aerodynamic performance of a wing is the flow separation near the rear of the body which results in generation of wakes. On an aircraft wing, the flow separation occurs when the boundary-layer travels far enough against an adverse pressure gradient. This results in reversed flow and thickening of the boundary layer downstream of the separation point. This separation generally results in low velocity wake downstream of the body. To counteract this particular adversity, VGs are introduced near the leading edge of the airfoil. VGs are passive control devices that improve the performance of the airfoil by energizing the boundary layer around the airfoil and delaying the flow separation[1].

The analysis of flow field over the surface of the wing with and without the presence of VGs effectively aids in the research field to study the aerodynamic parameters such as velocity fields, vorticity contour, circulation of vortex structures and sectional lift coefficient. To analyze the flow characteristics, PIV is one of the most commonly used flow visualization techniques. The PIV is a non-intrusive flow measurement technique that utilizes tracer particles to track fluid flow velocity. The high-speed camera captures images at different time frames and cross-correlation methods are used to determine the location of tracer particles at different time frames to calculate the displacement[2].

External flows around bluff bodies, such as circular cylinders, are extensively studied due to their significant influence on engineering structure design. Despite its apparent simplicity, the flow past a cylinder poses challenges in fluid mechanics, characterized by phenomena like vortex shedding, unsteady pressure fields, and fluctuating aerodynamic forces. These complexities are influenced by factors including Reynolds number, turbulence intensity, and geometric parameters.[3]. This study aims to comprehensively characterize and quantify the PIV setup using the Strouhal number, focusing on its sub-critical region below 0.21, indicative of specific vortex shedding characteristics. [4]
The incentive of the research is to observe and investigate the flow characteristics and vortex formation over the streamwise direction of the wing. To evaluate the flow characteristics in two different scenarios, the analysis of the flow field over the wing was conducted both with and without VGs through PIV technique in low Reynolds number.

1.2. Problem Statement

The problem statement for this particular project is to modify the existing PIV setup, for proper characterization, to conduct experiments at low Reynolds number. The project aims to investigate the flow around the circular cylinder (for setup characterization) and the effect of VGs on flow around the wing and wing with VGs using PIV. The analysis provides insight into the flow past the bluff body (cylinder) and the role of VGs in delaying the onset of flow separation that mitigates the adverse effects accompanying it.

1.3. Objective

1.3.1. Main Objective

To investigate the flow over a cylinder and wing with VGs using PIV.

1.3.2. Specific Objectives

1. To develop a fully functional linear actuation mechanism for PIV analysis.
2. To characterize the PIV setup for experimental analysis using circular cylinder through Strouhal number.
3. To visualize and analyze the flow characteristics around the wing with and without VGs at stall angle of attack.

1.4. System Requirements

1.4.1. Hardware Requirements

1. Camera
2. Class IIIA and IIIB Laser
3. Hollow glass spheres as tracer particles
4. Stepper Motor
5. Resin Printer
6. Other electronic components such as jumper wire, motor driver module, micro-controller.

1.4.2. Software Requirements

1. MATLAB with installed PIVLAB
2. ANSYS
3. CATIA
4. ARDUINO IDE
5. SOLIDWORKS
6. ITEMCAD
7. HALOT BOX

1.5. Applications

1. Flow past a circular cylinder is used in structural engineering for mitigating vortex-induced vibrations, drag, and lift forces in chimney stacks, bridges, ships, buildings, and towers.
2. The VGs are useful for the delay of boundary layer formation by energizing the boundary layer which remains useful for increase in lift and efficiency.
3. VGs can be used in aerodynamic research to analyze and investigate boundary layer behavior, flow separation control mechanism and stall delay.
4. VGs are utilized in building ships for the control of flow separation over hulls, propellers and rudders for increase in maneuverability leading to improved hydrodynamic performance.
5. The VGs are introduced in wind turbines for reduction of flow separation which are also known as smart blades.
6. VGs improve the flow distribution in Heating, Ventilation and air conditioning (HVAC) systems and also reduce the energy consumption by enhancing heat exchange efficiency.

1.6. Feasibility analysis

1.6.1. Economic Feasibility

The cost estimation for the fabrication of the circular cylinder, baseline wing, and the wing with VGs along with the resources needed for modifying the PIV setup and conducting experiments is about Rs. 25000. The calculated cost estimation reveals that the research is economically feasible.

1.6.2. Technical Feasibility

The availability of software for the design and analysis of components as well as the local availability of 3D resin printer for the fabrication of test specimen makes the research technically feasible. The availability of PIV tank setup, for the analysis of flow characteristics, further proves that the research is technically viable. However, the local unavailability of seeding particles might produce initial challenges.

1.6.3. Operational Feasibility

The design and fabrication of wing along with the utilization of PIV for the research analysis requires very basic and general concepts regarding the principle of PIV, and basic knowledge along with simple hands-on experience of the manufacturing process through resin molding for the fabrication of wing. The post-processing of images will also be done through software such as PIVLAB which makes the project operationally viable.

CHAPTER TWO: LITERATURE REVIEW

2.1. Vortex Generator

Vortex generators (VGs) are common passive flow control devices that are utilized to delay flow separation in many engineering applications due to their geometrical simplicity and great performance, as discussed by Liu [5]. Taylor discovered that streamwise vortices formed by small vane VGs boost near-wall momentum by transferring momentum from the outer flow to the near wall region [6].The shape of the vortex generator is critical. VGs come in a variety of shapes, including triangular, trapezoidal, rectangular, wishbone, and doublet.

Godard and Stanislas conducted the parametric study of triangular and rectangular VGs. The parameters include angle of attack, length , transverse distance.[2]. They concluded that the triangular vortex generator produces significantly less drag. Velte, Hansen and Cavar conducted the flow field measurement downstream of the triangular vortex generator. They found that the counter-rotating vortices produced by VGs extended the region of reversed flow at the downstream of the model.[7].

Velte et al. carried out wake measurement in a wind tunnel and visualized flow in a water tunnel via a rectangular vortex generator in a laminar boundary layer [8]. They discovered that the vortical structure in the wake downstream of the vortex generator was far more complex than a simple tip vortex structure. Yanagihara and Torii demonstrated that the longitudinal vortices surrounding the triangle vortex generator were made up of the main vortex, corner vortices, and the induced secondary vortex [9]. Velte et al. [8] and Yanagihara and Torii [9] demonstrated that a vortex generator generated various vortices in the laminar boundary layer.

VGs generate small streamwise vortices that energize near wall boundary layer because of which the flow is attached to the wing surface. This gives advantage of producing lift even at low Re. Also, it delays the boundary layer separation.[1].

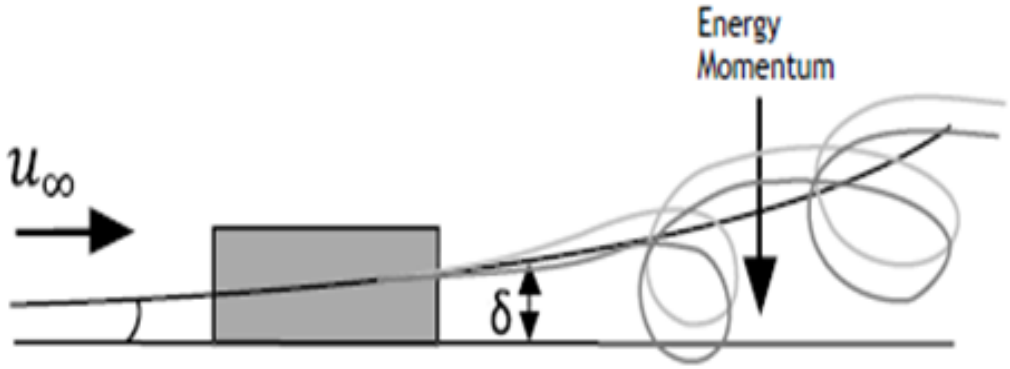

Figure 2.1: Boundary layer motion alteration by a rectangular Vortex Generator [1]

2.2. Vortex Generator Geometry

Passive control methods often utilize VGs, which are small plates or airfoils of various shapes and sizes attached to the airfoil wall and immersed in the boundary layer, typically upstream of the separation point. These devices can be arranged in rows along the spanwise direction of the airfoil with a yaw angle (β) relative to the mean flow direction, generating streamwise trailing vortices. VGs are commonly rectangular or triangular in shape, with a height on the order of the boundary layer thickness (δ). They can be configured to produce either co-rotating or counter-rotating vortices.

One limitation of passive VGs is that they are effective only within a specific range of fluid flow conditions. Therefore, their design needs to be optimized for particular applications where the separation location is relatively fixed and not too far from the VGs. Due to the drag penalty associated with passive devices, many optimization studies have focused on reducing the height (h) of the VGs, from being on the order of the boundary layer thickness (δ) to only a fraction of it.[10]

Conventional passive VGs are vane-type devices with a height (h) roughly equal to the boundary-layer thickness (δ). They have been widely employed to manage flow separation by enhancing near-wall momentum through momentum transfer from the outer (free-stream) flow to the wall region.

In the 1970s, Kuethe introduced and studied non-traditional wave-type VGs with a lower profile, where the height-to-thickness ratio (h/δ) was between 0.27 and 0.42. These VGs utilize the Taylor–Goertler instability to generate streamwise vortices within the boundary layer, particularly effective when the fluid flows over a concave surface. These low-profile

VGs have shown success in reducing the intensity of acoustic disturbances in the wake region by inhibiting the formation of the Karman vortex street and decreasing the area of velocity deficit in the wake. [11]

VGs with a height-to-boundary-layer thickness ratio ($\frac{h}{\delta}$) of less than or equal to 0.625 have shown the potential to outperform conventional VGs with $\frac{h}{\delta}$ around 1, primarily due to their significantly lower drag. Several studies have demonstrated that low-profile VGs, with a height much smaller than that of traditional vane-type VGs ($0.1 \leq \frac{h}{\delta} \leq 0.5$), can still effectively transfer momentum towards the wall over a region several times their own height, thereby controlling flow separation.

In addition to their lower drag, these low-profile VGs offer other advantages over larger conventional VGs, such as being more compact, which allows them to be stored within the wing when not in use (e.g., on slotted flaps), and having a reduced radar cross-section.[12]

2.3. Boundary layer

2.3.1. Laminar Boundary Layer

The laminar boundary layer theory is well-established, specifically when considering a flat plate without any pressure gradient. A precise solution, referred to as the Blasius solution , exists for this particular scenario. The Blasius solution provides equations 2.1, 2.2, and 2.3, which are crucial in analyzing the flow. The displacement thickness represents the outward displacement of the hypothetical flow's wall necessary to maintain the mass flux without friction. The momentum thickness indicates the amount of momentum lost within the boundary layer flow. Lastly, the shape factor is the ratio between the two measures and helps determine whether the flow is laminar or turbulent [13]. In the case of the Blasius solution, 99% boundary layer thickness is defined as:

$$\delta_{99} = \frac{4.92xh}{Re_{x\frac{1}{2}}} \tag{2.1}$$

The displacement thickness is given as:

$$\delta^* = 1.72\sqrt{\frac{vxh}{U}} \tag{2.2}$$

The momentum thickness is given as:

$$\theta = 0.644\sqrt{\frac{vxh}{U}} \tag{2.3}$$

The shape factor is given as:

$$H = \frac{\delta}{\theta} = 2.67 \tag{2.4}$$

2.3.2. Transition

Once the laminar-to-turbulent transition initiates in a boundary layer, the applicability of the Blasius solution diminishes. Transition mechanisms include laminar instability or deliberate induction. Transition location is important, especially for airfoils where downstream transition minimizes drag. VGs delay transition, while boundary layer trip mechanisms can induce transition at specific locations to control flow separation. Figure 2.2 illustrates transitional flow over a flat plate, depicting the transition process steps.[13]. The location of transition can be seen near the end of the flow, right before the onset of turbulence.

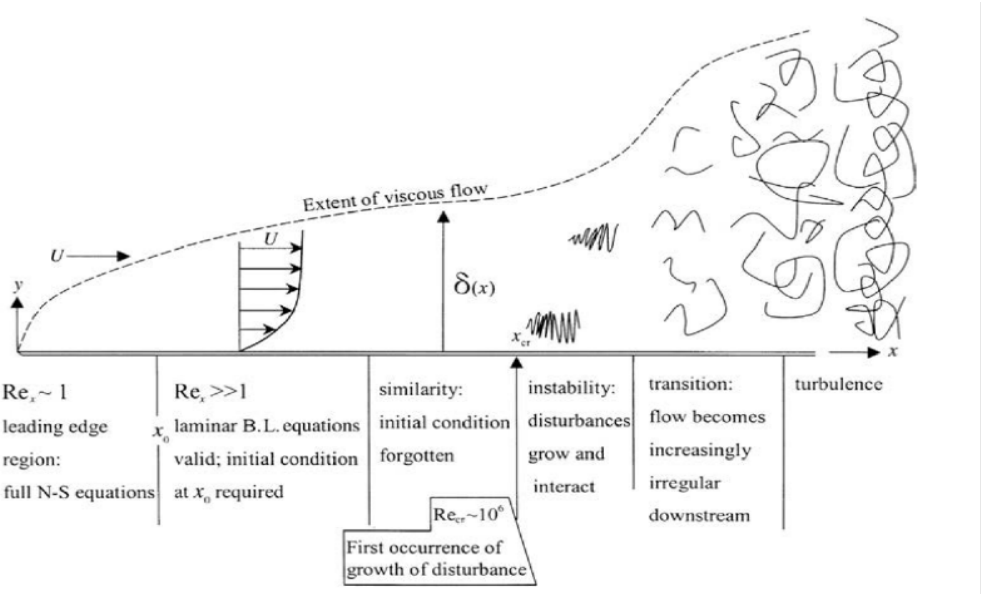

Figure 2.2: Schematic of flow over a flat plate [13]

2.3.3. Turbulent Boundary Layer

The transition from laminar to turbulent flow occurs when there is a disruption within the flow or when the Reynolds number reaches a sufficiently high value (the specific Reynolds

number at which this transition happens varies depending on the flow conditions). In most cases involving aircraft wings, laminar flow is more favorable than turbulent flow. This preference arises because turbulent boundary layers tend to be thicker and generate greater skin friction drag. However, as discussed in the section on transition, a turbulent boundary layer has a lower tendency to separate and can be advantageous in situations where the objective is to prevent separation [1].

2.3.4. Boundary Layer Thickness estimation using XFOIL

The Boundary layer thickness for flow over a streamlined body has been estimated using xfoil[14]. XFOIL calculates the boundary layer parameters such as displacement thickness (δ_*), momentum thickness (θ) and transition locations. Using this information, laminar and turbulent boundary layer thicknesses can be calculated. Equation 2.5 gives the laminar boundary layer thickness whereas 2.6 gives the turbulent boundary layer thickness[14].

$$\delta = 2.9\delta_* \tag{2.5}$$

$$\delta = \theta(3.15 + (\frac{1.72}{H-1})) + \delta_* \tag{2.6}$$

2.4. Unsteady Flow Past a Circular Cylinder

A circular cylinder generally represents behaviour of wakes behind bluff bodies and it has also a very simple geometry, therefore flow past a cylinder has been a method for the validation of PIV setup characterization.

2.4.1. Regime of Flow

One of the non dimensionless hydrodynamic numbers that is used to describe the flow around a smooth circular cylinder is the Reynolds number (Re). By the definition, the Reynolds number is the ratio of the inertia forces to viscous forces and formulated as:

$$\mathrm{Re} = \frac{\rho U D}{\mu} \tag{2.7}$$

where ρ is the density of fluid, D is the diameter of the cylinder, U is the flow velocity, and

μ is the dynamic viscosity of the fluid.

Flow regimes are obtained as the result of tremendous changes of the Reynolds number. The changes of the Reynolds number create separation flows in the wake region of the cylinder, which are called vortices. At low values of Re $(\mathrm{Re} < 5)$,no separation occurs. When the Re is further increased, the separation occurs and becomes unstable initiating the phenomenon called vortex shedding, at a certain frequency. As a result, the wake has an appearance of a vortex street which can be seen in the figure 2.3.

Reynolds number regime	Flow regime	Flow form	Flow characteristic
$\mathrm{Re} \to 0$	Creeping flow	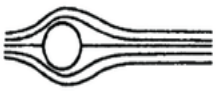	Steady, no wake
$3-4 < \mathrm{Re} < 30-40$	Vortex pairs in wake	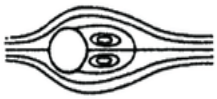	Steady, symmetric separation
$\begin{matrix}30\\40\end{matrix} < \mathrm{Re} < \begin{matrix}80\\90\end{matrix}$	Onset of Karman vortex street		Laminar, unstable wake
$\begin{matrix}80\\90\end{matrix} < \mathrm{Re} < \begin{matrix}150\\300\end{matrix}$	Pure Karman vortex street		Karman vortex street
$\begin{matrix}150\\300\end{matrix} < \mathrm{Re} < \begin{matrix}10^5\\1.3\cdot10^5\end{matrix}$	Subcritical regime		Laminar, with vortex street instabilities
$\begin{matrix}10^5\\1.3\cdot10^5\end{matrix} < \mathrm{Re} < 3.5\cdot10^6$	Critical regime		Laminar separation Turbulent reattachment Turbulent separation Turbulent wake
$3.5\cdot10^6 < \mathrm{Re}$	Supercritical regime (transcritical)		Turbulent separation

Figure 2.3: Flow regime around smooth, circular cylinder [15]

2.4.2. Vortex Shedding and Strouhal Number

The Vortex shedding phenomenon appears when pairs of stable vortices are exposed to small disturbances and become unstable at Re greater than 40. For these values of Re, the boundary layer over the cylinder surface will separate due to the adverse pressure gradient imposed by the divergent geometry of the flow environment at the rear side of the cylinder. Vortex shedding occurs at a certain frequency, which is called as vortex shedding frequency. This frequency normalized with the flow velocity U and the cylinder diameter D, can basically be seen as a function of the Reynolds number. Furthermore, the normalized vortex-shedding frequency is called Strouhal number (St), and formulated as: ($St = \frac{fD}{U}$)

The relationship between Re and St can be shown in figure 2.4.

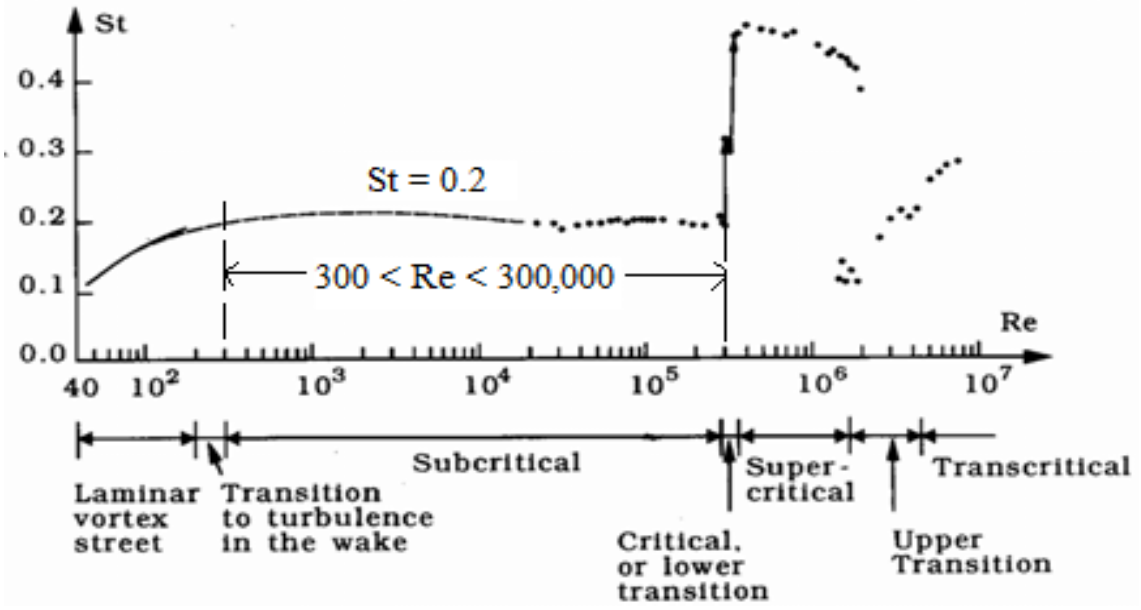

Figure 2.4: Strouhal number (St) for a smooth circular cylinder [15]

For the Reynolds number range $250 < Re_D < 2 \times 10^5$, the strohaul frequency can be estimated using the empirical formula [16] given in equation 2.6.

$$St = 0.198(1 - \frac{19.7}{Re_D}) \tag{2.8}$$

2.4.3. Blockage Ratio

Blockage ratio is the ratio of projected area of the object to the wetted cross-sectional area of tank. Mathematically,

$$\text{Blockage Ratio} = \frac{\text{Projected Area of Object}}{\text{Wetted Cross Sectional Area of Tank}} \tag{2.9}$$

For cylinder, blockage ratio can be represented as the ratio of cylinder diameter to the channel width (given in equation 2.8).

$$\text{Blockage Ratio} = \frac{\text{Cylinder Diameter}}{\text{Channel Width}} \tag{2.10}$$

For blockage ratios less than 6%, it is shown that the effects of blockage on pressure distribution and the drag coefficient are small [17] and that the Strouhal number is unaffected by blockage. For blockage ratios in the range 6-l6%, there is considerable distortion of the flow due to blockage and the effects are complex. The pressure distribution is of a different form and the Strouhal number changes. However, conflicting influences result in a blocked drag coefficient which is not very different from that at no blockage. Reduction in aspect ratio has effects on drag coefficient and on base pressure coefficient which are similar to those associated with increase in blockage ratio.

2.5. Computational Fluid Dynamics

Computational fluid dynamics, often abbreviated as CFD, involves using computer-based simulations or numerical models to analyze fluid mechanics, addressing issues related to fluid flows, heat transfer, and other phenomena like chemical reactions. CFD finds applications in various industrial and non-industrial sectors and is particularly effective in simulating fluid flows. It employs numerical methods to solve fluid flow problems since the Navier-Stokes equations, which describe fluid flow physics, cannot be analytically solved for the specific cases studied. Therefore, an approximate solution is required and the most relevant equations are

Conservation of mass:

$$\frac{\partial \rho}{\partial t} + \frac{\partial (\rho u)}{\partial x} + \frac{\partial (\rho v)}{\partial y} + \frac{\partial (\rho w)}{\partial z} = 0 \tag{2.11}$$

Conservation of momentum:

$$\frac{\partial Du}{\partial t} = \frac{\partial}{\partial x}(-p+\tau_{xx}) + \frac{\partial \tau_{yx}}{\partial y} + \frac{\partial \tau_{zx}}{\partial z} + S_{mx} \tag{2.12}$$

$$\frac{\partial Dv}{\partial t} = \frac{\partial \tau_{xy}}{\partial x} + \frac{\partial}{\partial y}(-p+\tau_{yy}) + \frac{\partial \tau_{zy}}{\partial z} + S_{my} \tag{2.13}$$

$$\frac{\partial Dw}{\partial t} = \frac{\partial \tau_{xz}}{\partial x} + \frac{\partial \tau_{yz}}{\partial y} + \frac{\partial}{\partial z}(-p+\tau_{zz}) + S_{mz} \tag{2.14}$$

General transport equation:

$$\frac{\partial \phi}{\partial t} + \frac{\partial}{\partial x}(\phi u) + \frac{\partial}{\partial y}(\phi v) + \frac{\partial}{\partial z}(\phi w) = \frac{\partial}{\partial x}\left(D\frac{\partial \phi}{\partial x}\right) + \frac{\partial}{\partial y}\left(D\frac{\partial \phi}{\partial y}\right) + \frac{\partial}{\partial z}\left(D\frac{\partial \phi}{\partial z}\right) + S \tag{2.15}$$

These equations are both interlinked and not linear. To solve such complex flows, the equations are broken down into discrete parts, which are then solved through an iterative process. In order for a computer to handle these equations, the entire domain, including its geometry, must be discretized. This discrete representation of the computational domain is known as a grid or mesh.

Solving a computational fluid dynamics (CFD) problem involves three main steps:

1. Creating a grid that represents the geometry.

2. Solving the relevant equations using a solver and a model.

3. Post-processing the results.

Additionally, the code is verified and validated by comparing its results to experimental data.

Various models are provided in simulation software to address specific problems and capture the relevant physical effects.[18]

2.5.1. Turbulence modeling

Turbulence models vary widely in complexity based on specific observation goals. Turbulence arises at high Reynolds numbers from interplay between nonlinear inertial and viscous terms in Navier-Stokes equations, involving rotating, time-dependent, 3D interactions. Vortex stretching connects rotational and 3D interactions, absent in 2D spaces. Turbulence is inherently random in time, with long-lived vortex structures traveling with flow. Turbulent quantities require consideration of upstream flow history. Ideal turbulence models balance

accuracy with minimal complexity. No universal model exists; suitability depends on the case. Variability in turbulence modeling enhances CFD modeling's intrigue and economic attractiveness, driving ongoing refinement to simulate real-world flow phenomena.

1. **Shear-stress Transport (SST) k-ω Model**
   The SST k-omega model was developed to combine the robust and accurate formulation of the k-omega model in the near-wall region with the free-stream independence of the k-epsilon model in the far field. This blending allows the SST k-omega model to be accurate and reliable for a wider range of flows, including those with adverse pressure gradients and airfoils.

   The SST k-omega model offers similar benefits as the standard k-omega model but with additional features that enhance its accuracy and reliability. It effectively accounts for the transport of turbulent shear stress and provides highly accurate predictions of flow separation onset and magnitude under adverse pressure gradients.

   While the SST k-omega model is suggested for high-accuracy boundary layer simulations, its reliance on wall distance makes it less appropriate for free shear flows than the regular k-omega model. Mesh resolution near the wall is required to accurately capture flow mechanics. [19]

2.6. Particle Image Velocimetry(PIV)

Particle image velocimetry (PIV) is an experimental technique employed to determine the velocity distribution within a fluid flow [20]. This technique involves capturing images of tracer particles in the fluid using a high-speed camera and subsequently cross-correlating these images to extract the velocity field information. In recent years, particle image velocimetry has gained widespread acceptance as a valuable tool for investigating various fluid dynamics problems [21].

Turbulent flow is characterized by highly chaotic motion occurring at high Reynolds numbers, with the flow exhibiting random movement in multiple directions. The unpredictable and distinctive nature of turbulence has driven efforts to enhance PIV techniques. These enhancements include the use of small particles, a high-intensity pulsed laser, and a short-exposure camera. Presently, the standard components utilized in a PIV system typically consist of a pulsed laser with high beam intensity, particles on the order of a few microns in size, and a high-speed camera.[20]

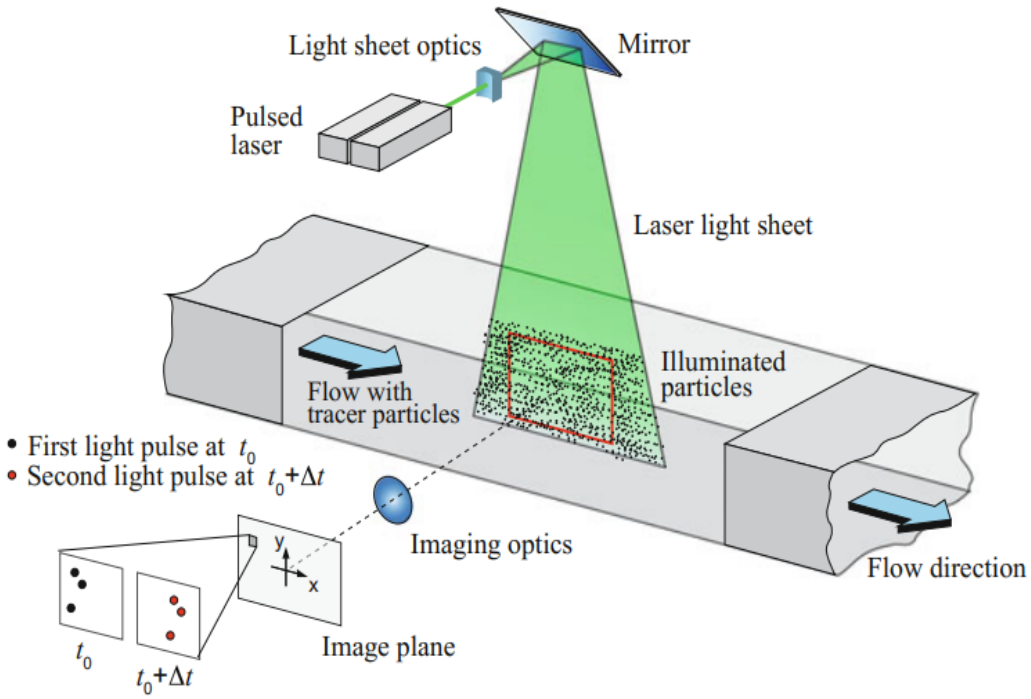

Figure 2.5: Particle Image Velocimetry Setup [20].

Figure 2.5 illustrates the fundamental experimental setup for conducting Particle Image Velocimetry (PIV). This setup comprises key components including a laser, which may operate in a continuous or pulsed manner, and light sheet optics consisting of a combination of cylindrical and spherical lenses. The laser emits a focused beam directed towards the light sheet optics, where it is transformed into a planar light sheet. A fluid containing tracer particles is then propelled at the desired velocity, and the light scattered by these tracer particles is captured by a high-speed camera. This process rapidly generates a large number of images within a fraction of second. Subsequent cross-correlation analysis of these images enables the determination of the velocity field of the flow.[20].

2.6.1. Seeding particles

Seeding particles are used to track the fluid motion in a flow. These are small micron particles made from materials with the same density as that of the fluid. While carrying out PIV measurements, the distance covered by the seeding particles in a small time interval t is measured by the cross-correlation between different images. Therefore, the measurement accuracy is greatly affected by the shape of seeding particles, their size, density ratio of the particle and the liquid, and fluid viscosity[20].

(a) Stokes number

The Stokes number (Stk) is a dimensionless parameter that characterizes the behavior of particles in a fluid flow. It is the ratio of the particle response time to the characteristic flow time.

$$Stk = \frac{\rho_p d_p^2}{18\mu_f} \frac{u_f}{D} \tag{2.16}$$

(b) Relaxation time

The relaxation time (τ_s) is a characteristic time that represents the time it takes for the particle's velocity to adjust in response to changes in the fluid flow.

$$\tau_s = \frac{d_p \times \rho_p}{18\mu} \tag{2.17}$$

(c) Settling time

The settling time (V_T) refers to the time it takes for particles to settle in a fluid under the influence of gravity.

$$V_T = \frac{g \cdot d_p^2 \cdot (\rho_p - \rho_f)}{18\mu} \tag{2.18}$$

The particles generally used in the case of liquid flows are listed, with their mean diameter, in the table below:-

Table 2.1: Seeding Particles in Liquid [20]

Type	**Material**	**Mean diameter in μm**
Solid	Polystyrene	10-100
	Aluminum flakes	2-7
	Hollow glass spheres	10-100
	Granules for synthetic coatings	10-500
Liquid	Different Oils	50-500
Gaseous	Oxygen bubbles	50-1000

2.6.2. Laser illumination

PIV can be accomplished using continuous wave (CW) lasers or, more optimally, pulsed lasers. The power of the Laser depends upon the light-scattering properties. Light scattering capability is quantified by the scattering cross section (Cs), defined as the ratio of total

scattered power (P_s) to incident laser intensity (I_0):

$$C_s = \frac{P_s}{I_0} \tag{2.19}$$

The light scattering by a 10 μm glass particle in water can be obtained from the figure 2.6.

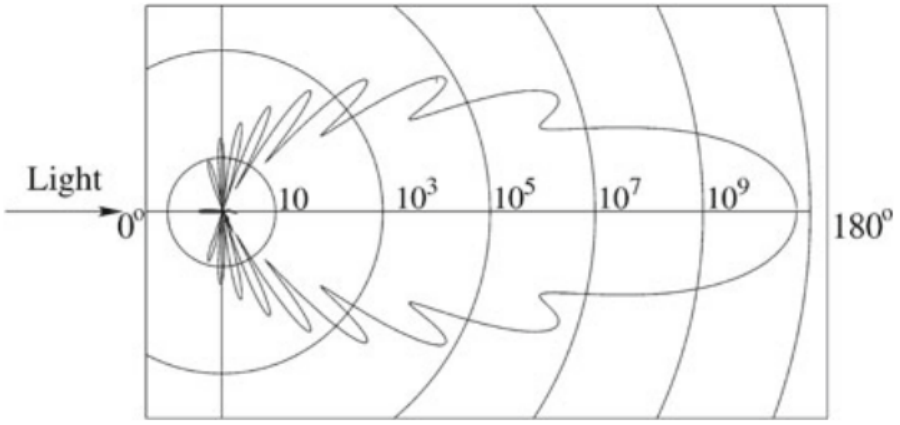

Figure 2.6: Scattering of light by a 10 μm glass particle in water [20]

For spherical particles with a refractive index of 1.5, the following figure illustrates Cs variations concerning the particle diameter (d_p) to laser wavelength (λ) ratio.

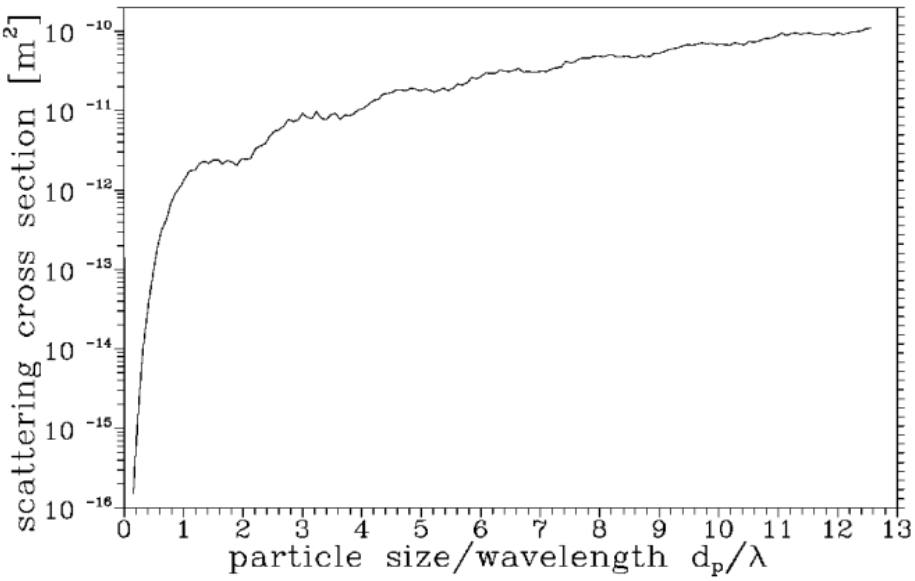

Figure 2.7: The scattering cross section as function of particle size [20]

Comparison between diatomic molecules (e.g., nitrogen or oxygen) and larger particles (1–10 μm diameter) in Table 2.2 reveals substantial differences in scattering cross-sections.

Table 2.2: Scattering Cross-section Variation with Particle Size [22]

Particle Size	**Scattering Cross-section (Cs)**
Molecule	$10^{-33}\,m^2$
1 μm particle	$10^{-12}\,m^2$
10 μm particle	$10^{-9}\,m^2$

2.7. PIV Image Processing

PIV demands a substantial effort in processing particle images to obtain an accurate velocity field. Numerous algorithms have been devised for this purpose, with software solutions available in both proprietary and open-source domains. The processing of PIV images involves three sequential steps:

1. Image Pre-processing (Preliminary image pre-processing)
2. Image Evalaution (Identification of particles and reconstruction of vectors)
3. Post-processing of random data and representation of the resulting field.

2.7.1. Image Pre-processing

In Particle Image Velocimetry (PIV), minimizing erroneous velocity estimates to ensure high measurement quality is crucial. One common approach, supported by Raffel et al. (2007) and Shavit et al. (2007), involves pre-processing images before correlation. This includes adjusting for background illumination, correcting uneven particle illumination, and addressing out-of-plane particle illumination using image segmentation and morphological algorithms. Several tools for image segmentation serve these purposes, briefly described below:

1. **Histogram Equalization:** CLAHE (Contrast Limited Adaptive Histogram Equalization) was developed to improve the interpretability of medical imaging data. It operates on small image regions or tiles, distributing the most frequent intensities of the image histogram across the entire data range (from 0 to 255 in 8-bit images). This enhances regions with low and high exposure independently, significantly increasing the likelihood of detecting valid vectors in experimental images by 4.7$\pm$3.2% [23].

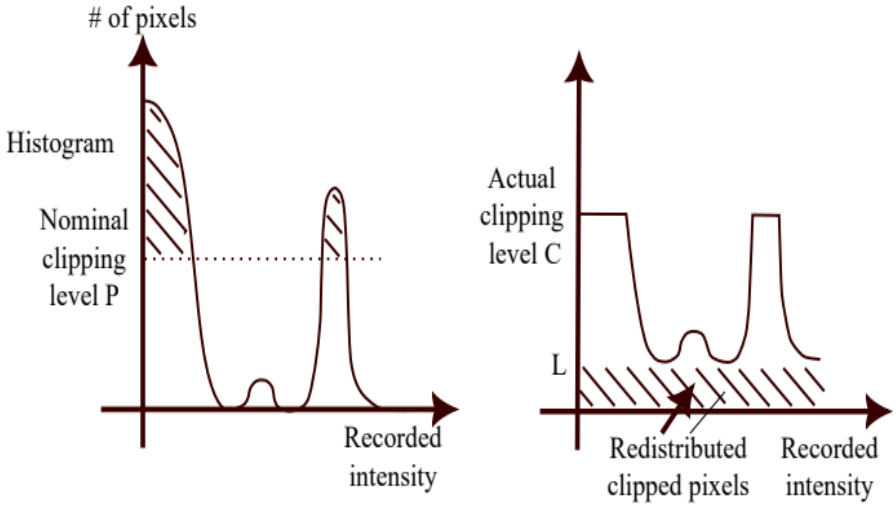

Figure 2.8: Image Histogram before (left) and after (right) CLAHE [23]

2. **High-pass Intensity:** Uneven lighting can introduce low-frequency background information, which can be addressed with a high-pass filter. This filter emphasizes particle details while suppressing low-frequency information, including displacement data [24].

3. **Intensity Capping:** In DPIV, non-uniform flows can lead to biased results due to uneven particle motion within interrogation windows. Bright particles may disproportionately affect the correlation signal [25]. The intensity capping filter sets an upper limit for grayscale intensity, minimizing potential negative impacts and improving the likelihood of detecting valid vectors in experimental images by $5.2 \pm 2.5\%$. [24]

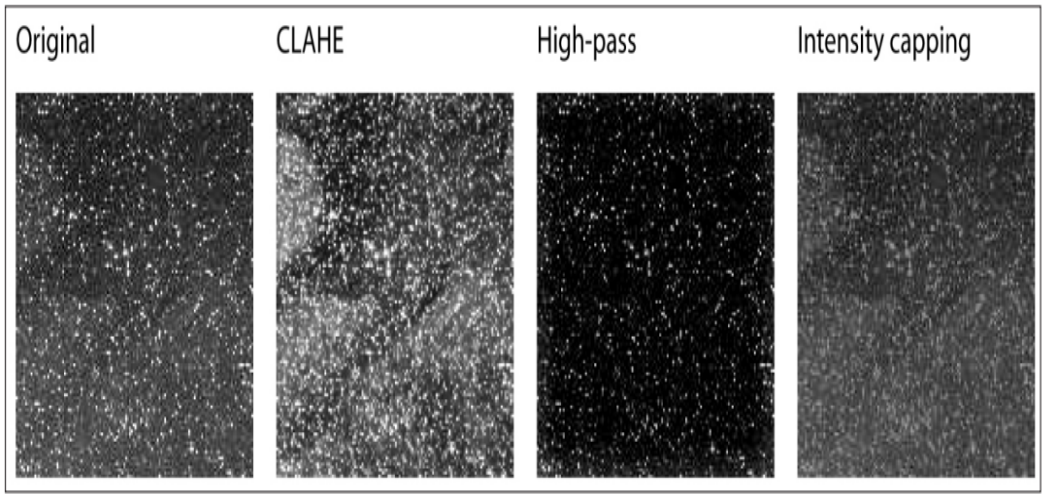

Figure 2.9: The effect of several pre-processing techniques [25]

4. **Wiener2 Denoise:** The Wiener2 algorithm removes noise from digital photographs using local filtering. It calculates local noise power and signal-to-noise ratio for each pixel within a window, then applies a filter to minimize mean squared error, effectively denoising the image.

5. **Contrast Stretching:** Contrast stretching enhances image contrast by expanding the dynamic range of intensity values, mapping original levels to a new range. Linear scaling normalizes intensities to 0 and 255 for an 8-bit image, while non-linear functions like logarithmic or power-law functions offer better control.

Additionally, the ability to subtract the background image by calculating the mean intensity of image frames is present. In cases where the mentioned algorithms prove insufficient for generating a noise-free particle image, pre-processing becomes essential before inputting data into the desired processing software.

2.7.2. Image Evaluation

The critical aspect of PIV analysis is the cross-correlation algorithm, where small sub-images within an image pair undergo cross-correlation to deduce likely particle displacements. This statistical pattern-matching technique aims to identify particle patterns between interrogation areas A and B. The discrete cross-correlation function is used:

$$C(m,n) = \sum_{i}\sum_{j} A(i,j)B(i-m, j-n) \tag{2.20}$$

where A and B represent corresponding interrogation areas from image A and image B. The location of the intensity peak in the resulting correlation matrix C provides the most probable particle displacement from A to B.[12].

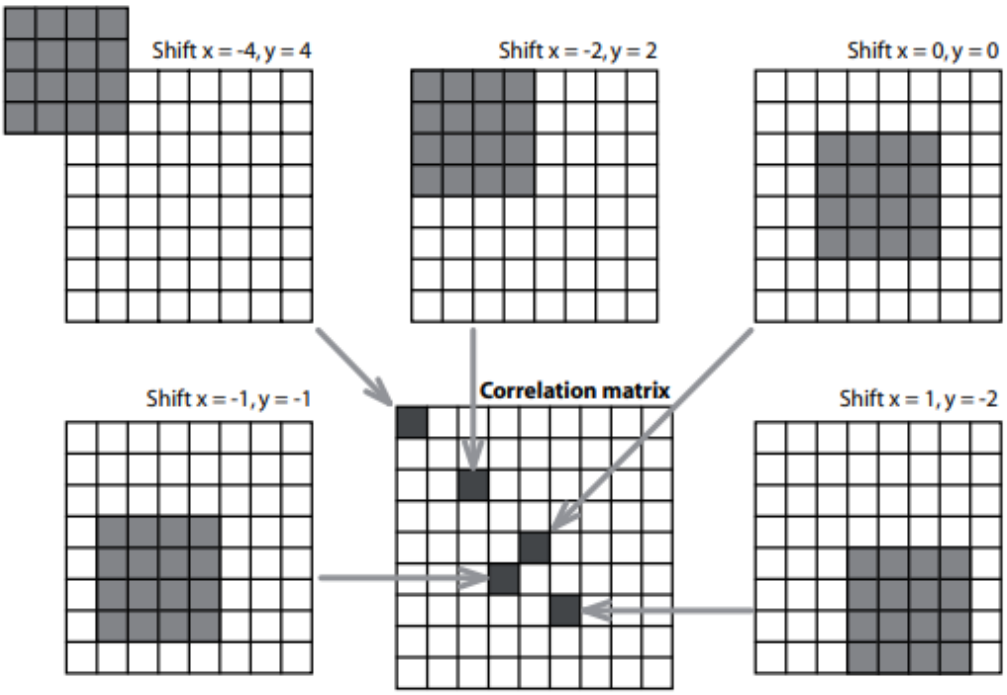

Figure 2.10: Calculation of the correlation matrix using DCC [25]

Two main approaches to solving equation 2.20 exist: direct computation in the spatial domain and using Discrete Fourier transform (DFT) in the frequency domain. The spatial domain method is known as direct cross-correlation or convolution filtering, while the frequency domain method involves DFT through fast Fourier transform, each with its own advantages and drawbacks.[25]

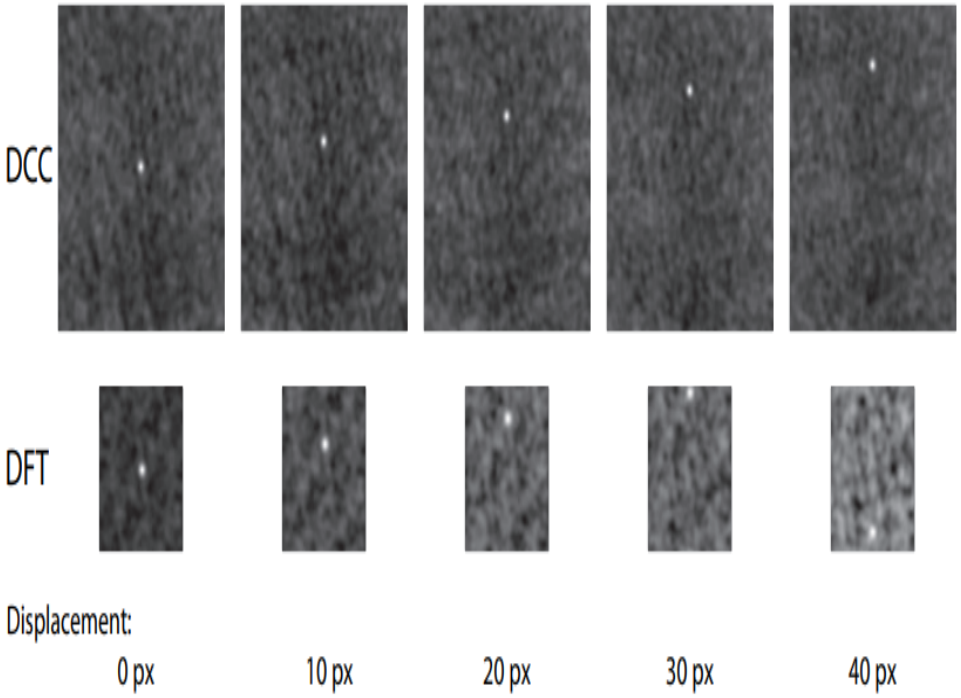

Figure 2.11: Correlation matrices of the DCC (top) and the DFT approach (bottom) [25]

1. **Direct cross-correlation (DCC)**

   Direct cross-correlation (DCC) calculates correlation in the spatial domain, accommodating different sizes for regions A and B [26]. Opting for B twice the size of A prevents information loss for particle displacements up to half the size of A, ensuring a reliable correlation matrix with minimal noise. [25].

2. **Discrete Fourier Transform (DFT) and advanced DFT techniques**

   To address DCC's computational cost, frequency domain correlation using FFT can be employed, though this introduces increased background noise due to identical-sized interrogation areas. Mitigating this, multiple passes of DFT on the same dataset refine the interrogation grid, achieving a high spatial resolution in the final vector map with optimal signal-to-noise ratio.[25].

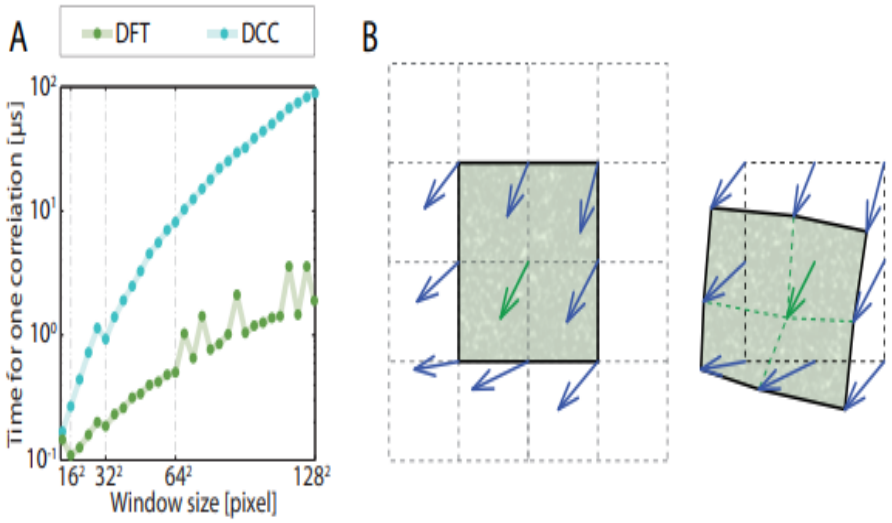

Figure 2.12: Calculation speed of DCC compared to DFT [25]

In real flows, particle patterns undergo shearing and rotation, leading to non-uniform motion that broadens correlation matrix peaks, potentially degrading results. PIVlab iteratively deforms interrogation areas based on displacement information from overlapping regions, enabling high-precision displacement determination. Velocity information is smoothed and validated between passes, with stringent data validation ensuring accuracy.[25]

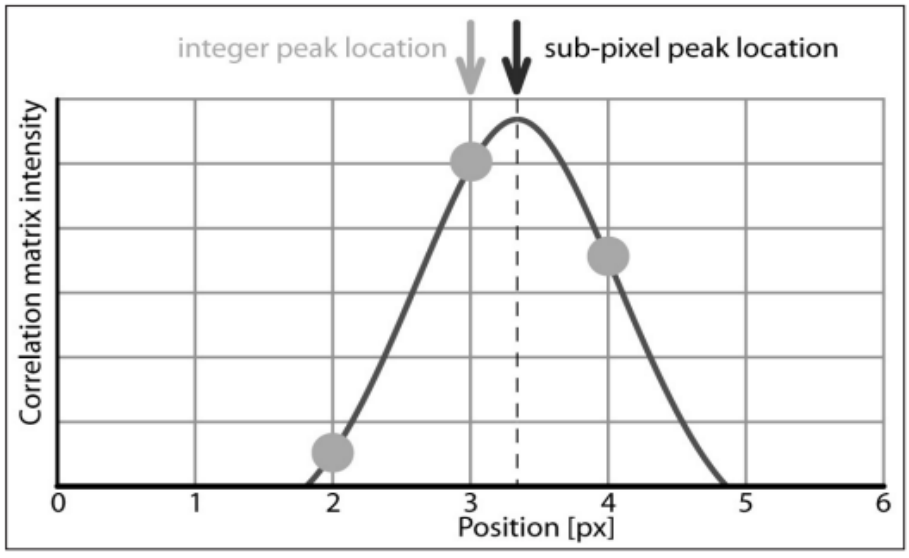

Figure 2.13: Principle of the Gaussian 2×3-point fit: Subpixel precision is attained by fitting a one-dimensional Gaussian function (solid line) to the integer intensity distribution of the correlation matrix (dots) for both axes independently (only one axis is displayed here) [25].

3. **Peak Identification** Peak identification method choice significantly influences PIV accuracy. Integer displacement is determined by locating the intensity peak in the correlation matrix, refined with sub-pixel precision using a Gaussian function fitting.This process considers neighboring pixels separately for x and y axes to achieve sub-pixel precision [25].

   When particles undergo shear, rotation, or if there's excessive motion blur, their displacement peaks may appear elliptical. In such cases, a two-dimensional Gaussian function (9-point fit) works better, especially in methods like DCC and single-pass DFT, both used in PIVlab.

2.7.3. Post Processing

1. **Data Validation**

   Post-processing of PIV data is generally required to obtain reliable results [25]. A basic method to filter outliers in PIVlab is to choose limits for acceptable velocities manually. Velocity thresholds can also be determined semi-automatically by comparing each velocity component with a lower threshold and an upper threshold ($t_{\text{lower}}, t_{\text{upper}}$):

   $$t_{\text{lower}} = \bar{u} - \eta\,\sigma_u \tag{2.21}$$

   $$t_{\text{upper}} = \bar{u} + \eta\,\sigma_u \tag{2.22}$$

   where u = mean velocity; σ_u = standard deviation of u. The user-defined value of η determines the strictness of this filter.

2. **Data Interpolation**

   After the removal of outliers, missing vectors should be replaced by interpolated data . One common technique is the 3×3 neighborhood (3×3 mean) interpolation. PIVlab uses a boundary value solver for interpolation .

3. **Data Smoothing**

   A certain amount of measurement noise will be inevitable in PIV analyses . Noise can be effectively reduced by applying data smoothing. [20] propose to perform a convolution of the data with a 2×2 or 3×3 kernel with equal weights. Another common and effective method to smooth PIV data is median filtering. [25]

4. **Data Exploration**

In DPIV studies, complex flow patterns are often challenging to describe using vector maps alone. PIVlab stands out by providing numerous options to further process and distill results. It allows calculation of derivatives like vorticity and divergence, extraction of data from paths or areas, and comfortable calculation of integral quantities, offering extensive analysis possibilities.[25]

CHAPTER THREE: METHODOLOGY

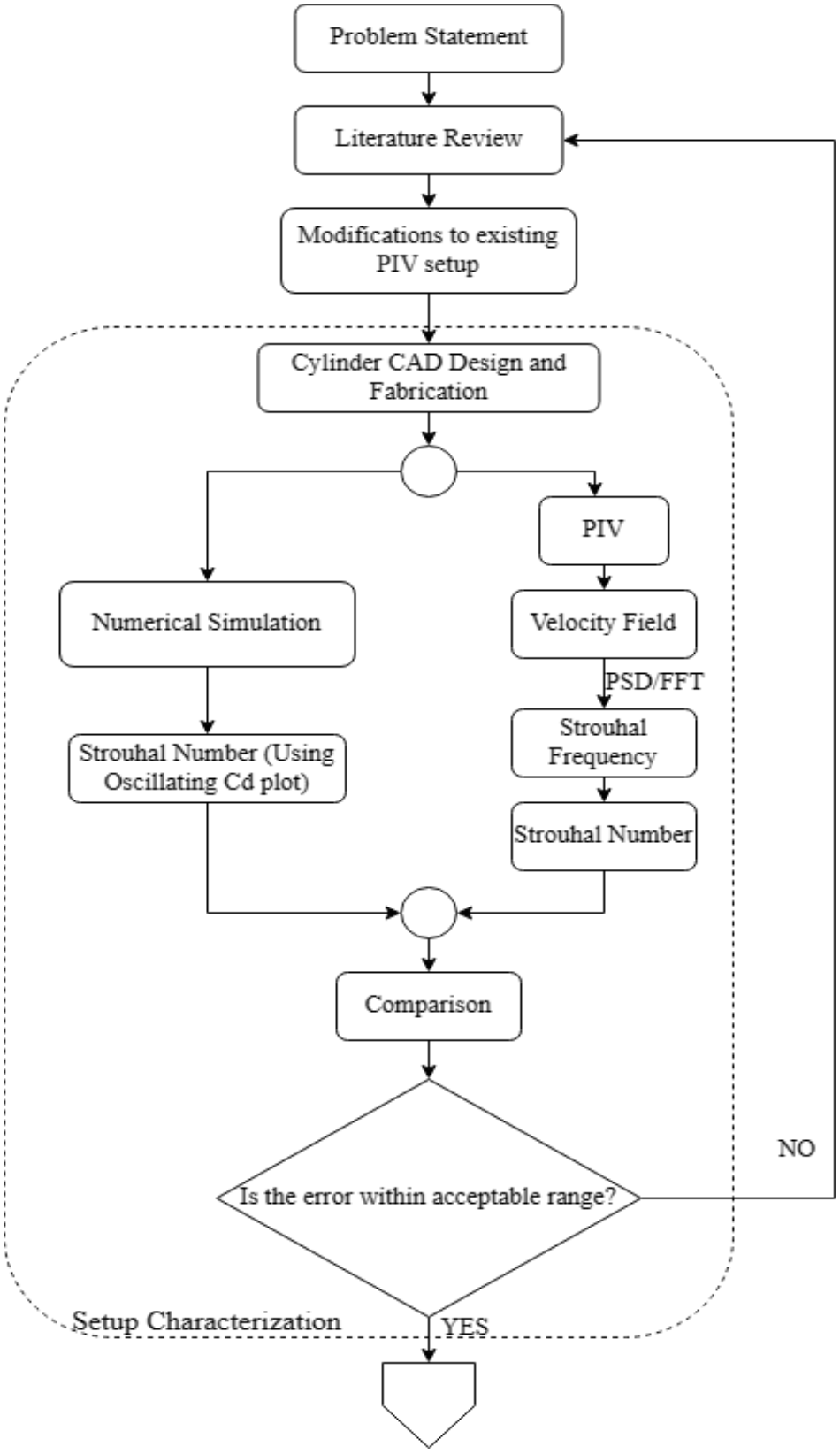

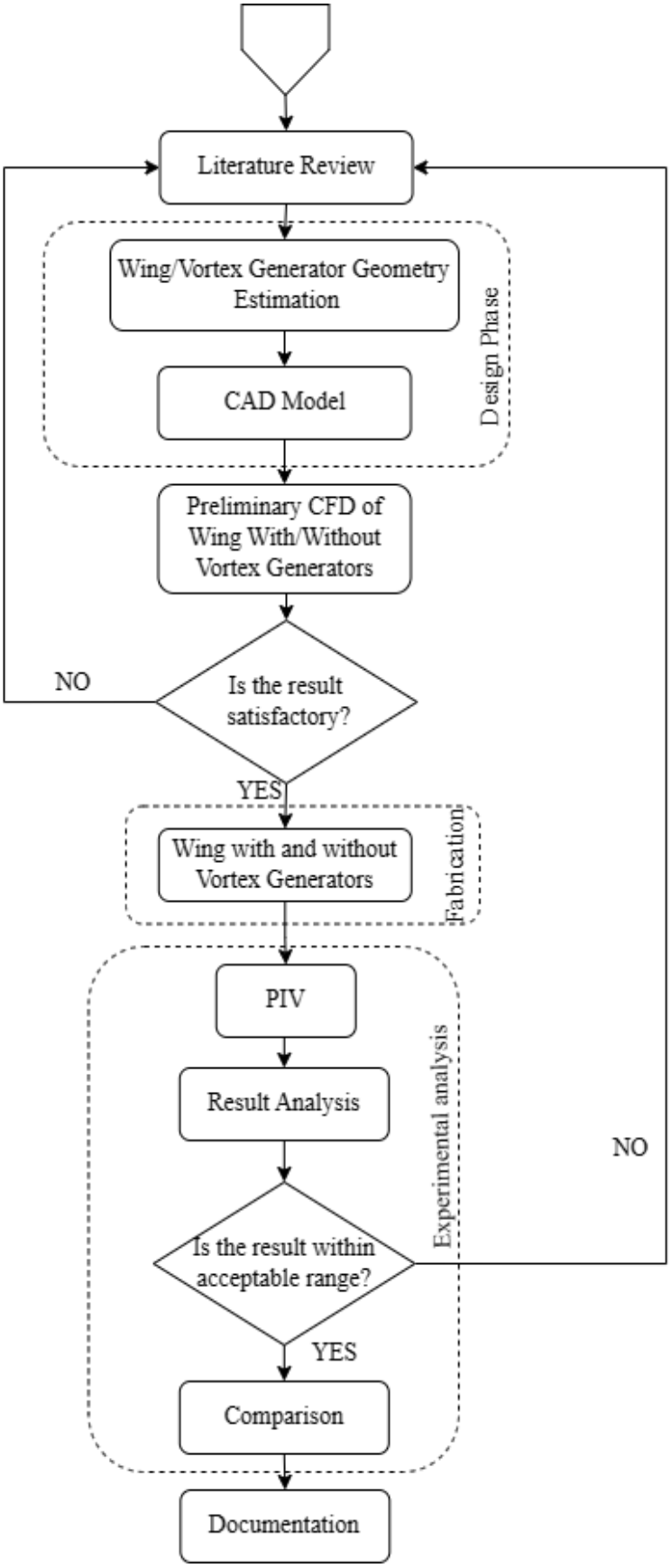

Figure 3.1: Process Flowchart

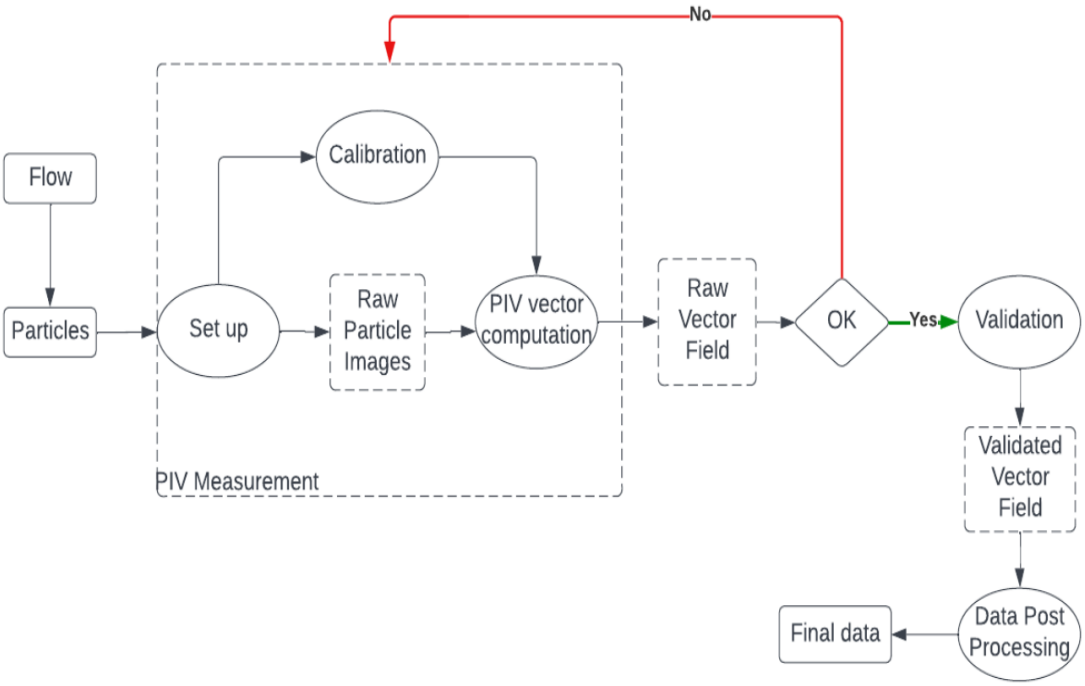

Figure 3.2: PIV Process Flowchart (Source: ITTC Quality System Manual)

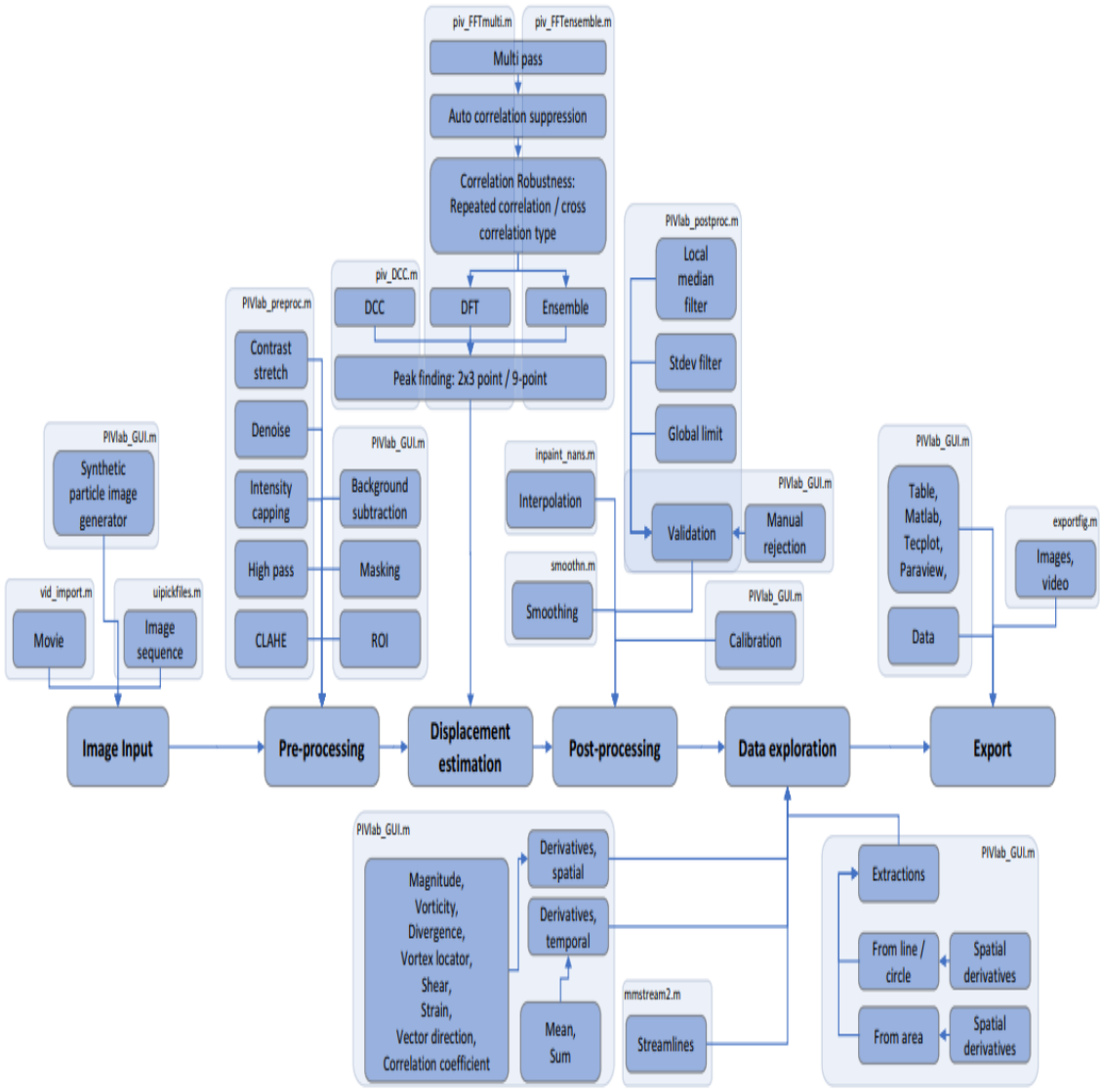

Figure 3.3: Image Processing Flowchart [27]

3.1. Modifications to existing PIV setup

3.1.1. Gantry System

The gantry system was modified to improve the accuracy of PIV measurements by limiting the motion to one degree of freedom and reducing discontinuous (characterized by vibration and occasional breaks) motion.

(a) CAD Model

A linear traveling mechanism comprised of bearings, threaded rods, nuts, and a hollow rectangular metal workpiece was designed to achieve the aforementioned goals.

The corresponding CAD model is shown in Figure 3.4. The linear gantry model is adjustable i.e., can be fitted to travel on rod of different cross sections.

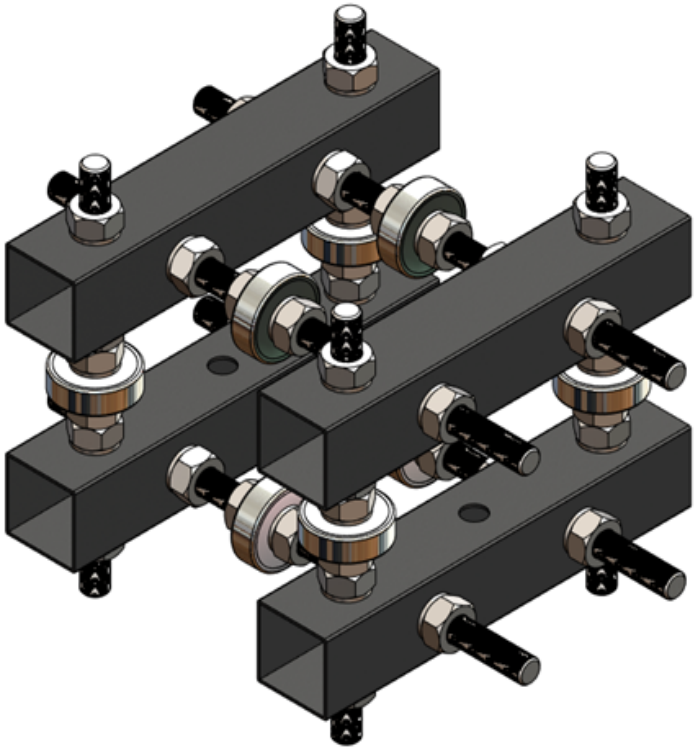

Figure 3.4: CAD Model of Gantry roller

The assembly of the gantry system (excluding motor mount and driven part) is shown in Figure 3.5.

Figure 3.5: CAD Model of Gantry Assembly

Other parts and views are shown in the appendix.

(b) Fabrication

The gantry roller, shown in figure 3.6, was fabricated using light weight materials.

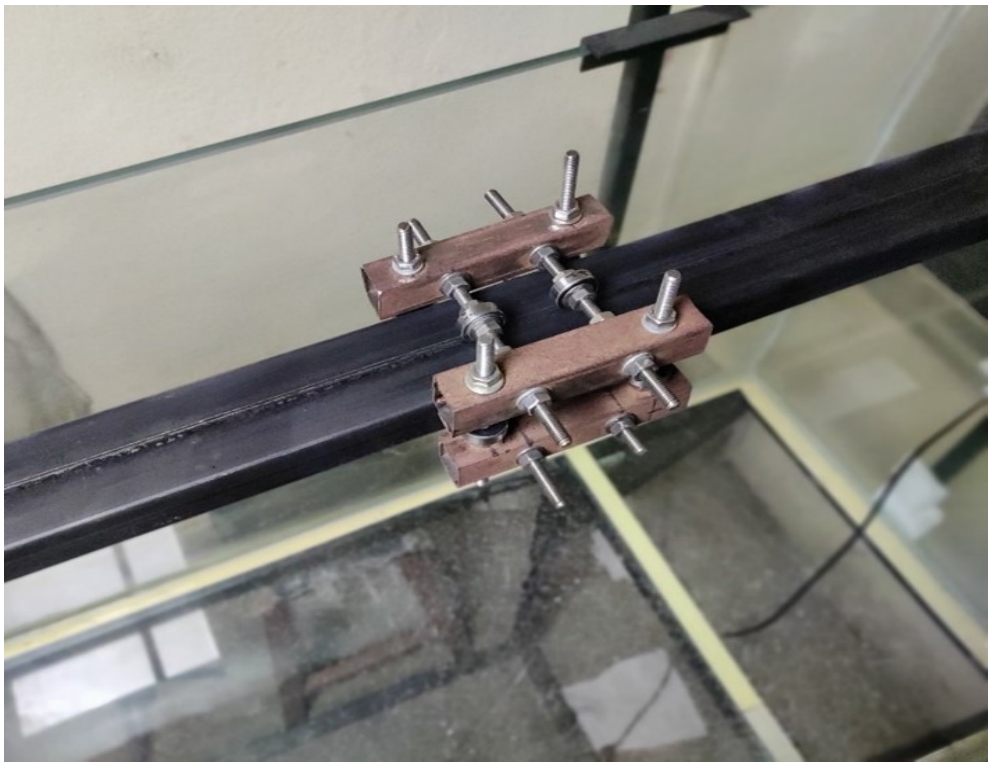

Figure 3.6: Fabricated Gantry Roller

Figure 3.7: Gantry system attached to the tank setup

Figure 3.8 shows the Gantry Assembly under which the cylindrical test specimen is attached.

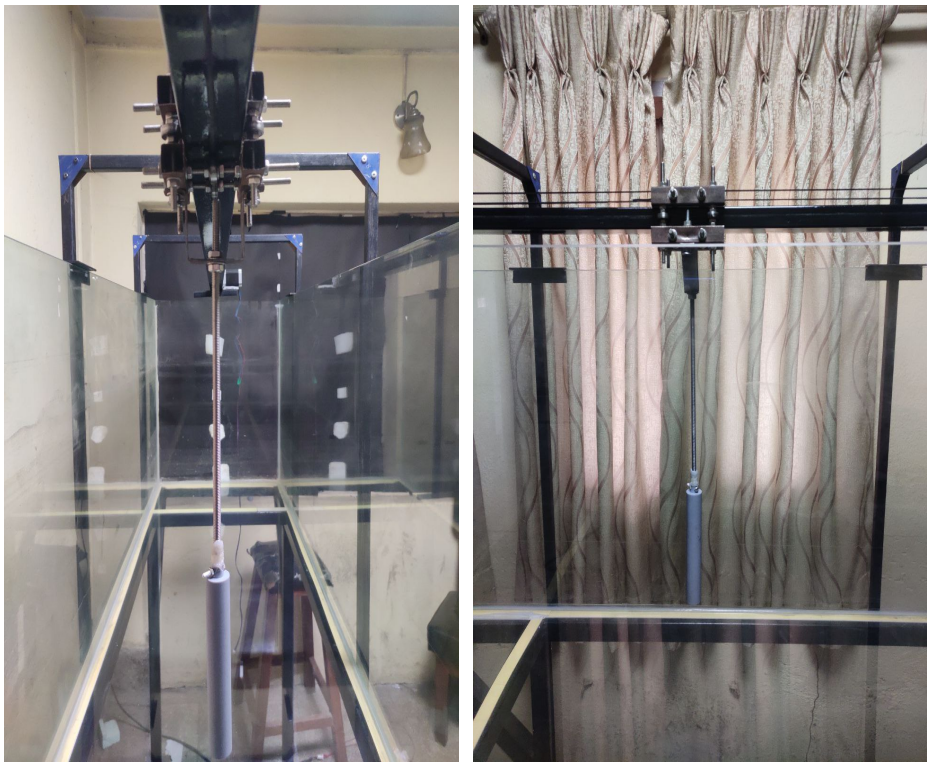

(a) Front View (b) Side View

Figure 3.8: Cylinder Model attached to the Gantry Assembly

3.1.2. Electronics

The need for high power, smooth motor motion, and comparatively more speed options (than the old setup) within the applicable torque range, resulted in the selection of the specific electronics components. They are listed in the table 3.1.

Table 3.1: Electronics Components

S.N	Particulars	Quantity	Features
1	Nema 23 Stepper Motor	1	1.89 Nm holding Torque
2	TB6600 Stepper Motor Driver	1	Microstep up to 6400 steps/rev
3	Arduino Uno (microcontroller)	1	-
4	Mini Breadboard	1	-
5	Self locking push button	3	-
6	24 V DC power supply	1	-

The TB6600 motor driver's micro stepping settings result in a smooth rotation of the motor, whereas the Nema 23 Stepper Motor's high holding torque provides more speed options within the applicable torque range.

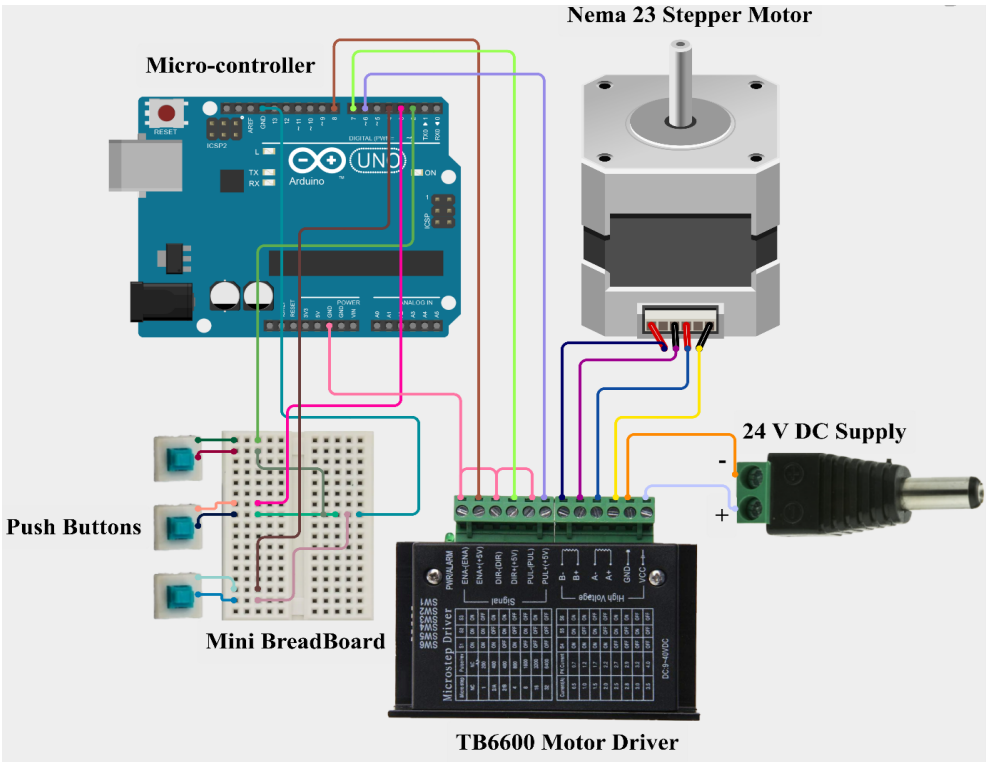

Figure 3.9: Electronic Circuit

The electronic circuit shown in Figure 3.9 was used to drive the stepper motor. And the Arduino code used to run the motor is mentioned in the appendix.

3.2. PIV Components

3.2.1. Laser

From Table 2.2,
$C_s = 1 \times 10^{-9}$
Intensity (I) = 15×10^6
The minimum scattering power required for the experiment must be 15mw.

Due to local unavailability of the planar laser having at least 15 mW power, a 100mW pointer laser was converted into planar using hollow glass tube. And the available 5mW planar laser was used from other side of the tank (such that the plane of two lasers nearly mesh into one another) to prevent the generation of shadow region.

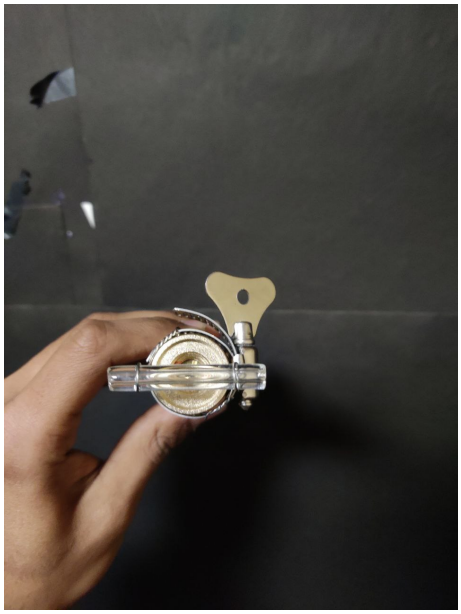

(a) Front View

(b) Side View

Figure 3.10: 100mW Laser With Glass Tube

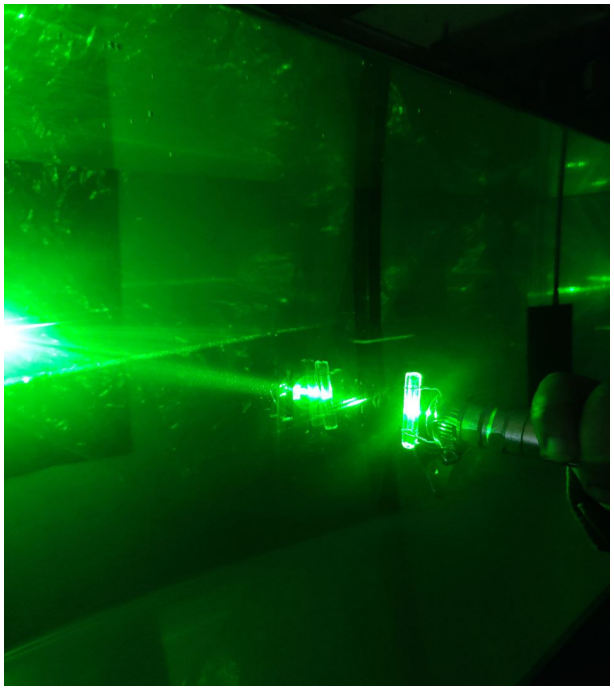

Figure 3.11: Illuminating Laser (100 mW)

Figure 3.12: 5mW Laser

3.2.2. Seeding particle

Hollow glass spheres having diameter within 10 - 20μm, were used for the seeding purposes. The parameters of the seeding particles are tabulated in the table 3.2.

Table 3.2: Seeding Particles Parameter

Parameters	**Value**
Density	1.05 g/cc
Refracting Index	1.5
Relaxation Time	0.583 s
Settling Velocity	$1.09 \times 10^{-5} m/s$
Stokes Number	1.56×10^{-5}

Figure 3.13: Hollow Glass Spheres

3.2.3. Camera

Two different cameras were utilized for capturing of raw videos for experimental analysis. They are:

1. iPhone 13 with 120 fps
2. Sony Alpha 6000 with 50 fps

3.3. Test Specimen

3.3.1. Design

Based on the tank dimensions (2 m x 0.5 m x 0.6 m), the dimensions of the circular cylinder and wing were calculated, considering a blockage ratio (BR) of 5%. For the VGs, the dimensions are based on the available literature. The calculations are shown under respective headings.

(a) Circular Cylinder

Here,

$$\mathrm{BR} = \frac{\mathrm{D}}{\mathrm{w}} = 0.05$$

$$\text{or, } \mathrm{D} = 0.05 \times 0.5 = 0.025 \text{ m (25 mm)}$$

So, the diameter of the cylinder, D = 25 mm. And the length was chosen to be 150 mm as per setup feasibility.

Figure 3.14: Circular Cylinder CAD Model

(b) Wing without Vortex Generator

NACA 2412 airfoil was chosen to model the wing. The calculations for the wing are given below:

Here,

$$\text{Aspect Ratio(AR)} = \frac{b^2}{S_1}$$

$$S_1 = \frac{b^2}{AR}$$

The wetted cross-section of the tank,

$$S_2 = 0.5 \times 0.5 = 0.25m^2$$

Then,

$$BR = \frac{S_1}{S_2}$$

$$\text{or, } 0.05 = \frac{\frac{b^2}{AR}}{0.25}$$

$$AR = 80b^2$$

Also,

$$AR = \frac{b}{c} \text{ where, c = chord of the wing = 0.075 m}$$

$$\text{So, } \frac{b}{0.075} = 80b^2$$

$$\text{or, } b = \frac{1}{80 \times 0.075}$$

$$b = 0.1667m(16.67cm)$$

And,

$$AR = \frac{b}{c} = 2.22$$

The dimensions obtained from the above calculations are tabulated in table 3.3.

Table 3.3: Dimensions for wing

Parameters	**Value**	**Unit**
Chord (c)	0.075	m
Aspect Ratio (AR)	2.22	
Span (b)	0.1667	m
Planform Area (S_1)	0.0125	m^2

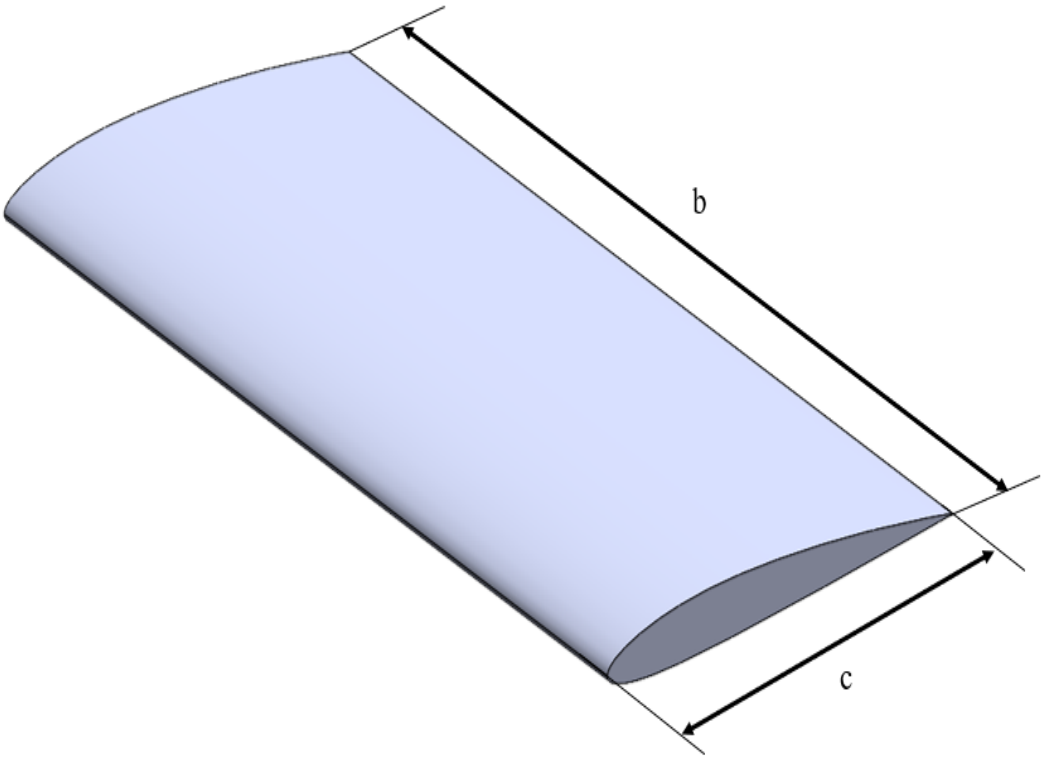

Figure 3.15: Wing without Vortex Generator

(c) Wing with vortex generator

The type of VG chosen is triangular-shaped conventional type vortex generator. The chosen wing configuration has 5 pairs of vortex generator separated by a distance(λ) of 35mm and located at the distance of 0.0085m from the leading edge. The distance between the two VG (d) is 5mm. The optimum height of the VG was selected to be 5mm (less than the laminar boundary layer thickness estimated from Xfoil for 15 deg AOA) based on the effectiveness of the VGS while performing preliminary CFD. The length of vortex generator was chosen to be l=15mm (l/h = 3). The VGs have an angle of incidence(β) of 12° . The thickness of VG was chosen to be 0.25 mm. The VG was placed at a location immediately before flow separation (at 15 deg AOA).

Table 3.4: Dimensions for VGs

Parameters	**Dimensions**	**Unit**
h/δ	1	
l/h	3	
Distance between VG (d)	5	mm
Distance between a pair of VG (λ)	35	mm
Angle of Incidence (β)	12	degrees
Thickness of VG (t)	0.25	mm

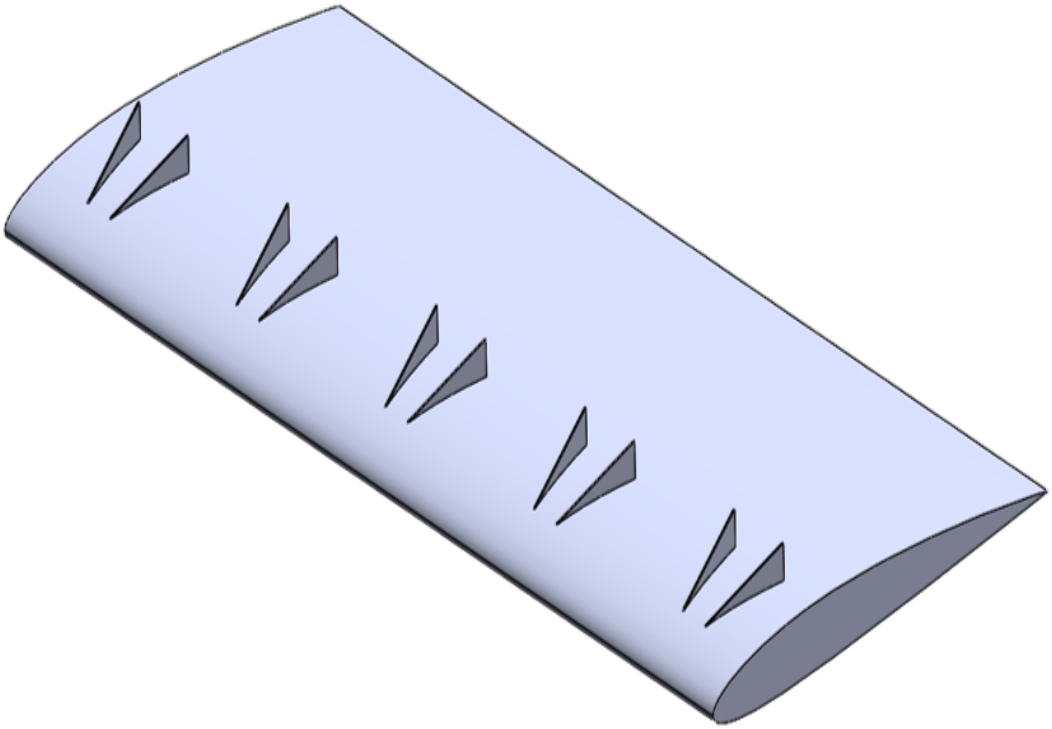

Figure 3.16: Wing with VGs

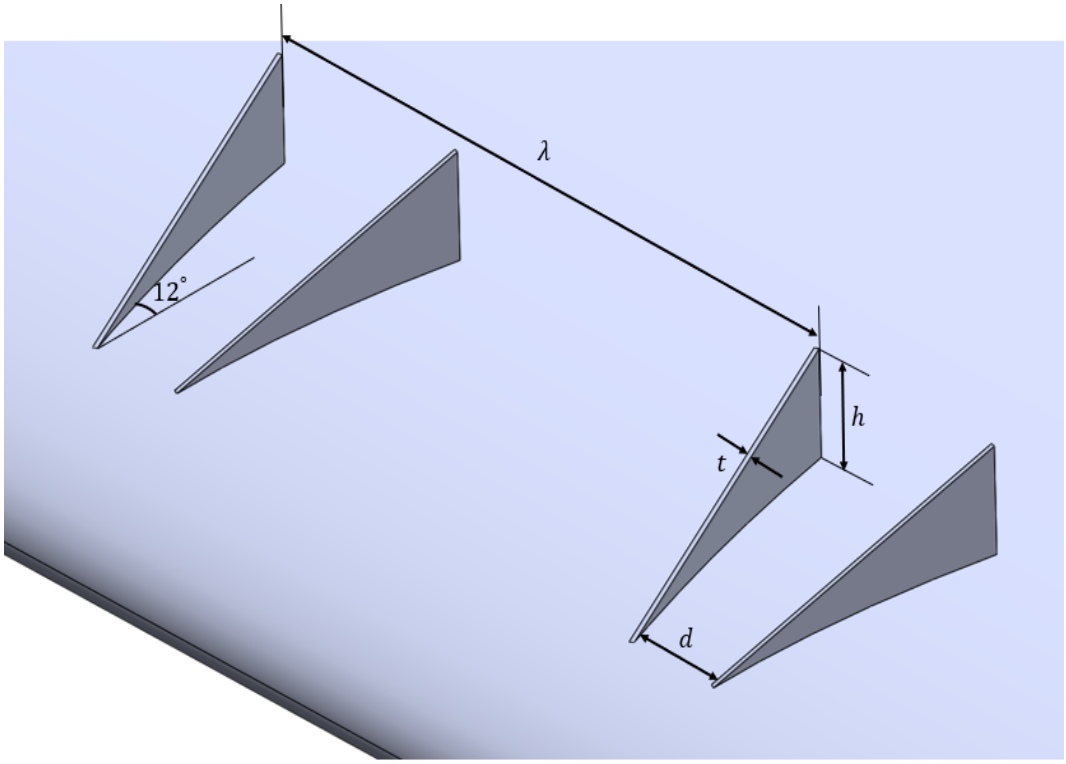

Figure 3.17: VGs

3.3.2. Fabrication

The circular cylinder, baseline wing, and wing with VG were fabricated using a Resin 3d printer. A resin 3d printer, rather than a conventional nozzle 3d printer, was used because smooth surface finishing was required and VGs having small sizes needed to be printed.

Figure 3.18: Resin Printed Circular Cylinder

After fabrication, these test models were black-painted to reduce the surface illumination due to the beam from the laser source.

(a) Wing Without VGs (b) Wing with VGs

Figure 3.19: Resin Printed Wing Models

3.4. Setup Characterisation

The strouhal number of the vortex shedding for flow over the circular cylinder is used as a comparison parameter to characterize the PIV setup. After the mesh independence study, the strouhal number obtained from the CFD analysis is compared to the experimental results from the PIV setup. The strouhal frequency is calculated from the post-processed velocity field result of the PIV experiment using power spectral density analysis and FFT.

3.5. Preliminary CFD of baseline wing and wing with VG

To determine the stall angle of attack for the wing at the corresponding Reynolds no. and obtain the optimum position of VGs (along the chord), a preliminary 3D CFD simulation was conducted.

In the 3D simulation, unsteady RANS (Reynolds Averaged Naviers Stokes) calculations was done using the Ansys Fluent package. For the Unsteady RANS fluent calculation, the two equations SST (Shear Stress Transport) k-ω turbulence model was employed. The mesh elements number was optimum considering the tradeoff between the accuracy and simulation

period.
Based on the net Coefficient of lift C_L values obtained for different angle of attack, the stall angle of attack was determined to be 15 deg. The C_L vs α plot for the baseline wing is shown in figure 3.20.

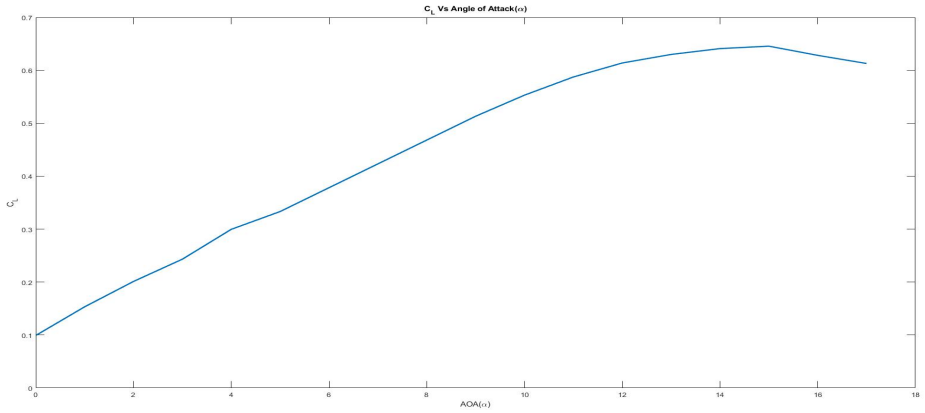

Figure 3.20: C_L vs α

Then, the unsteady RANS 3D simulation was done for wing with VG at 15 deg AOA. The location of VG was kept just before the flow separation point for baseline wing, which is 8.5mm behind the wing leading edge measured along the chord. The initial geometry of the VG was selected based on the literature and then, the optimum height of the VG was selected depending on how effectively the flow separation was delayed. The 5mm height VG was found to effectively delay the flow separation which is also less than the laminar boundary layer thickness obtained from X-foil calculations.
From the comparison of the velocity vector plots (for the plane taken at the mid-section along the span of the wing) which are shown in figures 3.21 and 3.22, it can be concluded that the VGs effectively delayed the flow separation.

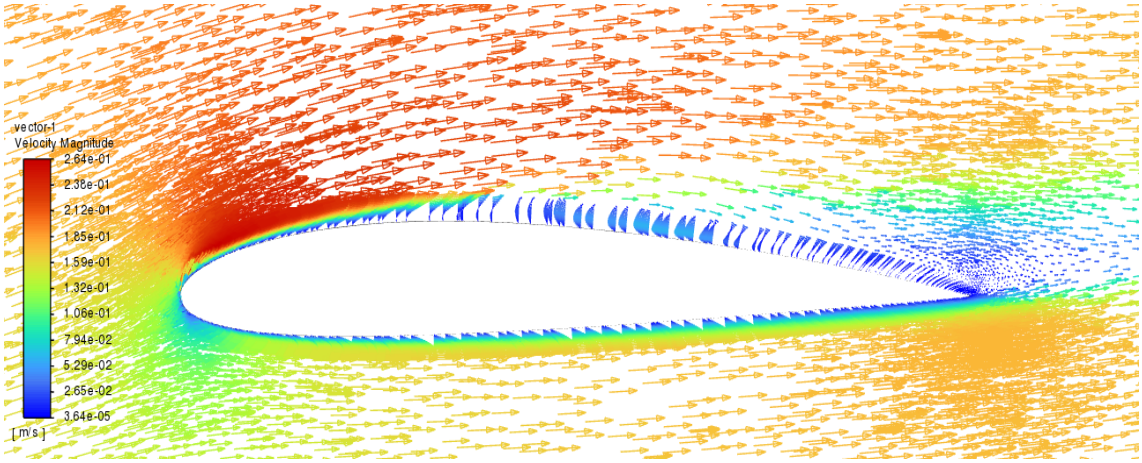

Figure 3.21: Velocity Vector Plot of flow around the baseline wing at mid-section along span for 15 deg AOA

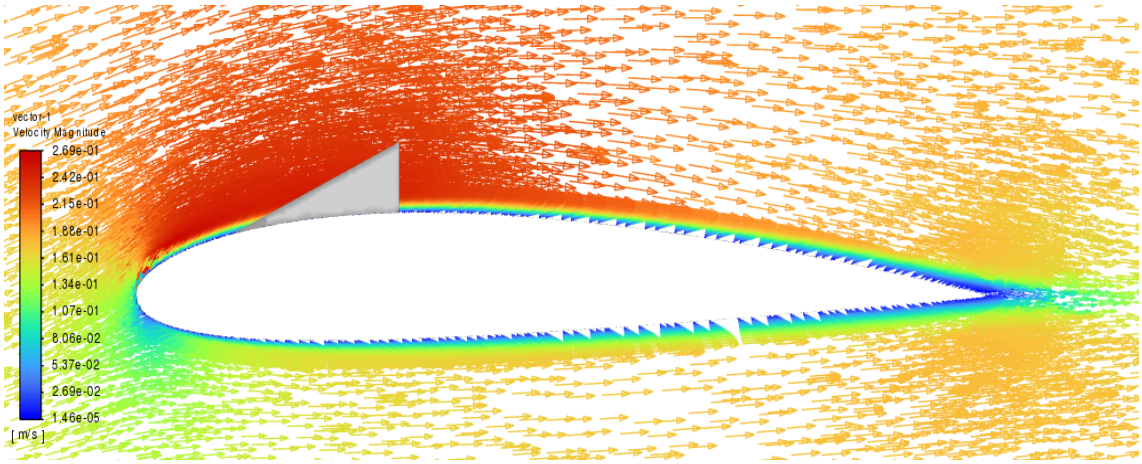

Figure 3.22: Velocity Vector Plot of flow around the wing with VGs at mid-section along span for 15 deg AOA

3.6. Numerical Simulation

3.6.1. Circular Cylinder

Defining the parameters for the flow fluid problem dictates the quality of the CFD solution. Within the pre-processing stage, accuracy is influenced by key factors such as:

a) Defining the solution domain.

b) Generating the mesh.

c) Determining physical modeling parameters.

d) Specifying fluid properties.

e) Setting boundary conditions.

a) Solution Domain

The solution domain defines the abstract environment where the solution is calculated. The shape of the solution domain can be circular or rectangular. The choice of solution domain shape and size can affect the problem's solution.

However, the domain selected for the study is rectangular, as per the tank configuration, which is 2000 mm $\times$ 500 mm.

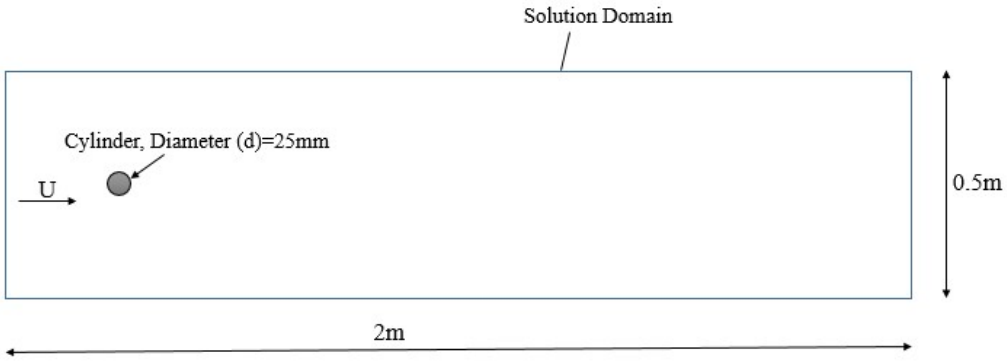

Figure 3.23: Domain for circular cylinder

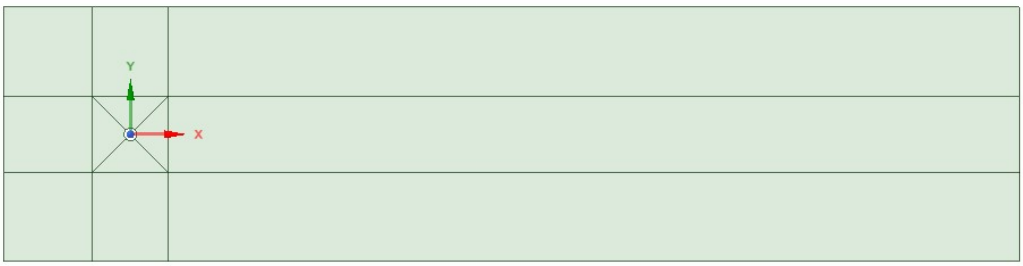

x

Figure 3.24: Geometry for circular cylinder

b) Mesh generation

Structured (regular) grid: This regular grid structure consists of non-crossing grid lines within groups, with each group crossing every member of other groups only once. It's the simplest grid with four neighbors in 2D and six in 3D, making programming and algebraic equation system matrices simpler, but suitable only for geometrically simple solution domains.[28].

Block-Structured grid: On this type of grid, the solution domain is divided into two or more subdivisions. Each subdivision contains blocks of structured grids patched together. Special treatment is needed at block interfaces.

Figure 3.25: Mesh generation with 308088 elements

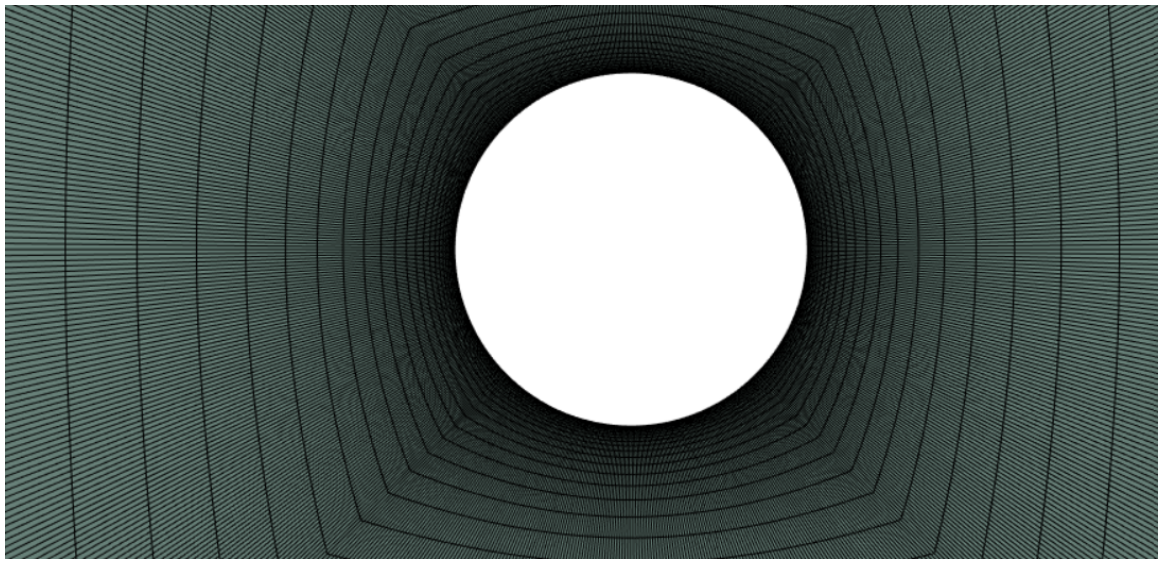

Figure 3.26: Mesh generation (close-up)

Table 3.5: Mesh quality chart

Average skewness	0.14939
Maximum skewness	0.5
Minimum skewness	1.3057e-10

c) Solver settings

The solver settings chosen for circular cylinder is provided in table 3.6.

Table 3.6: Solver Settings for Circular Cylinder

Parameters	**Circular Cylinder**
Pressure velocity coupling	Coupled
Pressure Second order discretization	Second order discretization
Momentum	Second order implicit
No. of time steps	500
Time step size	0.05
Solver type	Transient
Convergence criteria	error $(\varepsilon) < 0.000001$

3.7. Experimental Analysis

3.7.1. Small channel

In the experimental phase, we conducted a test on a small channel tank to gain practical experience with image processing techniques. The fluid used was water, characterized by a density of $998.2 kg/m^3$ and a viscosity of $1.003 \times 10^{-3} Pa.s$.

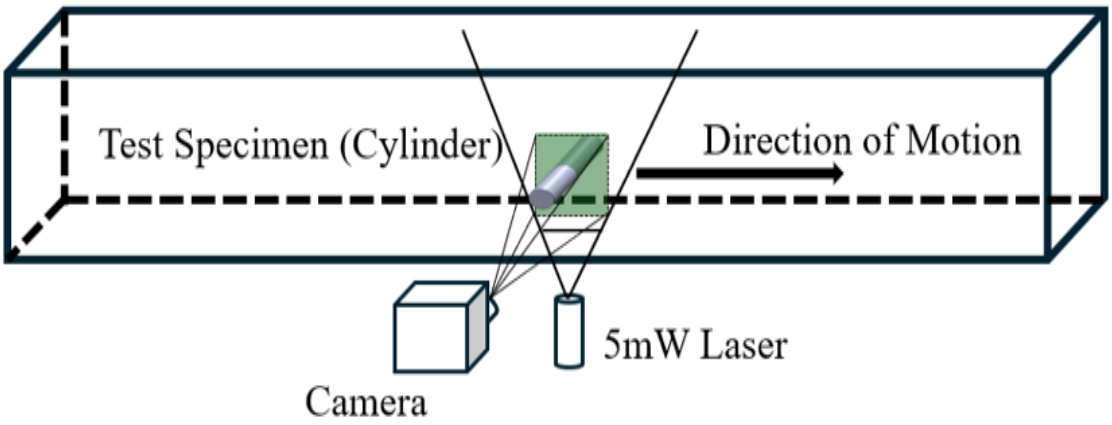

Figure 3.27: Schematic of Small Tank Setup

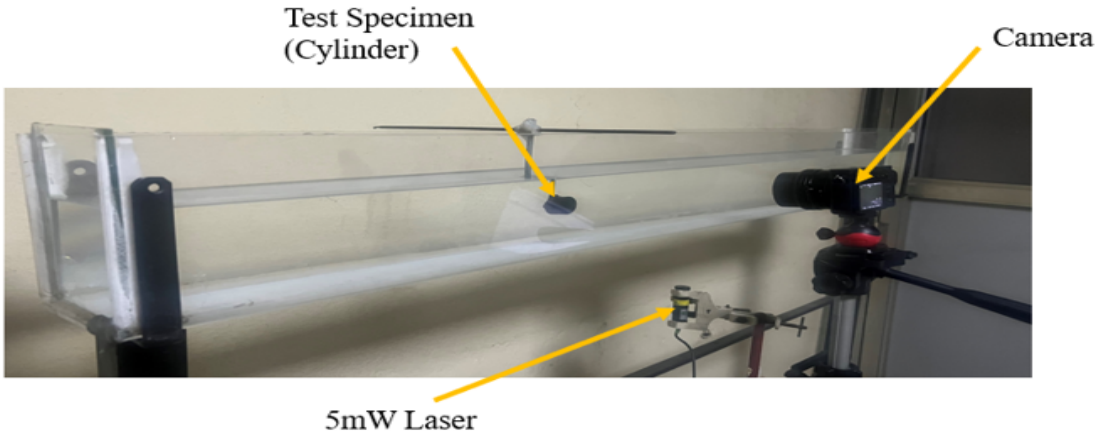

Figure 3.28: Small Tank Setup

1. **Geometrical Parameters:**
   (a) Test specimen: Circular Cylinder
   (b) Diameter: 25 mm
   (c) Small tank dimensions: $1220mm \times 150mm \times 100mm$
   (d) Water Volume: $2.25 \times 10^3 m^3$
   (e) Particle size: 3-5 pixels at a resolution of 1920×1080
2. **Flow Parameters:**
   (a) Velocity: 0.12 m/s
   (b) Reynolds number: 2293
3. **Image Generation**
   Images were captured during the large tank test using the Sony Alpha 6000 camera. The resulting frames had a frame rate of 25 fps. Image size had been 1440*1080.
4. **PIV Image Pre-Processing**
   The overall PIV processing was carried out using the PIVlab toolbox in MATLAB. The images captured from the camera in both tests were affected by noise from particle dust and background illumination, as shown in Figure 3.29. Therefore, these issues needed to be addressed before proceeding.

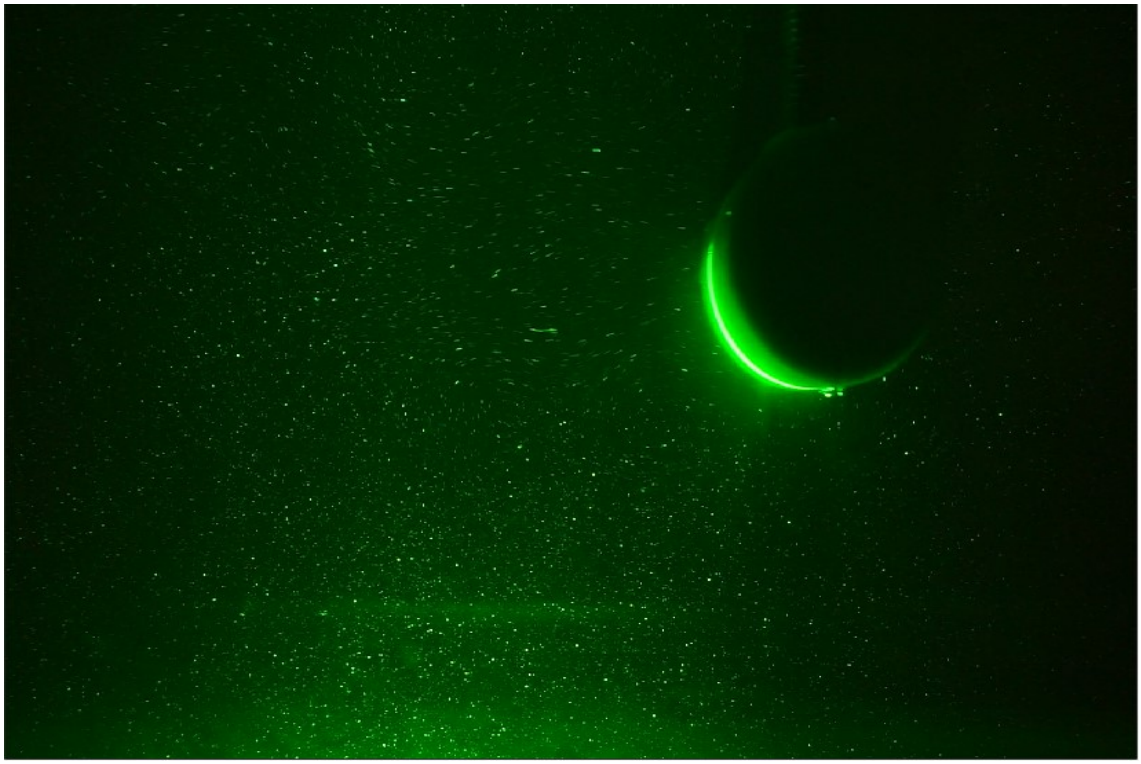

Figure 3.29: Raw image from Sony Alpha 6000

(a) **Image Segmentation**

Inbuilt functions from the PIVLAB toolbox were utilized to preprocess the above images. These functions, listed in Table 3.7, operate on the grayscale image of the input image to refine the image, resulting in higher correlation accuracy.

Table 3.7: Image Segmentation Functions

S.N.	Parameters	Function Settings
1	CLAHE Window size	64 px
2	High bypass Kernel size	15 px
3	Intensity capping	Yes
4	Wiener2 denoise and Low Pass Window size	3 px
5	Mean Intensity Subtraction	Yes

(b) **Manual Masking**

Manual masking provides a good result with a better mask covering all the regions that need to be masked. However, it is a tedious process to manually mask all the frames and is very time-consuming if the total number of experiments and the number of frames in each experiment are both high.

For this experiment, manual masking had been applied.

Figure 3.30: Manual masking

(c) **PIV Settings**

Table 3.8: PIV Settings for the analysis

Parameter	**Value**
PIV Algorithm	FFT window deformation
Pass 1	-
Interrogation area (px)	64
Interrogation Step (px)	32
Pass 2	-
Interrogation area (px)	32
Interrogation Step (px)	16
Sub-pixel estimator	Gauss 2 $\times 3-$ *point*

(d) **Calibration**

The circular cylinder was used for the calibration of the image. The data used for the calibration is summarized in table 3.9.

Table 3.9: Calibration Parameters

Parameter	Value
Reference Length (mm)	286.49
Real Distance (mm)	25
Time Step (ms)	40

5. **Post Processing of Image** Post-processing of PIV data is crucial for obtaining reliable results, and various techniques are employed in PIVlab to enhance data quality.

3.7.2. Large Tank

Large towing tank was used for the further experimental analysis for baseline wing and wing with vortex generator. Also, the setup characterization experiment for circular cylinder was performed. The fluid used was water, characterized by a density of $998.2 kg/m^3$ and a viscosity of $1.003 \times 10^{-3} Pa.s$.

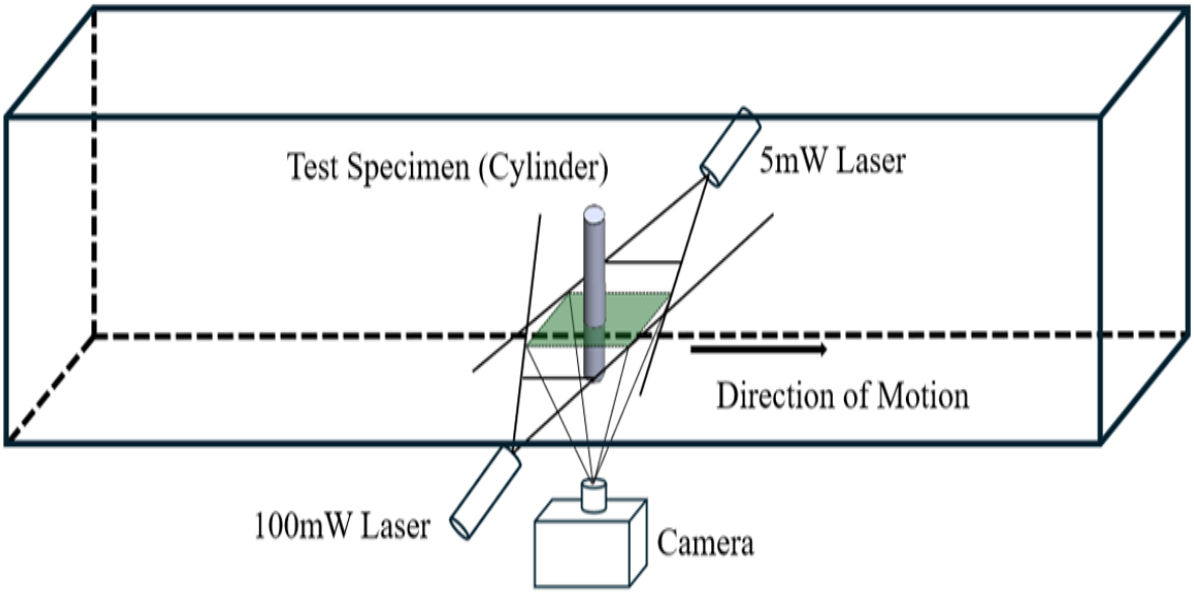

Figure 3.31: Schematic of Large Tank Setup

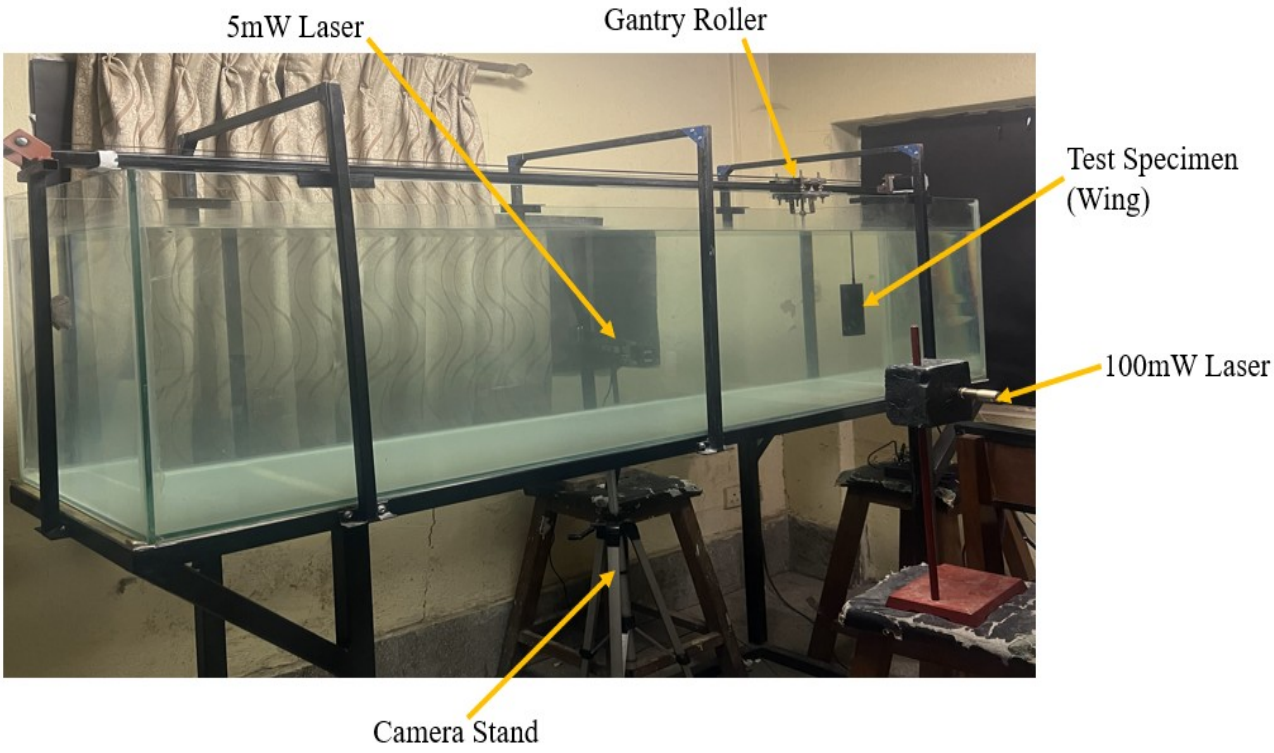

Figure 3.32: Experimental Setup (Large Tank)

1. **Geometrical Parameters for circular cylinder:**
   (a) Test specimen: Circular cylinder
   (b) Diameter: 25 mm
   (c) Length: 15 cm
2. **Geometrical Parameters for wing:**
   (a) Test specimen: Airfoil NACA (2412)
   (b) Chord: 75 mm
   (c) Span: 16.667 cm
3. **Geometrical Parameters for wing with VG:**
   (a) VG height: 5 mm
   (b) Distance between a pair of VG: 35 mm
   (c) Deflection angle: 12 degree
4. **Experimental Parameters:**
   (a) Airfoil velocity: 0.1756 m/s

(b) Reynolds number: 4369 (for cylinder), 13107 (for wing)

(c) Large tank dimensions: $2m \times 0.5m \times 0.6m$

(d) Water Volume: 500 litres ($0.5m^3$)

(e) Particle size: 4-6 pixels at a resolution of 1920×1080

5. **Image Generation**

   Images were captured during the large channel test using an iPhone 13 Pro camera and Sony Alpha 6000. The resulting frames had a frame rate of 120 fps for circular cylinder and 50 fps for wing and wing with VGs.

6. **Particle concentration**

   The concentration of tracer particles was analysed in the interrogation window of size 64*64 pixels, with at least 7-13 particles detected in the particular interrogation window.

   The mass estimation of seeding particles was done such that 8 particles were present in 1 mm^3 of water volume. [20] The calculated overall mass dispersed within the large channel tank is 3.738 gm.

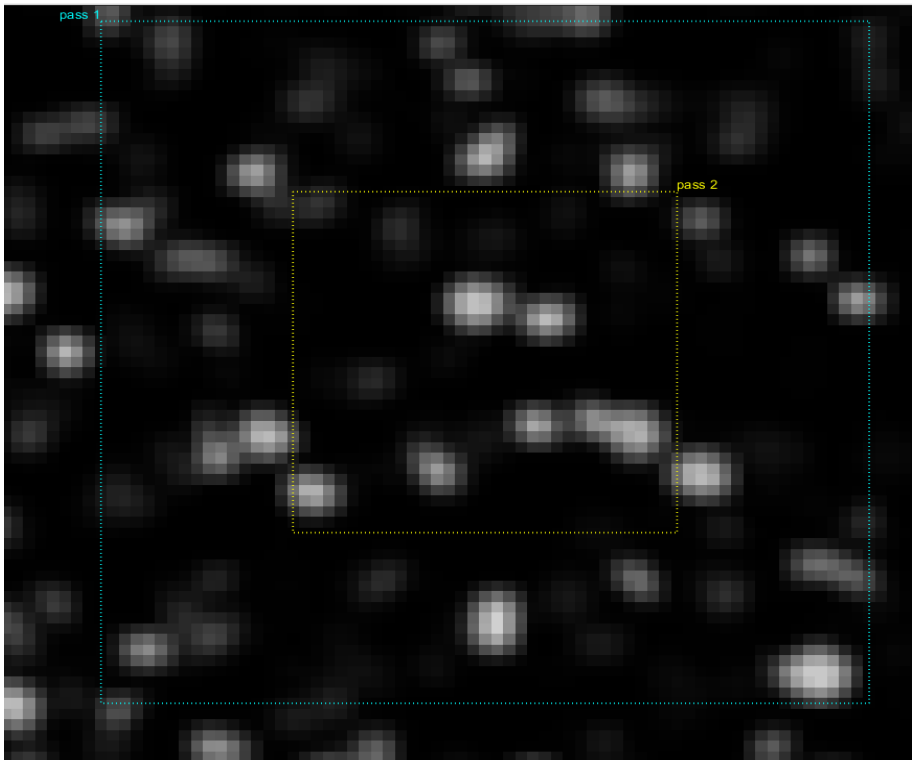

Figure 3.33: Particle size concentration

7. **PIV Image Pre-Processing**

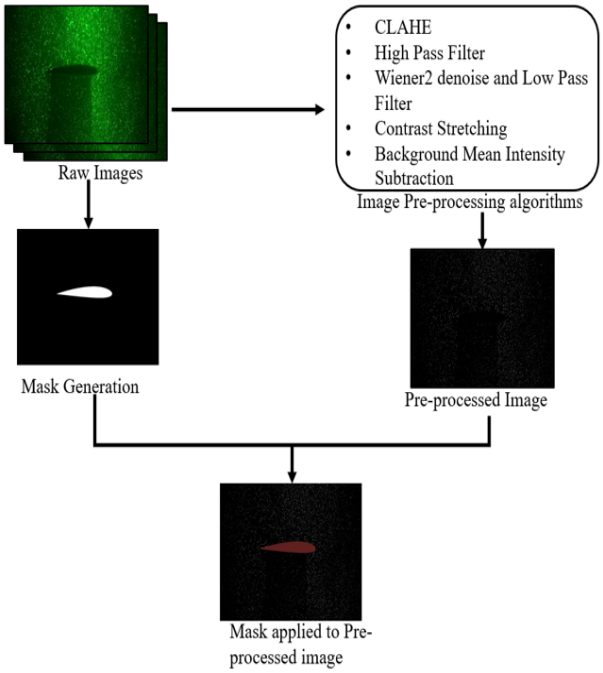

Figure 3.34: Image Pre-processing Flowchart

The overall PIV processing was carried out using the PIVlab toolbox in MATLAB. The images captured from the camera in both tests were affected by noise from particle dust and background illumination, as shown in Figure 3.35. Therefore, these issues needed to be addressed before proceeding.

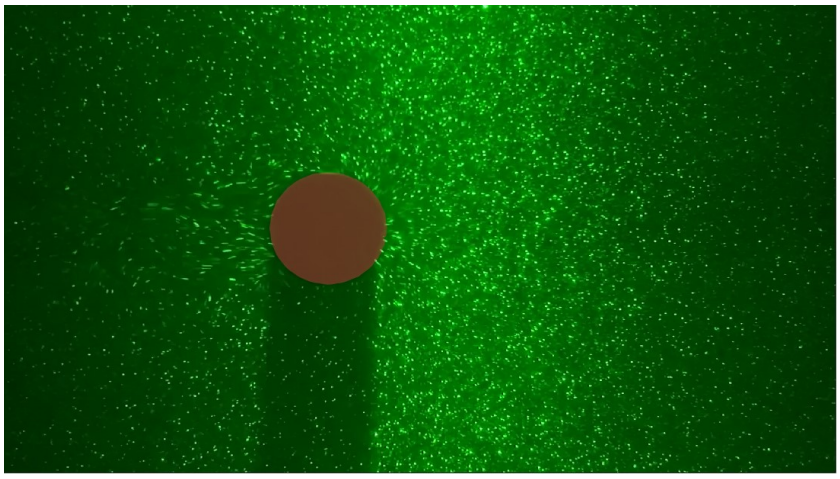

Figure 3.35: Raw image of circular cylinder (with mask)

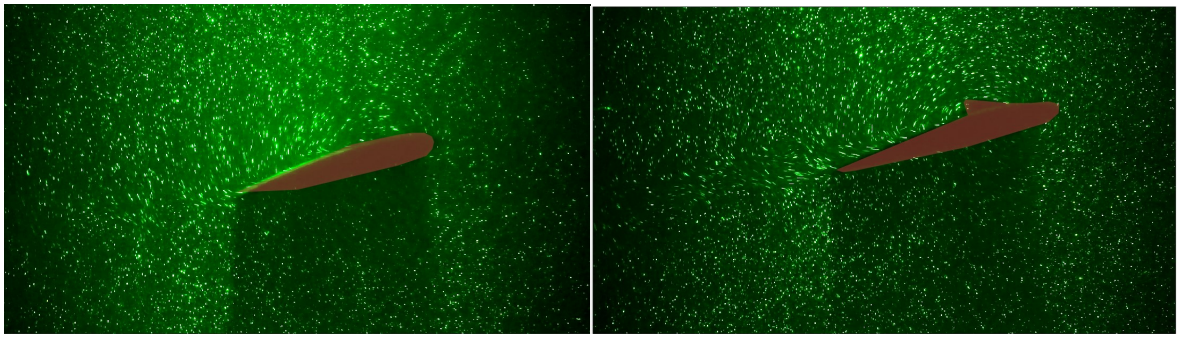

(a) Raw image of baseline wing (with mask) (b) Raw image of wing with VG (with mask)

Figure 3.36: Comparison of wing raw images

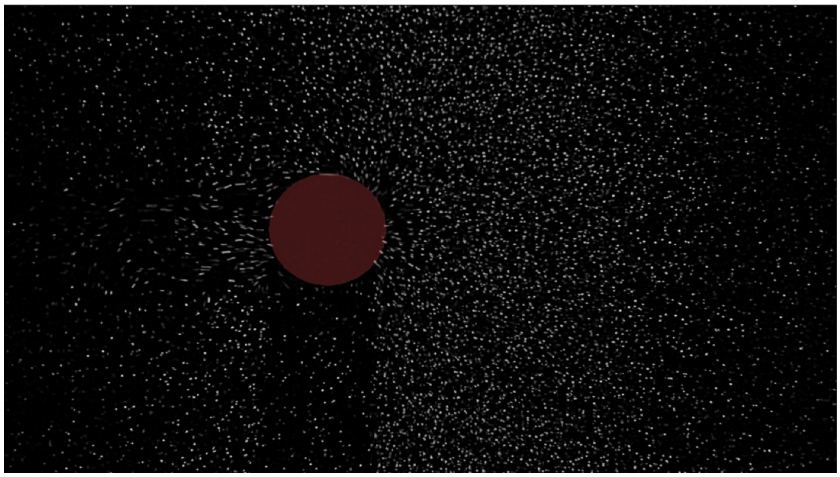

Figure 3.37: Pre-processed image of circular cylinder

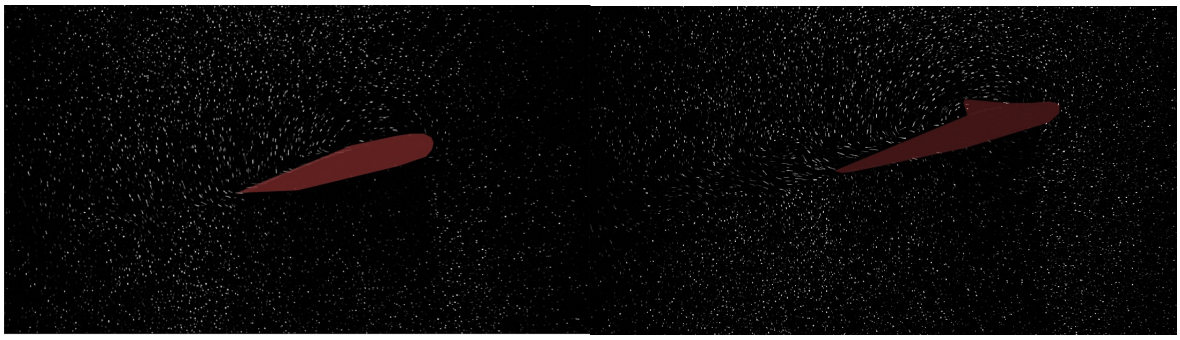

(a) Pre-processed image of baseline wing (b) Pre-processed image of wing with VG

Figure 3.38: Comparison of wing pre-processed images (with mask)

(a) **Image Segmentation**

Inbuilt functions from the PIVLAB toolbox were utilized to preprocess the above images. These functions, listed in Table 3.10, operate on the grayscale image of the input image to refine the image, resulting in higher correlation accuracy.

Table 3.10: Image Segmentation Functions

S.N.	Parameters	Function Settings
1	CLAHE Window size	64 px
2	High bypass Kernel size	15 px
3	Intensity capping	No
4	Wiener2 denoise and Low Pass Window size	3 px
5	Auto Contrast Stretch	min = 0.0156863 and max = 1
6	Mean Intensity Subtraction	Yes

(b) **Uniform velocity Masking**

Uniform velocity masking provides a good result with a better mask covering all the regions that need to be masked. It is performed through the code.

For this experiment, uniform velocity masking has been applied. Also, for the exact retention of shape in the shadow region, the co-ordinates of cylinder and wing is imported in MATLAB and the matlab generated mask is utilized.

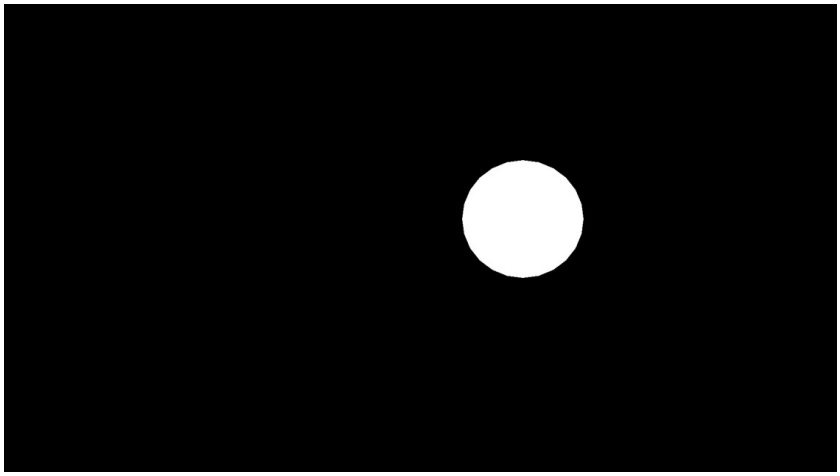

Figure 3.39: Matlab generated mask for circular cylinder

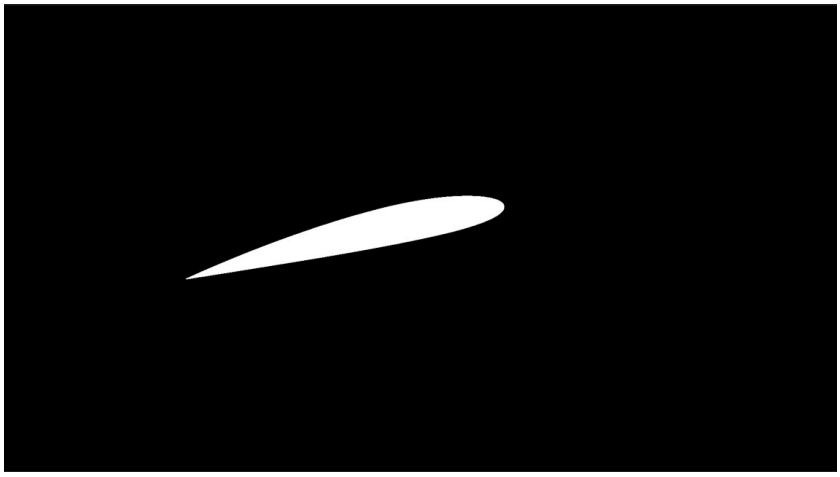

Figure 3.40: Matlab generated mask for baseline wing

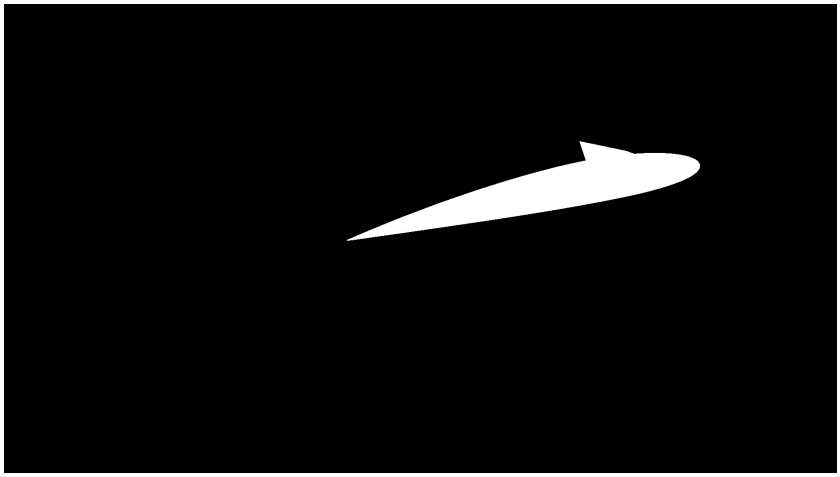

Figure 3.41: Matlab generated mask for wing with VG

(c) **PIV Settings**

Table 3.11: PIV Settings for the analysis

Parameter	**Value**
PIV Algorithm	FFT window deformation
Pass 1	-
Interrogation area (px)	64
Interrogation Step (px)	32
Pass 2	-
Interrogation area (px)	32
Interrogation Step (px)	16
Sub-pixel estimator	Gauss $2 \times 3 - point$

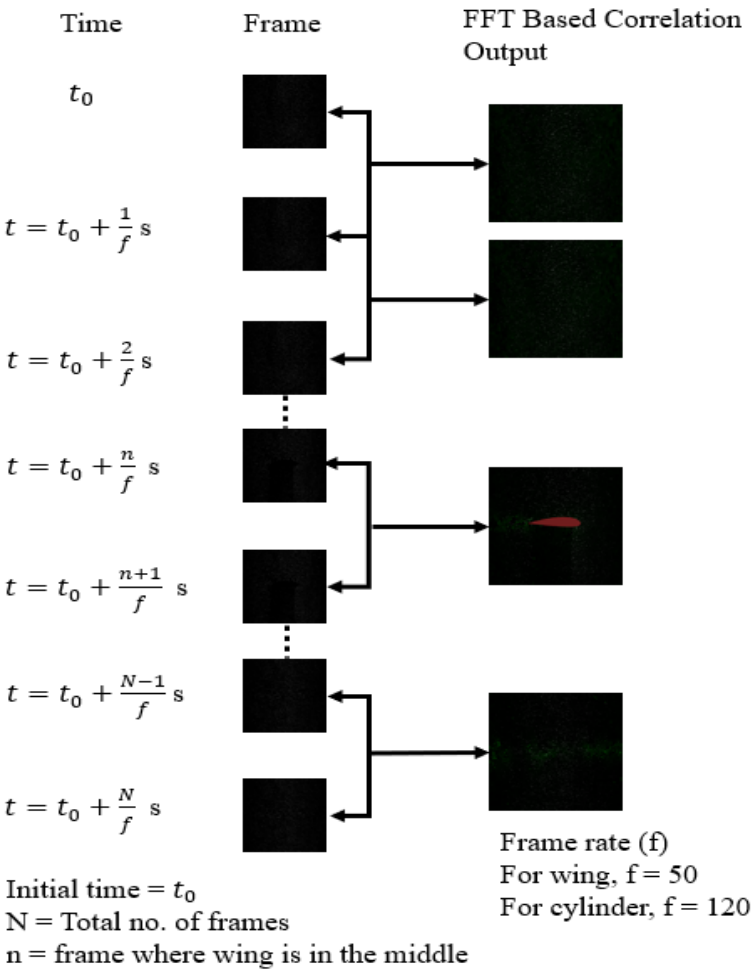

Figure 3.42: FFT Result Representation

(d) **Calibration**

Calibration of circular cylinder

The image of the circular cylinder with a known diameter distance was used for the calibration of the image. The data used for the calibration is summarized in table 3.12.

Table 3.12: Calibration Parameters for circular cylinder

Parameter	**Value**
Reference Length (pixel)	254.25
Real Distance (mm)	25
Time Step (ms)	8.333

Calibration of wing

The image of the wing with known chord was used for the calibration of the wing image. The data used for the calibration is summarized in table 3.13.

Table 3.13: Calibration Parameters for wing

Parameter	**Value**
Reference Length (pixel)	800.54
Real Distance (mm)	75
Time Step (ms)	20

8. **Post Processing of Image** Post-processing of PIV data is crucial for obtaining reliable results, and various techniques are employed in PIVlab to enhance data quality.

   (a) **Data Validation** Post-processing of PIV data involves manual selection or semi-automatic determination of velocity limits. Outlier filtering method had been used for the data validation.

   (b) **Data Interpolation and Smoothing** Smooth and High vectors were enabled to get smooth images.

   (c) **Data Exploration** Vector maps, v-velocity contour, vorticity contour and velocity contour were explored to extract the images.

CHAPTER FOUR: RESULT AND DISCUSSION

The extracted videos and images were imported to PIVLab for visualization of velocity and vorticity contours of flow past a circular cylinder, baseline wing and wing with VGs. The above pre-processing and post-processing settings mentioned in the methodology section were applied and the final results are presented in the following sections.

4.1. Flow Visualization for small channel circular cylinder

The pre-processed images were further processed in PIVLAB to obtain the velocity and vorticity contours, as shown in figures 4.1 and 4.2 respectively. Counter-rotating vortices can be visualized from the counter at opposite ends of the circular section. One end has a distinguishing circular arc whereas the arc at other end is not visible because of the mask applied to cover the shadow region. This problem was mitigated in the large tank setup by the application of two lasers, with nearly meshed illuminated laser planes, at opposite ends.

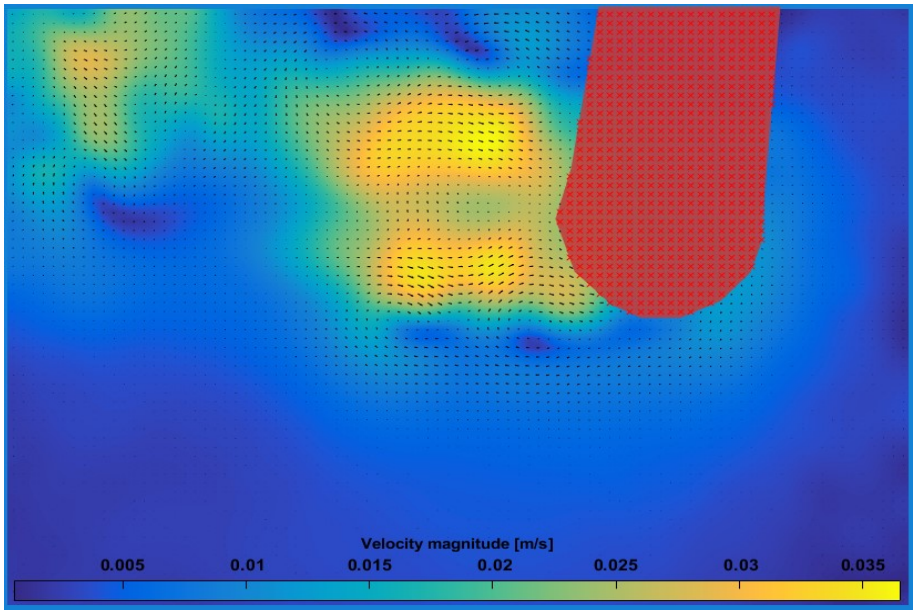

Figure 4.1: Velocity Contour

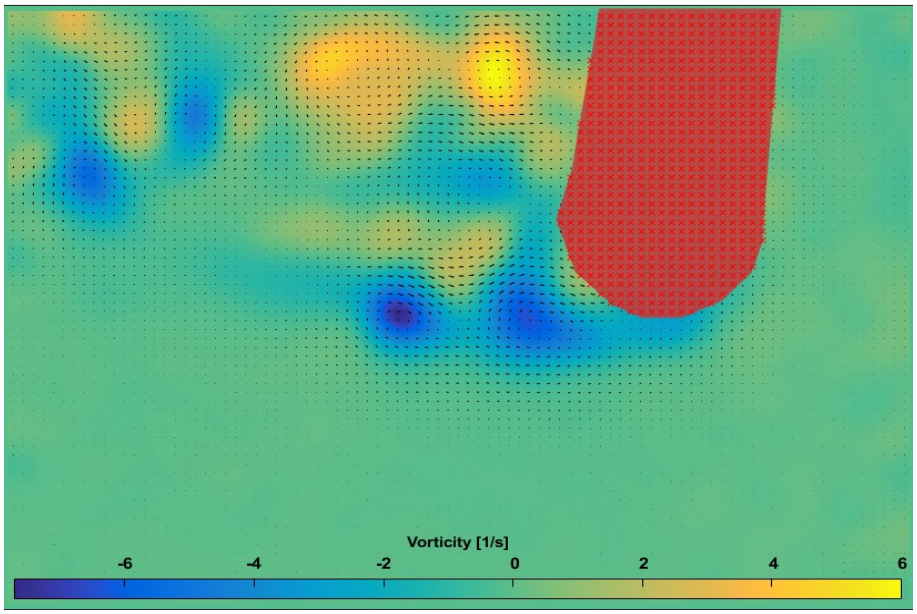

Figure 4.2: Vorticity contour

A code was also developed for image processing. The code basically incorporated the cross correlation algorithm and optical algorithm.So, the hybrid PIV algorithm was implemented successfully as shown in the appendix section. The velocity and vorticity streamlines obtained from the code are shown in figures 4.3 and 4.4.

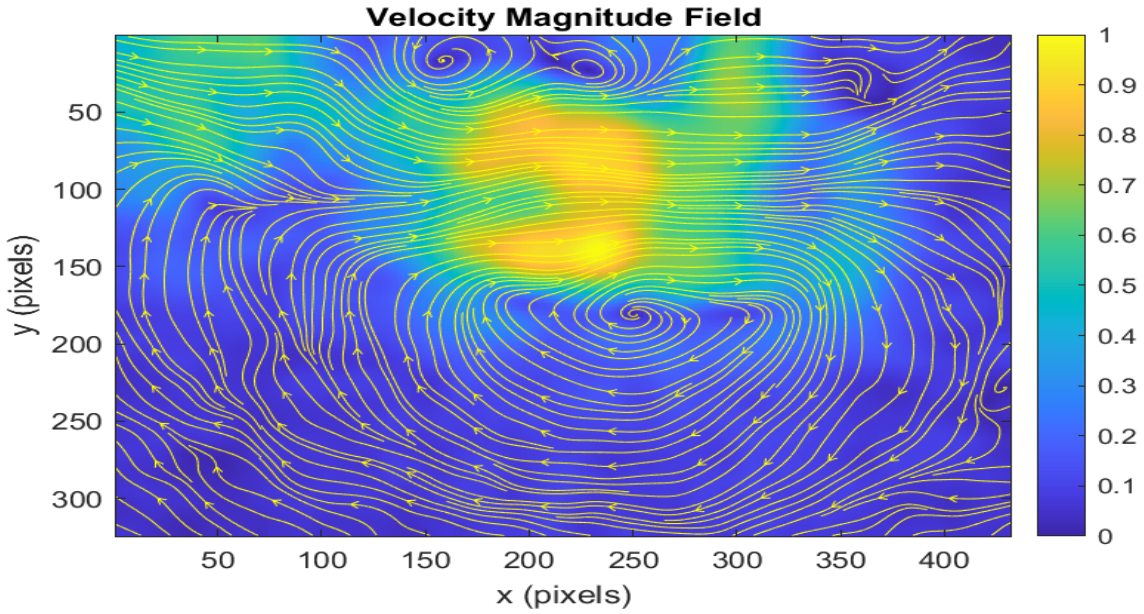

Figure 4.3: Velocity field of wake region behind a cylinder

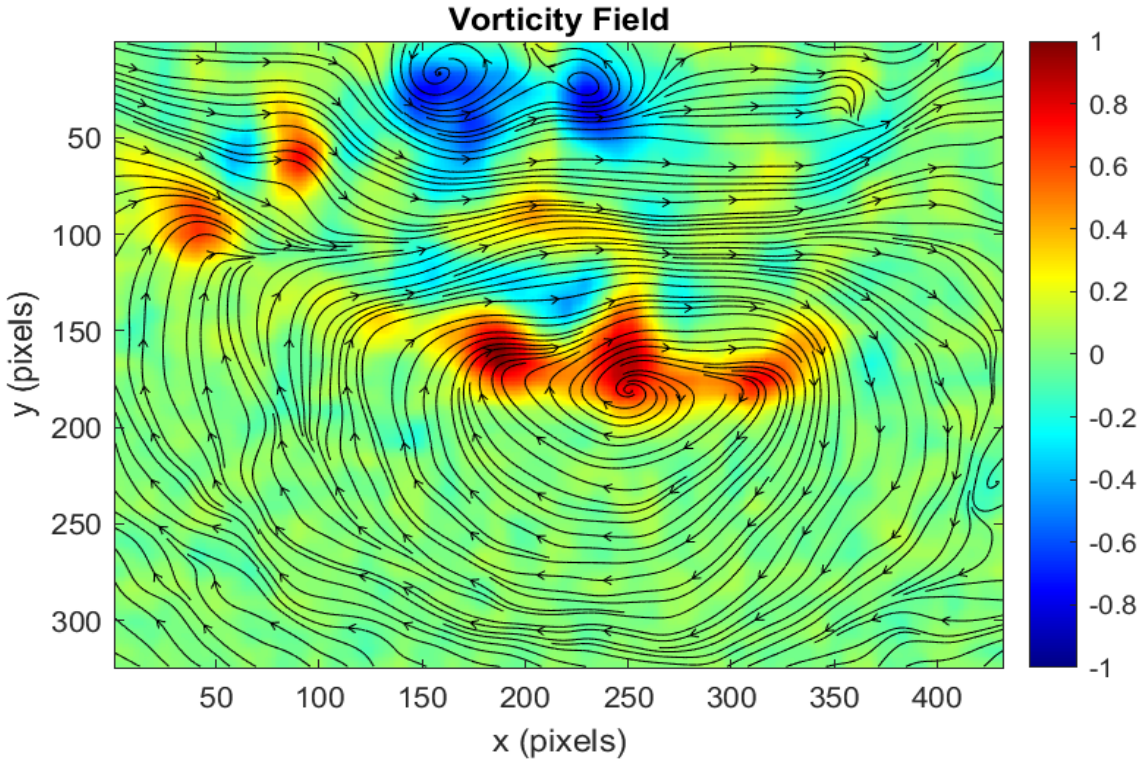

Figure 4.4: Vorticity field of wake region behind a cylinder

4.2. Setup Characterization Through Flow Past a Circular Cylinder

For the characterization of the existing PIV setup in Pulchowk Campus, the experimentally and numerically calculated strohaul number of circular cylinder was compared with the experimental data from the reference paper, and the setup was validated with error calculation.

4.2.1. Comparison of numerical simulation with experimental data from reference paper

A study of the numerical simualtion had been done to characterize the piv setup. The numerical simulations were first validated with a experimental data for 50mm diameter obtained from orucc's [4] . At Reynolds number 3350, 6850 and 10,200, the strouhal number had been verified to ensure the correctness of the scheme. The Strouhal number obtained from the numerical simulation and experimental data had been compared in table 4.1.

Table 4.1: Comparison of Experimental and Numerical Simulation Data with Error [4]

Reynolds number	**Experimental data (St)** [4]	**Numerical Simulation (St)**	**Error(%)**
3350	0.2	0.2078	3.9
6850	0.19	0.1892	-0.421052632
10,200	0.18	0.1803	0.166666667

This ensured us the scheme that validates the result with certain numerical errors. For the Reynolds number of 4369, the numerical simulations of unsteady flow past a cylinder had been studied and from which the Strouhal number was found to be 0.196.
Also, the obtained result validates linear relationship between Karman vortex shedding frequency (f) and Reynolds number(Re) for bare cylinder. (which is also in agreement with Prasad and Williamson [29])

4.2.2. Numerical Simulation for Circular Cylinder (25mm diameter)

1. **Mesh independence study for circular cylinder**
   Mesh independence study was conducted with drag coefficient as the convergence parameter. From the study (tabulated in table 4.2), the values of drag coefficient started converging after reaching the mesh elements number equal to 77730 and the change in C_d at elements number greater than 308088 was minimum. Hence, 308088 was chosen to be the optimum mesh number.

Table 4.2: Grid Independence Study

Simulation Number	No. of Elements	Cd(trough)	Cd(crest)
1	10352	1.198	1.30764
2	17896	1.1768	1.3174
3	38666	1.1205	1.25667
4	77730	1.10489	1.2556
5	166656	1.10462	1.21337
6	308088	1.104	1.2125

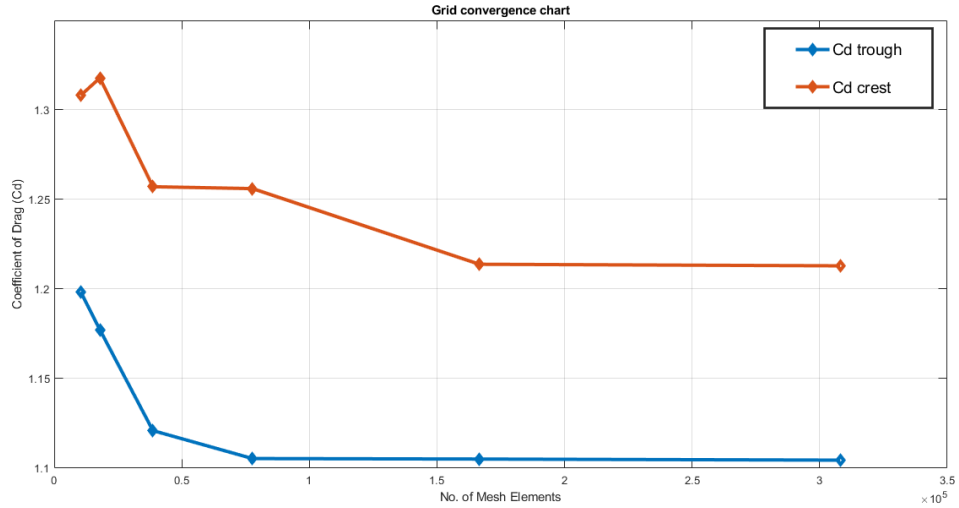

Figure 4.5: Coefficient of drag variation with mesh number

2. **Coefficient of lift and drag variation with flow time**

   As can be seen in the figures 4.6 and 4.7, the lift and drag coefficients fluctuate periodically, which is due to the separation of fluid layer at opposite ends of the cylinder which results in the formation of counter-rotating vortices. The frequency of formation of these vortices was obtained from the figure 4.7 and is equal to 1.37 Hz.

   Using the frequency, the strouhal number was calculated and was equal to 0.196. The obtained data had been validated with King's [3] work and the C_d vs Reynolds number plot data which states that C_d should be in range of 1.1 to 1.3 for Reynolds number range between 1000 to 10000 [30].

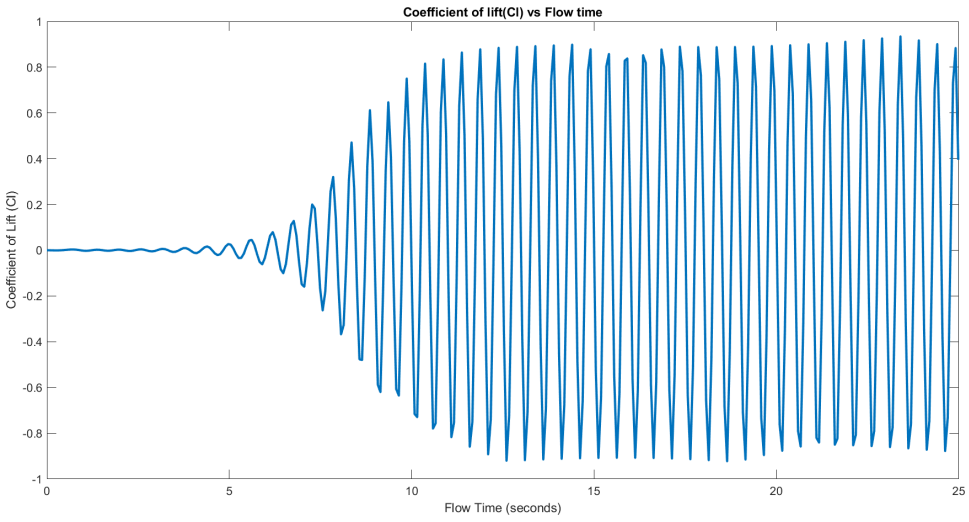

Figure 4.6: Coefficient of lift(Cl) vs flow time

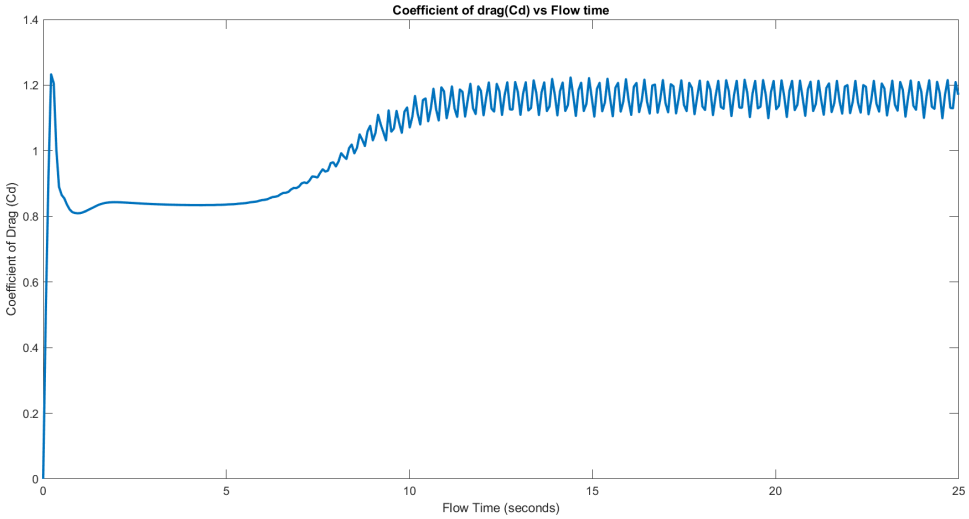

Figure 4.7: Coefficient of drag(Cd) vs flow time

3. **Contour plot of the flow past circular cylinder**

   The obtained velocity-contour plot for the circular cylinder is shown in figure 4.8.

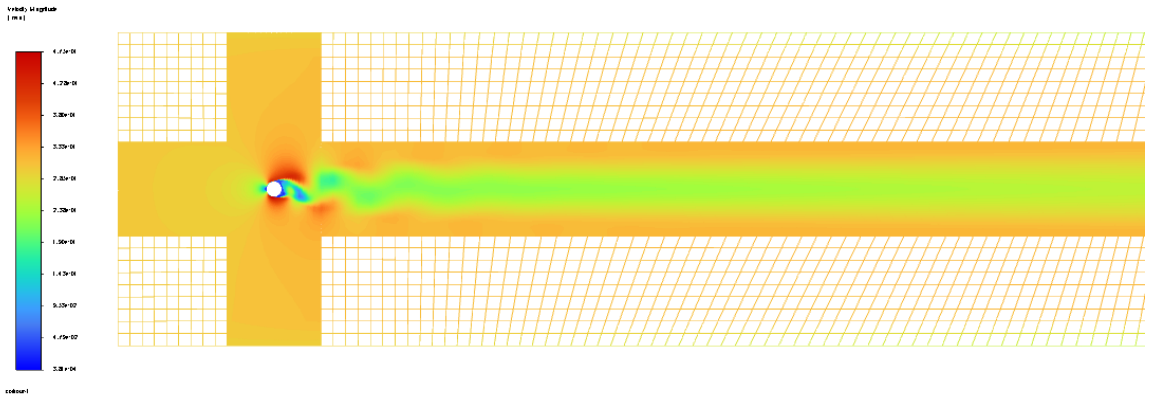

Figure 4.8: Pathlines-contour plot for velocity magnitude (mesh number:308088)

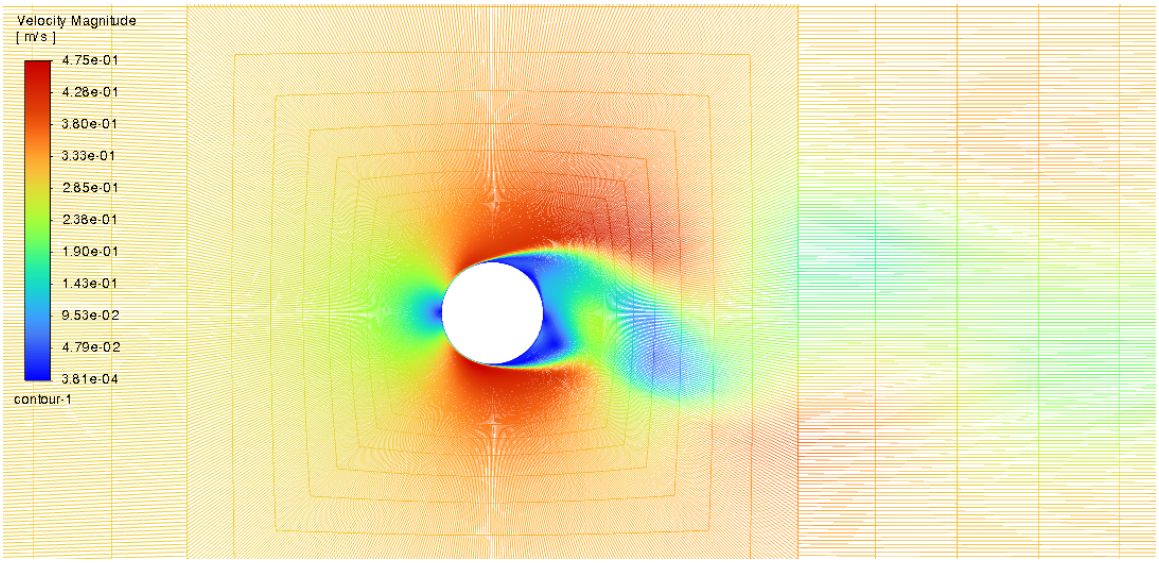

Figure 4.9: Pathlines-contour plot for velocity magnitude (mesh number:308088)

The pathlines line contour in figure 4.9 shows the flow (velocity) field at any instant of time and the separation of the fluid layer along with the formation of counter-rotating vortices can be seen clearly.

4.2.3. Time Resolved Flow Characteristics for circular cylinder on Large Water Tank

The time-resolved flow patterns of circular cylinder were analyzed by conducting three distinct experiment to characterize the Particle Image Velocimetry (PIV) setup. Velocity and vorticity contours were examined for the same points, revealing unique flow behaviors associated with each cylinder configuration.

The velocity contours for three different runs are presented in the figures 4.10, 4.11, and 4.12.

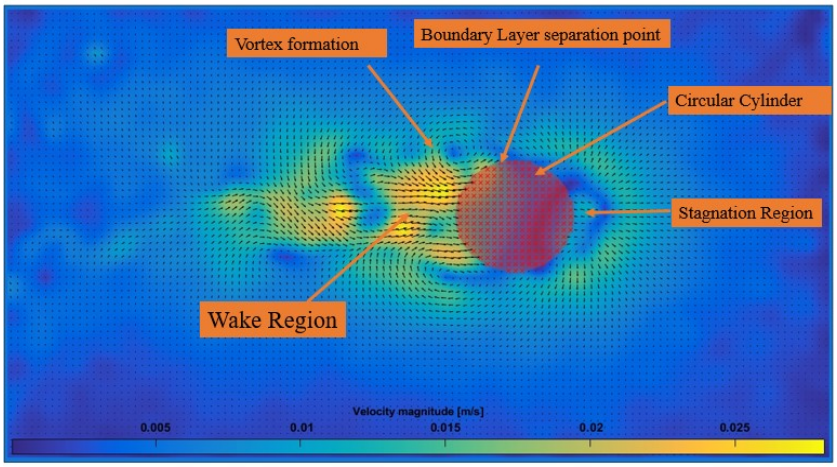

Figure 4.10: Velocity magnitude plot of flow across circular cylinder(Run I)

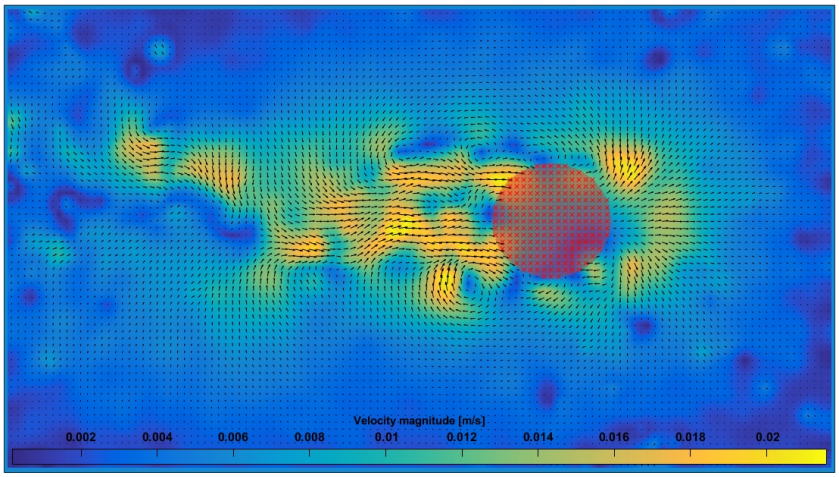

Figure 4.11: Velocity magnitude plot of flow across circular cylinder (Run II)

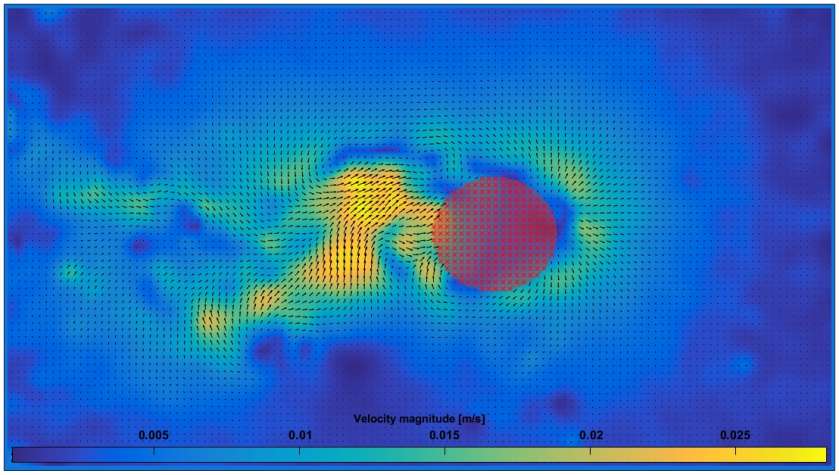

Figure 4.12: Velocity magnitude plot of flow across circular cylinder (Run III)

The vorticity contours for three different runs are shown in the figures 4.13, 4.14, and 4.15.

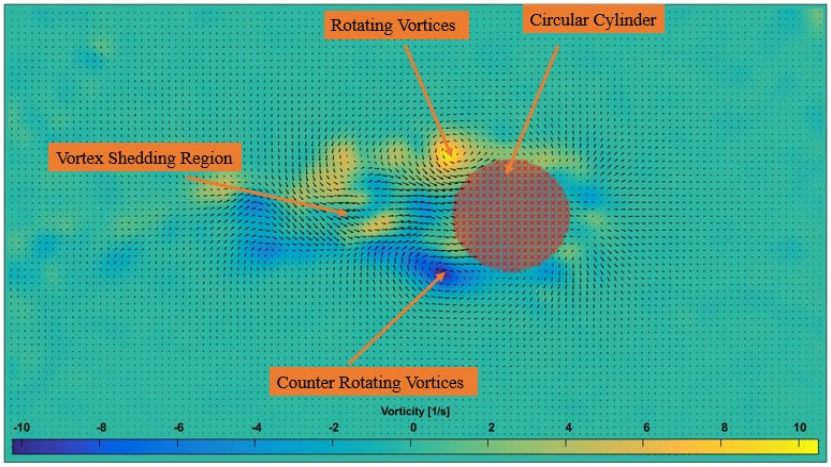

Figure 4.13: Vorticity plot of flow across circular cylinder (Run I)

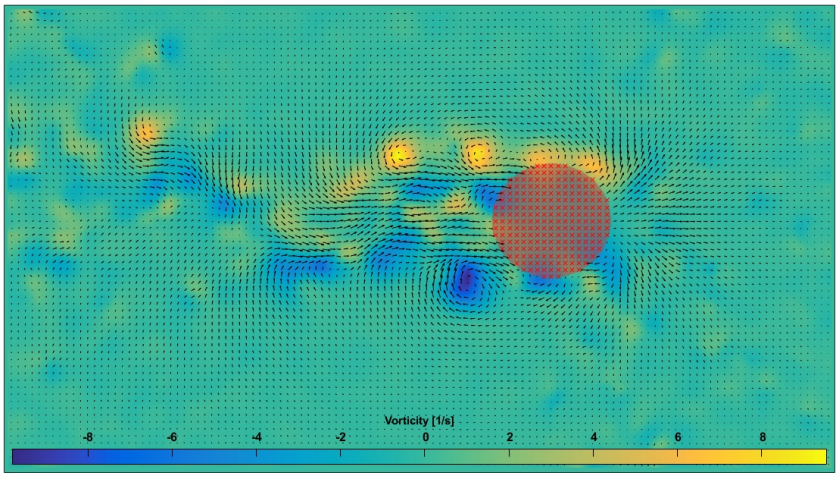

Figure 4.14: Vorticity plot of flow across circular cylinder (Run II)

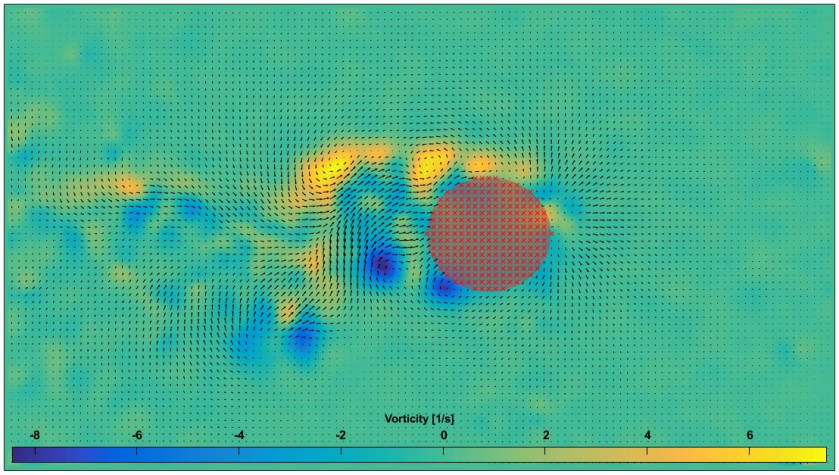

Figure 4.15: Vorticity plot of flow across circular cylinder (Run III)

The vorticity plot obtained from three different raw videos capture vortex shedding behind

the object for a flow at low Reynold's number.

4.2.4. Amplitude Spectral Analysis of the Flow Field

Utilizing Fast Fourier Transformation (FFT) for mean vorticity (1/s) data, spectral analysis was conducted to investigate flow structures within the wake region. The analysis unveiled dominant frequency values, crucial for identifying vortex shedding phenomena. Peaks observed in the spectral analysis confirmed characteristic flow frequencies, supported by the provided number of time-dependent vorticity data points. Moreover, the number of time-dependent vorticity data were 90. It is certain that the peak in the spectral analysis indicates the dominant frequency of the vortex shedding, f (Hz) evidently.

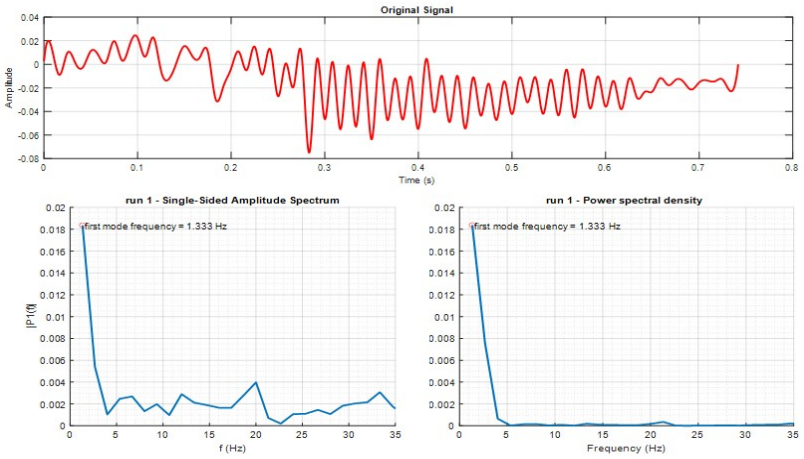

Figure 4.16: Single Sided Amplitude Spectrum and PSD for cylinder (Run I)

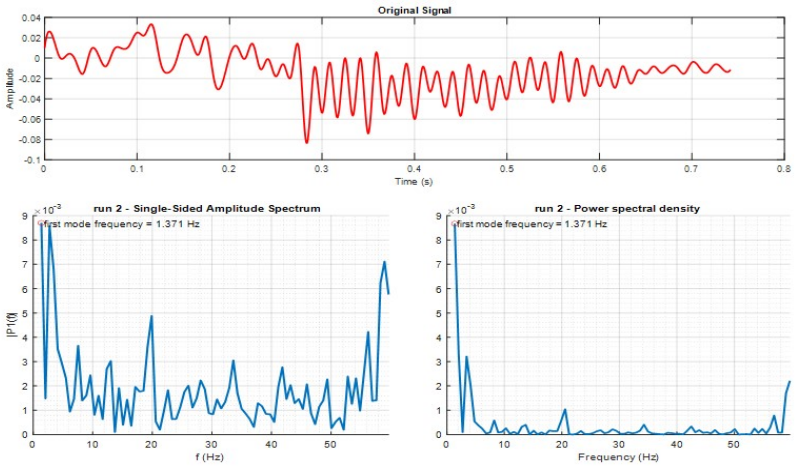

Figure 4.17: Single Sided Amplitude Spectrum and PSD for cylinder (Run II)

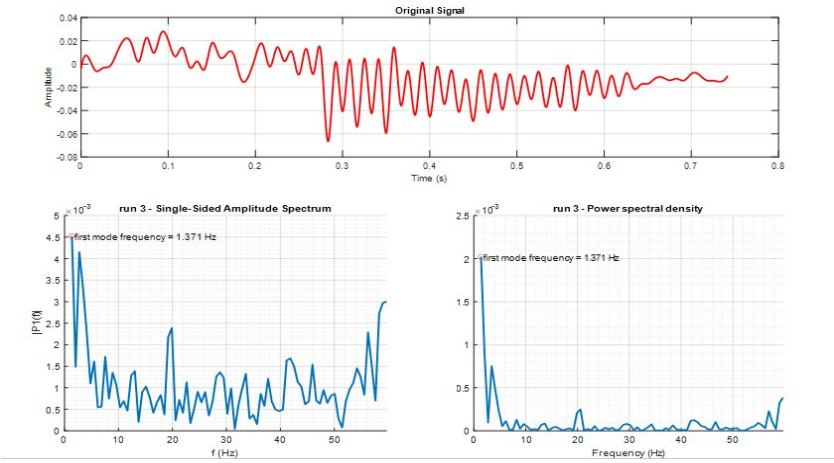

Figure 4.18: Single Sided Amplitude Spectrum and PSD for cylinder (Run III)

4.2.5. PIV Setup Characterization

Following the spectral analysis, Strouhal numbers were calculated based on the obtained dominant frequencies. The relative error of the Strouhal number was determined using the provided formula, comparing experimental and theoretical values.

$$\text{Error } (\%) = \left(\frac{\text{Strouhal number (Experimental)} - \text{Strouhal number (Theoretical)}}{\text{Strouhal number (Theoretical)}} \right) \times 100\%$$

This analysis allowed for an assessment of the setup's accuracy in capturing flow phenomena. The required data, including vortex shedding frequencies, experimental Strouhal numbers, and relative errors, are presented in the table **??**

Table 4.3: Setup Characterization

Run	Vortex shedding Frequency (Hz)	Experimental Strouhal Number	Theoretical Strouhal Number	Relative error (%)
I	1.33331	0.1897	0.1970	3.6777
II	1.37143	0.1952	0.1970	0.9137
III	1.37143	0.1952	0.1970	0.9137

The table provides interpretation about vortex shedding phenomena, comparing experimental and theoretical data across different cases. In Run I, the recorded vortex shedding frequency stands at 1.33331 Hz, resulting in an experimental Strouhal number of 0.1897, slightly diverging from the theoretical prediction of 0.1970, with a relative error of 3.6777%. In contrast, Runs II and III share a vortex shedding frequency of 1.3714 Hz, with an experimental Strouhal number of 0.1952. Despite this, the theoretical Strouhal number remains consistent at 0.1970. The relative error in Runs II and III amounts to 0.9137%, suggesting a closer

agreement between experimental and theoretical values compared to Run I.

4.3. Time Resolved Flow characteristics of Baseline Wing and Wing with VGs

The time resolved flow characteristics for the baseline wing and wing with VGs was studied. The cross-correlation algorithm along with above mentioned settings was employed on wings for visualization and comparison of results obtained from post-processing of PIV images.

4.3.1. Experimental Flow visualization of Wing and Wing with VGs

Velocity and vorticity contours were shown in the following figures at time step 10/50, 27/50, and 35/50.

Baseline wing

The contour plots for velocity magnitude of baseline wing, at three different time steps, are shown in figures 4.19, 4.20, and 4.21.

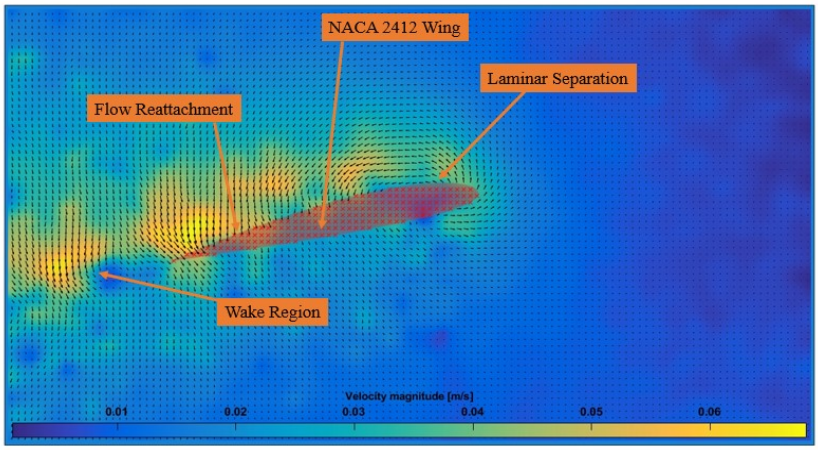

Figure 4.19: Velocity magnitude plot of flow across wing- image 1(time step 10/50)

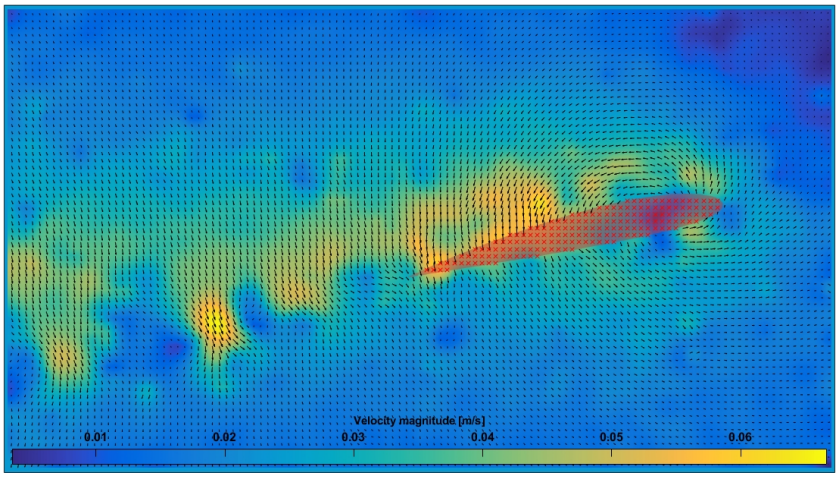

Figure 4.20: Velocity magnitude plot of flow across wing- image 2(time step 27/50)

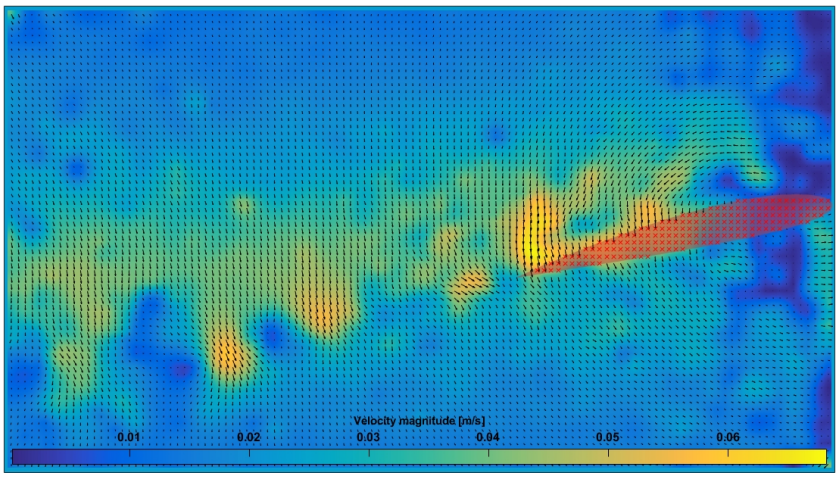

Figure 4.21: Velocity magnitude plot of flow across wing- image 3(time step 35/50)

The contour plots for vorticity of baseline wing, at three different time steps, are shown in figures 4.22, 4.23, and 4.24.

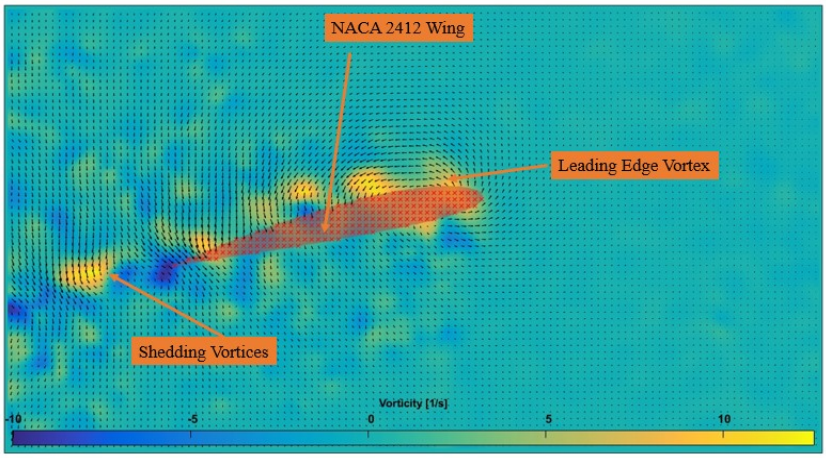

Figure 4.22: Vorticity plot of flow across wing- image 1(time step 10/50)

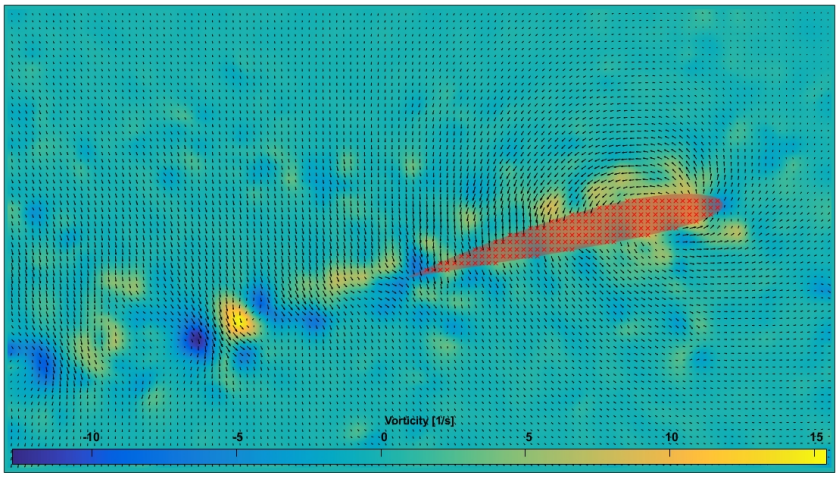

Figure 4.23: Vorticity plot of flow across wing- image 2(time step 27/50)

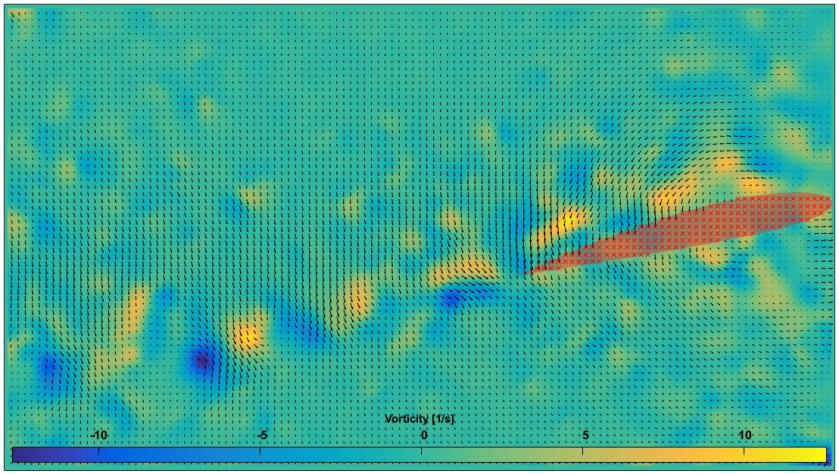

Figure 4.24: Vorticity plot of flow across wing- image 3(time step 35/50)

From the figures, for different time step, it can observed that vortices are being shed from

the location on the upper surface of the wing, just downstream of the leading edge signifying flow separation. Furthermore, the vortex shedding can also be observed at the trailing edge.

Wing with VG

The contour plots of velocity magnitude, at three different time steps, are shown in figures 4.25, 4.26, and 4.27.

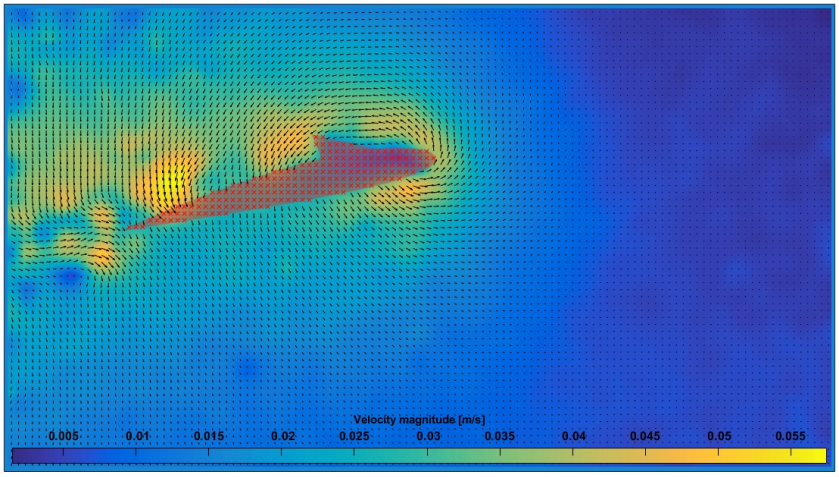

Figure 4.25: Velocity magnitude plot of flow across wing with VG- image 1(time step 10/50)

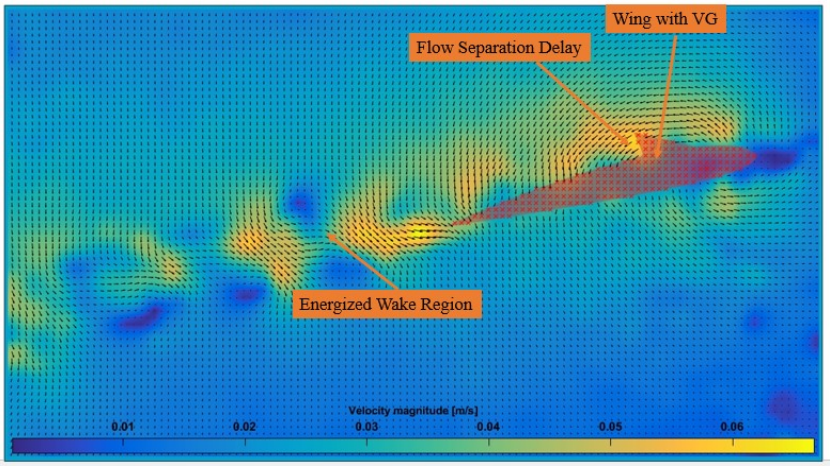

Figure 4.26: Velocity magnitude plot of flow across wing with VG- image 2(time step 27/50)

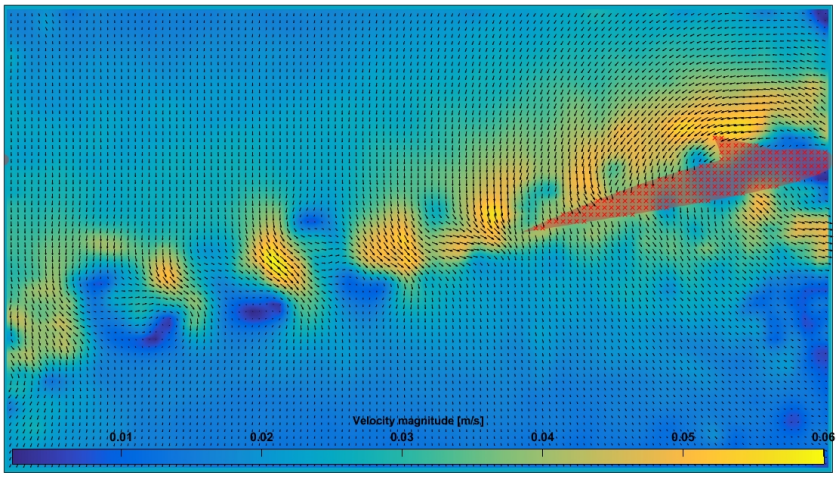

Figure 4.27: Velocity magnitude plot of flow across wing with VG- image 3(time step 39/50)

The contour plots of vorticity of wing with VG, at three different time steps, are shown in figures 4.28, 4.29, and 4.30.

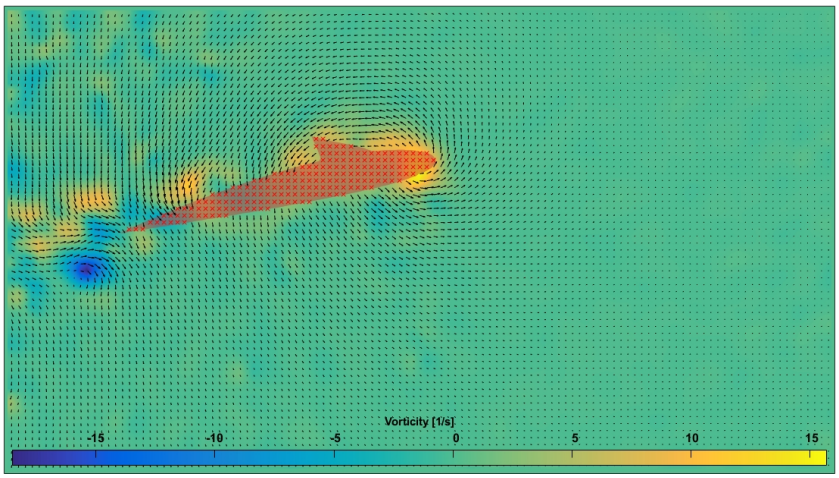

Figure 4.28: Velocity magnitude plot of flow across wing with VG- image 1(time step 10/50)

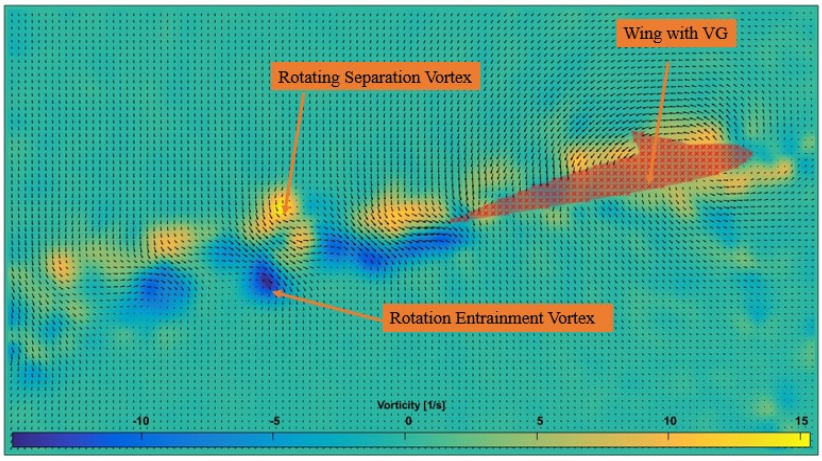

Figure 4.29: Velocity magnitude plot of flow across wing with VG- image 2(time step 27/50)

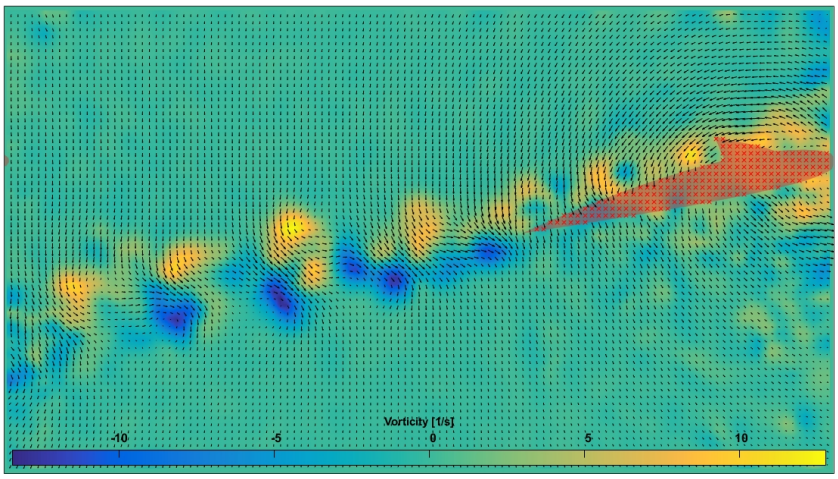

Figure 4.30: Velocity magnitude plot of flow across wing with VG- image 3(time step 35/50)

Compared to the baseline wing, vortex formation location on the upper surface of the wing with VG was delayed downstream signifying possible flow separation delay (can be visualized more clearly in video formats).

4.3.2. Spectral Analysis of the Flow Field to obtain Strouhal number

The FFT analysis for mean vorticity data of the wing and wing with VGs helped to determine the dominant peak using a single-sided amplitude spectrum and power spectral density plot.

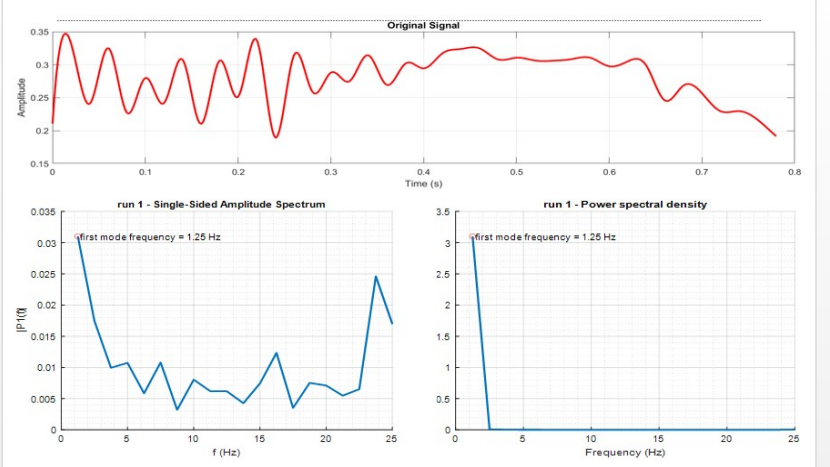

Figure 4.31: Single Sided Amplitude Spectrum and PSD for baseline wing

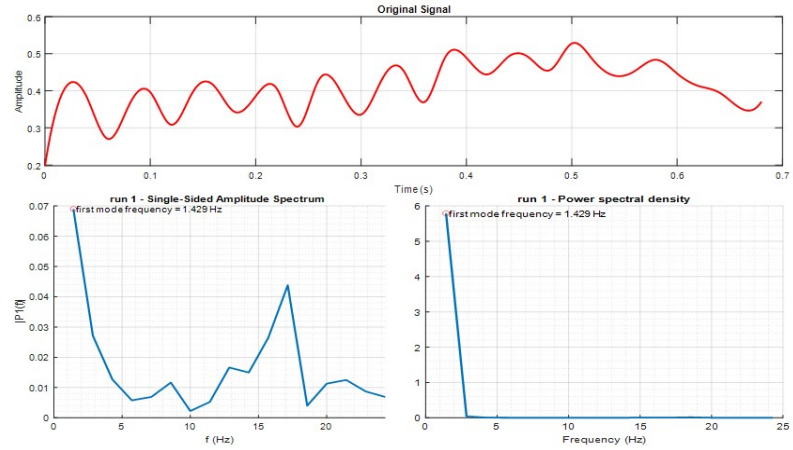

Figure 4.32: Single Sided Amplitude Spectrum and PSD for wing with VGs

The dominant peak value for wing and wing with VGs are 1.250 Hz and 1.429 Hz respectively. Hence, the obtained Strouhal number for wing and wing with VGs are 0.1381 and 0.1571 respectively.

4.3.3. Effectiveness of VGs with comparison of wing using Strouhal number

The effectiveness of vortex generator is measured in terms of Strouhal number.

Table 4.4: Strouhal Numbers comparison for wing and wing with VGs

Case	Strouhal Frequency (Hz)	Strouhal Number
Wing	1.250	0.1381
Wing with VGs	1.429	0.1571

On the basis of specific wake formation, the wake formation can be divided into four regions which are tabulated in table 4.5.

Table 4.5: Wake Formation Characteristics [31]

Case	Characteristics	Strouhal Number Range
A	Drag-type, momentum deficit	$St < 0.14$
B	Neutral-type	$0.14 < St < 0.15$
C	Thrust-type, momentum surplus	$0.15 < St < 0.32$
D	Thrust/lift-type	$St > 0.32$

The experimental results revealed a notable difference in the Strouhal numbers between the wing without VGs (0.1381) and the wing with VGs (0.1571). According to the predefined Strouhal number ranges [31], the former falls within Case A, indicating a drag-type wake with a momentum deficit, while the latter falls within Case C, indicative of a thrust-type wake with a momentum surplus.
The shear layer became more concentrated, indicating a decrease in diffusion. This concentration enabled the shear layer, situated on the opposite side of the developing vortex, to penetrate more easily into the growing vortex . Additionally, the distance between the two shear layers decreased. Consequently, these two effects led to a sudden increase in the Strouhal number.

This confirms that the addition of VGs alters the wake formation from drag-type to thrust-type, resulting in improved aerodynamic efficiency and enhanced momentum transfer.

4.4. Possible Error Sources

1. The uneven illumination of two lasers used, which were of 5 mW and 100 mW may have caused uneven brightness of tracer particles throughout the experimental video when the plane is not matched.
2. The inability of camera to capture higher amount of frame rates than 120 fps limited the result obtained from frequency plot.

4.5. Work Completed

1. Development of a fully-functional linear actuation mechanism.

2. Selection of uniform diameter seeding particle and high power laser for PIV.
3. Numerical simulation and grid independence study of flow past a circular cylinder.
4. Selection of airfoil, vortex generator and wing parameters along with numerical simulation and grid independence study of airfoil.
5. Setup characterization through Strouhal number comparison between simulation and experimental results, for flow past a circular cylinder.
6. Experimental analysis of velocity field and vortices across the wing and wing with VGs and validation of the result using Strouhal number.

4.6. Limitations

1. The planar PIV study does not incorporate three dimensional calculation and analysis for flow past the wing as compared to the stereoscopic PIV.
2. The resolution of camera were not enough to capture the boundary layer separation for the VGs.
3. Light deficiency and particle blurring may appear and contribute to increasing the loss of correlation in some region , introducing limits to the achievable spatial resolution of the velocity field when a continuous laser is used for PIV experiment [32].

4.7. Problems faced

The complications that arised during the experimental and numerical study can be listed as below:

1. The inability of Sony alpha 6000 camera to capture required amount of sampling frame rate for characterization of PIV setup.
2. The available power of laser was less than 5mW while the calculation for minimum threshold value required for the experiment was 15mW.
3. The inability of the existing gantry system to limit the motion to 1D and the vibration induced motion of the gantry, required the complete modification of the actuation mechanism.

4.8. Budget Analysis

The budget estimation for the overall project from start to finish is shown in the table **??**.

Table 4.6: Cost Estimation

S.N.	**Particulars**	**Rate**	**Quantity**	**Cost**(Rs)
1	100 mW point laser	1300/-	1	1300/-
2	L298N Stepper motor driver	350/-	1	350/-
3	Nema 23 Stepper Motor	3220/-	1	3220/-
4	TB6600 Stepper motor driver	1100/-	1	1100/-
5	Arduino Uno (Micro-controller)	1500/-	1	1500/-
6	24V DC adapter	500/-	1	500/-
7	3 push buttons and one mini breadboard	-	-	85/-
8	Rectangular hollow Rod	1750/-	1	1750/-
9	8mm diameter 1 m long threaded rod	950/-	1	950/-
10	6mm diameter 1 m long threaded rod	650/-	1	650/-
11	Nuts, bolts, screws and washers	-	-	600/-
12	6 mm bore ball bearings	100/-	10	1000/-
13	Pulley 2GT 8mm long	160/-	1	160/-
14	Paint	350/-	1	350/-
15	Man hour	-	-	300/-
16	Miscellaneous	-	-	10000/-
Total				23815/-

4.9. Work Schedule (Gantt Chart)

The work schedule for the project is shown in the Gantt chart (Figure **??**.

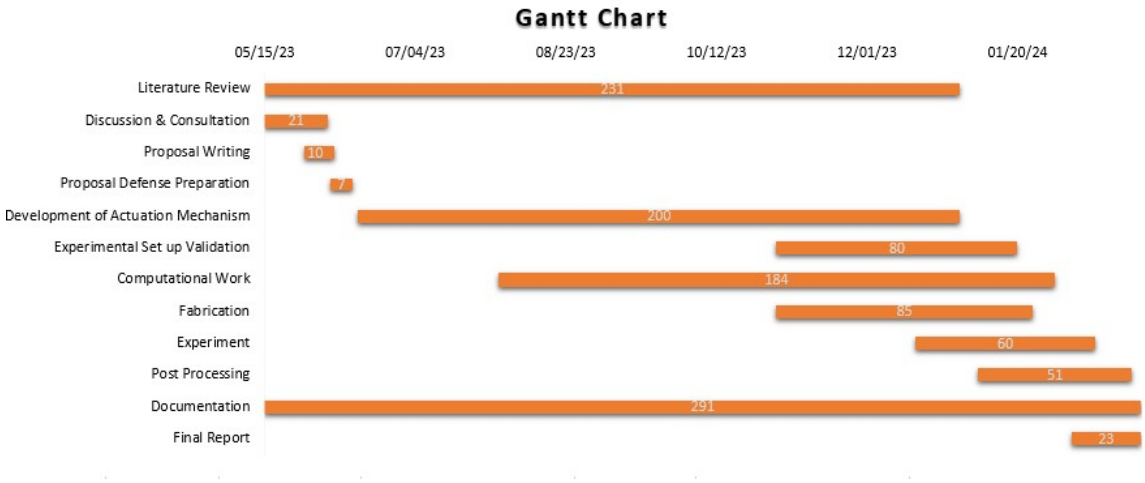

Figure 4.33: Gantt Chart

Table 4.7: Project Timeline

Task Name	**Duration**	**Start**	**Finish**
Literature Review	231	05/15/23	01/01/24
Discussion & Consultation	21	05/15/23	06/05/23
Proposal Writing	10	05/28/23	06/07/23
Proposal Defense Preparation	7	06/06/23	06/13/23
Development of Actuation Mechanism	200	06/15/23	01/01/24
Experimental Set up Validation	80	11/01/23	01/20/24
Computational Work	184	08/01/23	02/01/24
Fabrication	85	11/01/23	01/25/24
Experiment	60	12/17/23	02/15/24
Post Processing	51	01/07/24	02/27/24
Documentation	291	05/15/23	03/01/24
Final Report	23	02/07/24	03/01/24

CHAPTER FIVE: CONCLUSION AND FUTURE ENHANCEMENT

5.1. Conclusion

A functional linear actuation mechanism was developed for the planar PIV experimental setup to perform experiment in low Reynold's number. The gantry system was modified to improve the accuracy of PIV measurements by limiting the motion to one degree of freedom and reducing discontinuous motion.

Initially, the analysis of circular cylinder was done on a small prototype tank of dimension $1220\,\text{mm} \times 100\,\text{mm} \times 150\,\text{mm}$ with the use of glass particles incorporating huge variation in diameter which produced erroneous results during image processing for vector plot and velocity plot. The PIV technique involves use of uniform seeding particles and high power laser having nearly gaussian intensity distribution for accurate analysis and the erroneous results were due to the use of non-uniform glass particles, low power laser having irregular intensity distribution.

The selection of seeding particle for water was done on the basis of stokes number criterion and the laser was selected for optimum power level greater than 15mW. Furthermore, the numerical simulation and analysis was done for the flow past a circular cylinder and the strohaul number and strohaul frequency was calculated. The CAD model of the 25mm diameter circular cylinder was then exported in Halotbox and the 3D model of the cylinder was resin printed.

The stall angle of attack and optimum location of VG on the upper surface of the wing from the leading edge measured along the chord were determined by performing a preliminary CFD simulation of the baseline wing and wing with VG.

The visualization of vortex behind the cylinder was first captured in small water channel and the velocity and vorticity contours flow were investigated. After completing multiple rounds of experiments in small channel, we moved to the large tank. The experimental setup characterization were performed by analyzing three sets of different experimental data for vorticity which gave us an relative error range of nearly 3 % around value.

Critically assessing the setup characterization, the experimental investigation for wing and wing with VGs were performed at 15 degree angle of attack. The flow shedding characteristics were studied in terms of strouhal numbers which helped to investigate the effectiveness of vortex generator.

In a nutshell, the linear actuation mechanism, experimental setup characterization and experimental investigation of vortex shedding characteristics for wing and wing with VGs had been studied.

5.2. Scope for future enhancement

1. Development of a fully functional stereoscopic PIV setup for 3D flow analysis across various objects.
2. Integrating a mechanism that alters the Angle of Attack (AOA) of the test specimen.
3. Investigating flow over the cylinder at different velocities within low Reynolds number range.
4. Implement machine learning algorithms for data analysis, pattern recognition, and optimization of flow parameters based on experimental and numerical results.
5. Include thermal considerations in the study to analyze the impact of temperature variations on the flow field around the cylinder and wing.
6. Use of high power pulsed laser for experimental validation and analysis.

References

[1] U. F. Gámiz, "Fluid dynamic characterization of vortex generators and two-dimensional turbulent wakes," *POLYTECHNIC UNIVERSITY OF CATALONIA, CATALONIA,[Online]. Available: www. tesisenred. net/bitstream/handle/10803/13459/tufg1de1. pdf [Accessed 27 June 2015]*, 2013.

[2] H. Shim, Y.-H. Jo, K. Chang, K.-J. Kwon, and S.-O. Park, "Wake characteristics of vane-type vortex generators in a flat plate laminar boundary layer," *International Journal of Aeronautical and Space Sciences*, vol. 16, no. 3, pp. 325–338, 2015.

[3] R. King, "A review of vortex shedding research and its application," *Ocean Engineering*, vol. 4, no. 3, pp. 141–171, 1977. [Online]. Available: https://www.sciencedirect.com/science/article/pii/0029801877900026

[4] V. Oruç, H. Akilli, and B. Sahin, "Piv measurements on the passive control of flow past a circular cylinder," *Experimental Thermal and Fluid Science*, vol. 70, pp. 283–291, 2016.

[5] Y. Liu, B. Cheng, S. P. Sane, and X. Deng, "Aerodynamics of dynamic wing flexion in translating wings," *Experiments in Fluids*, vol. 56, pp. 1–15, 2015.

[6] O. A. Elsayed, W. Asrar, A. A. Omar, and K. Kwon, "Evolution of naca23012 wake vortices structure using piv," *Journal of Aerospace Engineering*, vol. 25, no. 1, pp. 10–20, 2012.

[7] D. Greenblatt, "Management of vortices trailing flapped wings via separation control," in *43rd AIAA Aerospace Sciences Meeting and Exhibit*, 2005, p. 61.

[8] C. M. Velte, V. L. Okulov, and I. V. Naumov, "Regimes of flow past a vortex generator," *Technical Physics Letters*, vol. 38, pp. 379–382, 2012.

[9] J. I. Yanagihara and K. Torii, "Heat transfer augmentation by longitudinal vortices rows," in *Experimental Heat Transfer, Fluid Mechanics and Thermodynamics 1993*. Elsevier, 1993, pp. 560–567.

[10] X. Li, K. Yang, and X. Wang, "Experimental and numerical analysis of the effect of vortex generator height on vortex characteristics and airfoil aerodynamic performance," *Energies*, vol. 12, no. 5, p. 959, 2019.

[11] O. M. Fouatih, M. Medale, O. Imine, and B. Imine, "Design optimization of the aerodynamic passive flow control on naca 4415 airfoil using vortex generators," *European Journal of Mechanics-B/Fluids*, vol. 56, pp. 82–96, 2016.

[12] J. C. Lin, "Review of research on low-profile vortex generators to control boundary-layer separation," *Progress in aerospace sciences*, vol. 38, no. 4-5, pp. 389–420, 2002.

[13] T. Wilson, "Investigation of low-profile vortex generators via computational methods," Ph.D. dissertation, Oklahoma State University, 2019.

[14] M. Manolesos, L. Chng, N. Kaufmann, P. Ouro, D. Ntouras, and G. Papadakis, "Using vortex generators for flow separation control on tidal turbine profiles and blades," *Renewable Energy*, vol. 205, pp. 1025–1039, 2023.

[15] B. M. Sumer *et al.*, *Hydrodynamics around cylindrical strucures*. World scientific, 2006, vol. 26.

[16] R. D. Blevins, *Flow-induced vibration*. Krieger Pub. Co., 1994.

[17] G. West and C. Apelt, "The effects of tunnel blockage and aspect ratio on the mean flow past a circular cylinder with reynolds numbers between 104 and 105," *Journal of Fluid mechanics*, vol. 114, pp. 361–377, 1982.

[18] O. López Calle, "Preliminary study of the effects of vortex generators in ultralight aircraft," B.S. thesis, Universitat Politècnica de Catalunya, 2015.

[19] X.-k. Li, W. Liu, T.-j. Zhang, P.-m. Wang, and X.-d. Wang, "Analysis of the effect of vortex generator spacing on boundary layer flow separation control," *Applied Sciences*, vol. 9, no. 24, p. 5495, 2019.

[20] M. Raffel, C. E. Willert, F. Scarano, C. J. Kähler, S. T. Wereley, J. Kompenhans, M. Raffel, C. E. Willert, F. Scarano, C. J. Kähler *et al.*, "Techniques for 3d-piv," *Particle Image Velocimetry: A Practical Guide*, pp. 309–365, 2018.

[21] A. Schröder and C. E. Willert, "Particle image velocimetry: new developments and recent applications," 2008.

[22] A. Melling, "Tracer particles and seeding for particle image velocimetry," *Measurement science and technology*, vol. 8, no. 12, p. 1406, 1997.

[23] U. Shavit, R. J. Lowe, and J. V. Steinbuck, "Intensity capping: a simple method to improve cross-correlation piv results," *Experiments in Fluids*, vol. 42, pp. 225–240, 2007.

[24] H. Huang, D. Dabiri, and M. Gharib, "On errors of digital particle image velocimetry," *Measurement Science and Technology*, vol. 8, no. 12, p. 1427, 1997.

[25] E. Stamhuis and W. Thielicke, "Pivlab–towards user-friendly, affordable and accurate digital particle image velocimetry in matlab," *Journal of open research software*, vol. 2, no. 1, p. 30, 2014.

[26] J. Soria, "An investigation of the near wake of a circular cylinder using a video-based digital cross-correlation particle image velocimetry technique," *Experimental Thermal and Fluid Science*, vol. 12, no. 2, pp. 221–233, 1996.

[27] W. Thielicke and R. Sonntag, "Particle image velocimetry for matlab: Accuracy and enhanced algorithms in pivlab," *Journal of Open Research Software*, vol. 9, no. 1, 2021.

[28] M. T. Asyikin, "Cfd simulation of vortex induced vibration of a cylindrical structure," Master's thesis, Institutt for bygg, anlegg og transport, 2012.

[29] A. Prasad and C. H. Williamson, "The instability of the shear layer separating from a bluff body," *Journal of fluid mechanics*, vol. 333, pp. 375–402, 1997.

[30] E. Achenbach, "Experiments on the flow past spheres at very high reynolds numbers," *Journal of fluid mechanics*, vol. 54, no. 3, pp. 565–575, 1972.

[31] W. Ren, H. Hu, H. Liu, and J. C. Wu, "An experimental investigation on the asymmetric wake formation of an oscillating airfoil," in *Proceedings of the 51st AIAA Aerospace Sciences Meeting including the New Horizons Forum and Aerospace Exposition, Paper*, vol. 794. Citeseer, 2013.

[32] P. Lopez-Gavilan and A. Barrero-Gil, "On the limits of particle image velocimetry with continuous wave lasers," *Experimental Thermal and Fluid Science*, vol. 144, p. 110873, 2023.

[33] T. Liu and D. M. Salazar, "Openopticalflow_piv: an open source program integrating optical flow method with cross-correlation method for particle image velocimetry," *Journal of Open Research Software*, vol. 9, no. 1, 2021.

APPENDIX

A.1. Gantry System

A.1.1. CAD model

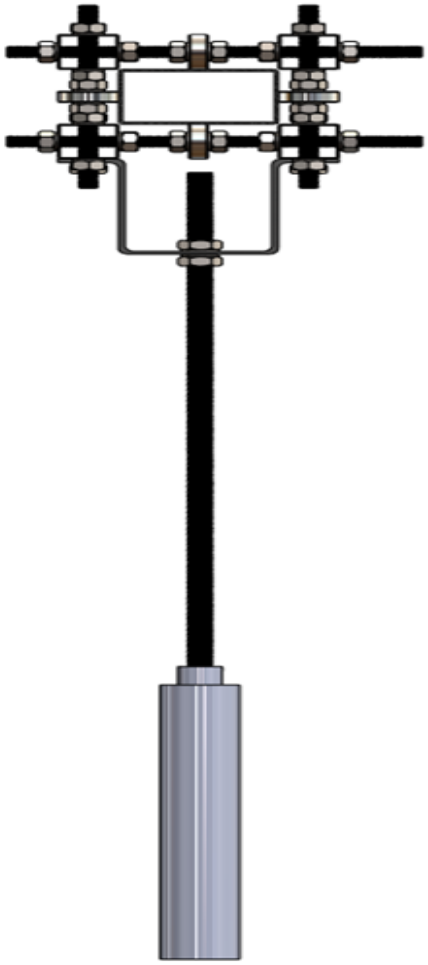

Figure A.1: Gantry Assembly Front View

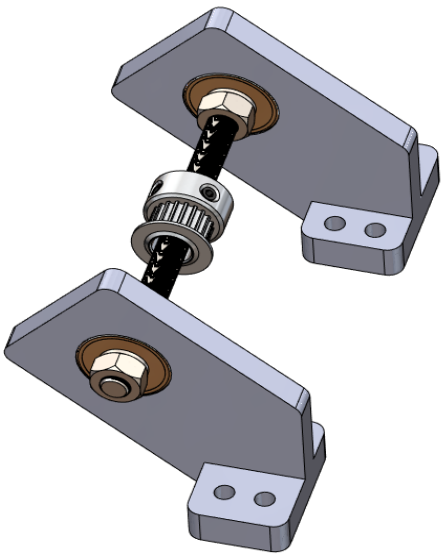

Figure A.2: Gantry Driven end

A.1.2. Fabricated parts

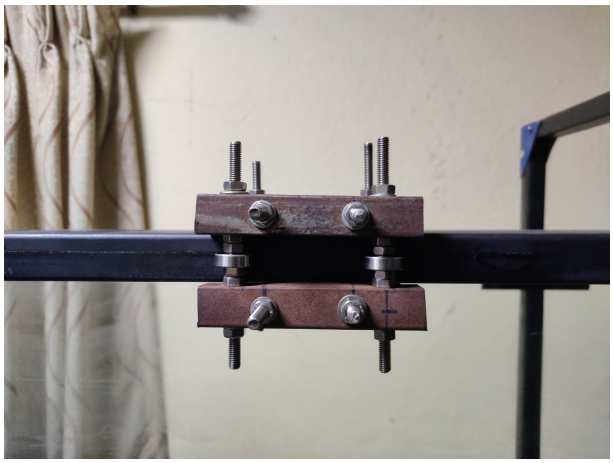

(a) Gantry roller side view

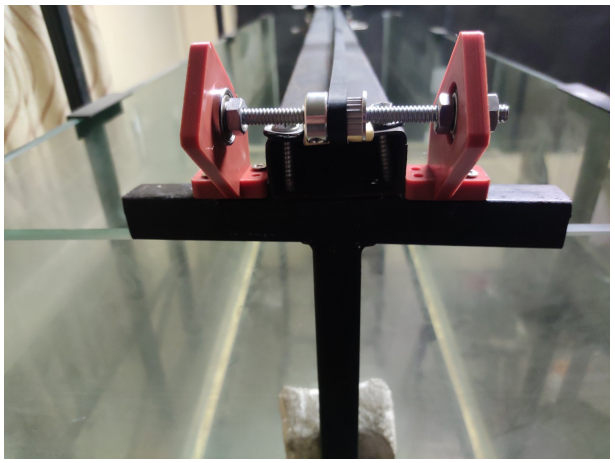

(b) Gantry driven end

(c) U shaped connector

Figure A.3: Gantry System: Fabricated Parts

A.2. Codes

A.2.1. Arduino Code to control Stepper motor

```
#define SW1 2
#define SW2 3
#define SW3 4
#define PUL 6
#define DIR 7
#define ENA 8 // HIGH disables motor power

#define CW 1
#define CCW 0

// indicates motor is on
// this is built in LED on DP13.
#define motorOn 13

// sets how many pulses for 360 degrees
//#define rot360 100

// the microstepping settings used in the TB6600 driver
int ms = 800; // in steps/rev

// HIGH on PUL will keep motor locked in position
// note motor will get hot after some time.


// this sets the motor speed
int pulseDelay = 130; // in uSec.

void setup() {
  Serial.begin(9600);
  Serial.println("Starting␣Stepper");
  // DP13 LED
  pinMode(motorOn, OUTPUT);
  digitalWrite(motorOn, LOW);
```

```
  pinMode(SW1, INPUT_PULLUP);
  pinMode(SW2, INPUT_PULLUP);
  pinMode(SW3, INPUT_PULLUP);
  pinMode(DIR, OUTPUT);
  digitalWrite(DIR, LOW);
  pinMode(PUL, OUTPUT);
  digitalWrite(PUL, LOW);
  pinMode(ENA, OUTPUT);
  digitalWrite(ENA, HIGH);
}

void printSpeed(int pulseDelay) {
  float speed_RPS = 1000000 / (pulseDelay * ms);
  Serial.print("Speed (RPS): ");
  Serial.println(speed_RPS);
}

void loop() {

while (digitalRead(SW1) == 0){
  // manual CW when pushed
  if (digitalRead(SW2) == 0){
  while (digitalRead(SW2) == 0 && digitalRead(SW1) == 0) {
    digitalWrite(motorOn, HIGH); // motor LED On
    digitalWrite(ENA, LOW); // enable motor power
    digitalWrite(DIR, CW);
    digitalWrite(PUL, 1);
    delayMicroseconds(pulseDelay);
    digitalWrite(PUL, 0);
    delayMicroseconds(pulseDelay);
  } // end while
  }
  else{
  // manual CCW when pushed
  while (digitalRead(SW3) == 0 && digitalRead(SW1) == 0) {
    digitalWrite(motorOn, HIGH); // motor LED On
    digitalWrite(ENA, LOW); // enable motor power
    digitalWrite(DIR, CCW);
```

```
    digitalWrite(PUL, 1);
    delayMicroseconds(pulseDelay);
    digitalWrite(PUL, 0);
    delayMicroseconds(pulseDelay);
  } // end while
  }
}

  if (digitalRead(SW2) && digitalRead(SW3)) digitalWrite(
     motorOn, LOW);

  if(digitalRead(SW1) == 1)
  {
    digitalWrite(PUL, LOW);
    digitalWrite(ENA, HIGH);
  }

printSpeed(pulseDelay);
} // end loop
```

A.2.2. Matlab Codes

1. **Video to .tif (video frame extraction)**

```
    % Create a GUI to select a video file
[filename, pathname] = uigetfile({'*.mp4;*.avi;*.mov;*.
   mkv;*.flv', 'Video Files (*.mp4, *.avi, *.mov, *.mkv,
   *.flv)'}, 'Select a Video File');

% Check if the user clicked on Cancel
if isequal(filename, 0) || isequal(pathname, 0)
    disp('User canceled the operation.');
    return;
end

% Construct the full file path
videoFilePath = fullfile(pathname, filename);

% Create a VideoReader object
```

```
videoObj = VideoReader(videoFilePath);

% Create an output folder for the TIFF images
outputFolder = 'output_tiff_images';
if ~exist(outputFolder, 'dir')
    mkdir(outputFolder);
end

% Loop through each frame and save it as a TIFF image
while hasFrame(videoObj)
    frame = readFrame(videoObj);
    currentFrame = videoObj.CurrentTime * videoObj.
       FrameRate;

    % Save the frame as a TIFF image
    outputFileName = sprintf('frame_%04d.tif', round(
       currentFrame));
    imwrite(frame, fullfile(outputFolder, outputFileName)
       , 'tif');
end

disp('Conversion completed.');
```

2. **Uniform Velocity Masking**

```
imageFolder = uigetdir('Select a folder containing images
   '); %% Helps to select a directory

if imageFolder == 0
    error('Operation cancelled by the user.');
end

%%Helps to select a file
[imageFile, imageFolder] = uigetfile(fullfile(imageFolder
   , '*.*'), 'Select an image file', 'MultiSelect', 'on')
   ;

if isequal(imageFile, 0)
```

```
    error('Operation cancelled by the user.');
end

if ~iscell(imageFile)
    imageFile = {imageFile};
end
%%% Output folder
outputFolder = uigetdir('Select a folder to save frames
   as .tif files');

if outputFolder == 0
    error('Operation cancelled by the user.');
end
%%%%%%%%%%%%%%%%%%%%%%%%%%%%%%%%%%%%%%%%%%%%%%%%

%//Frame rate
prompt = 'Enter the frame rate: ';
frameRate = input(prompt);

prompt = 'Enter the velocity in meters per second: ';
%vel=0.045  for Feb 8 M74 Circular cylinder;
vel = input(prompt);
velocity =vel*(frameRate/60);

for i = 1:length(imageFile)
    currentImagePath = fullfile(imageFolder, imageFile{i
       });
    currentImage = imread(currentImagePath);

    % Display the image
    figure;
    imshow(currentImage);
    title(['Draw a region of interest (ROI) for Image ',
       num2str(i)]);

    % Allow to draw an ROI
    roi = roipoly;
```

```
    binaryMask = roi;

    prompt = 'Enter the number of frames to display: ';
    numFrames = input(prompt);

    % Calculate shift speed in pixels per frame
    % pixel value and real distance as inputs from PIVLAB
        or any Image processing software


%pixelValue = input('Enter the pixel value corresponding
   to a known real distance: ');
%pixelValue = 701.31;
  %pixelValue =436.91;%For Feb 8 M74 Circular cylinder;
        pixelValue =210.13;%For Feb 3792 M74 Circular
           cylinder;



%realDistanceMM = input('Enter the known real distance in
    millimeters: ');
realDistanceMM =25 ;


ppmm = pixelValue / realDistanceMM; % Calculate Pixels
   per Millimeter (PPMM)
pixelsPerMeter = ppmm * 1000; % Convert PPMM to Pixels
   per Meter

    shiftSpeed = velocity * pixelsPerMeter / frameRate; %
       %main

    prompt = 'Enter a file name for the video (without
       extension): ';
    videoFileName = input(prompt, 's');  % 's' specifies
       as a string (for my information)
```

```
    if isempty(videoFileName)
        error('Operation cancelled by the user.');
    end

    for frame = 1:numFrames
        shiftDistance = round(frame * shiftSpeed); %%
            round off the value
        shiftedMask = circshift(binaryMask, [0,
            shiftDistance]); %% shifts circularly
        binaryImageWithWhiteROI = zeros(size(currentImage
            , 1), size(currentImage, 2));
        binaryImageWithWhiteROI(shiftedMask) = 1;
        whiteInsideROI = uint8(repmat(
            binaryImageWithWhiteROI, [1, 1, size(
            currentImage, 3)]) * 255);
        figure(2);
        imshow(whiteInsideROI, 'InitialMagnification', '
            fit');
        title(['Original Image with White Inside ROI -
            Frame ', num2str(frame)]);

        % Save the frame as a .tif file
        frameFileName = fullfile(outputFolder, [
            videoFileName, '_frame_', num2str(frame), '.
            tif']);
        imwrite(whiteInsideROI, frameFileName);

        pause(0.1);
    end
end
```

3. **Hybrid Algorithm for PIV (References from PIVLAB and Open Optical Flow Algorithm) [33]**

```
   % Prompt the user to select a folder
selectedFolder = uigetdir('Select a folder');

% Check if the user clicked Cancel
if isequal(selectedFolder, 0)
```

```
    disp('User canceled folder selection. Exiting...');
    return;
end

% Prompt the user to select the first image file within
   the selected folder
[file1, folder] = uigetfile(fullfile(selectedFolder, '*.
   tif'), 'Select the First Image File');

% Check if the user clicked Cancel
if isequal(file1, 0)
    disp('User canceled first image file selection.
       Exiting...');
    return;
end

% Prompt the user to select the second image file within
   the selected folder
[file2, folder] = uigetfile(fullfile(selectedFolder, '*.
   tif'), 'Select the Second Image File');

% Check if the user clicked Cancel
if isequal(file2, 0)
    disp('User canceled second image file selection.
       Exiting...');
    return;
end

% Construct the full paths to the selected image files
selectedImageFile1 = fullfile(folder, file1);
selectedImageFile2 = fullfile(folder, file2);

% Display the selected folder and image files
disp(['Selected Folder: ', selectedFolder]);
disp(['Selected Image File 1: ', selectedImageFile1]);
disp(['Selected Image File 2: ', selectedImageFile2]);

% Load the selected image files
```

```
Im1 = imread(selectedImageFile1);
Im2 = imread(selectedImageFile2);

%% Selete region of interest, "0" for processing the
   whole image, "1" for processing a selected region
index_region=0;

Im1=double(Im1);
Im2=double(Im2);

if (index_region == 1)
    imagesc(uint8(Im1));
    colormap(gray);
    axis image;

    xy=ginput(2);
    x1=floor(min(xy(:,1)));
    x2=floor(max(xy(:,1)));
    y1=floor(min(xy(:,2)));
    y2=floor(max(xy(:,2)));
    I1=double(Im1(y1:y2,x1:x2));
    I2=double(Im2(y1:y2,x1:x2));
elseif (index_region == 0)
    I1=Im1;
    I2=Im2;
end

I1_original=I1;
I2_original=I2;


%% Set the Parameters for Optical Flow Computation

% Set the lagrange multipleirs in optical computation
lambda_1=17;  % the Horn_schunck estimator for initial
   field
lambda_2=2000; % the Liu-Shen estimator for refined
   estimation
```

```
%% Number of iterations in the coarse-to-fine iterative
   process from
%% initial estimation, "1" means 1 iteration
no_iteration=1; % fixed

%% Initial coarse field estimation in the coarse-to-fine
   iterative process,
%% scale_im is a scale factor for down-sizing of images
scale_im=0.3;
%% For Image Pre-Processing

%% For local illumination intensity adjustment, To bypass
    it, set size_average = 0
size_average=0; % in pixels

%% Gausian filter size for removing random noise in
   images
size_filter=6; % in pixels

%% correcting the global and local intensity change in
   images
[m1,n1]=size(I1);
window_shifting=[1;n1;1;m1]; % [x1,x2,y1,y2] deines a
   rectangular window for global intensity correction
[I1,I2]=correction_illumination(I1,I2,window_shifting,
   size_average);


%% cleaning the left and upper edges since some data near
    the edges are corrupted due to interpolation
edge_width=1; % in pixels


%% pre-processing for reducing random noise,
%% and downsampling images if displacements are large
[I1,I2] = pre_processing_a(I1,I2,scale_im,size_filter);
```

```
I_region1=I1;
I_region2=I2;


%% initial correlation calculation for a coarse-grained
   velocity field (ux0,uy0)
% ux is the velocity (pixels/unit time) in the image x-
   coordinate (from the left-up corner to right)
% uy is the velocity (pixels/unit time) in the image y-
   coordinate (from the left-up corner to bottom)


%% run FFT cross-correlation algorithm
Im1=I1;
Im2=I2;

pivPar.iaSizeX = [64 16 8];     % size of interrogation
   area in X
pivPar.iaStepX = [32 8 4];       % grid spacing of
   velocity vectors in X

pivPar.ccMethod = 'fft';

[pivData1] = pivAnalyzeImagePair(Im1,Im2,pivPar);

ux0=pivData1.U;
uy0=pivData1.V;


%% re-size the initial velocity field (u0, v0)
[n0,m0]=size(ux0);
[n1,m1]=size(Im1);

scale=round((n1*m1/(n0*m0))^0.5);

ux0=imresize(ux0,scale);
uy0=imresize(uy0,scale);
```

```
%% generate the shifted image from Im1 based on the
   initial coarse-grained velocity field (ux0, uy0),
%% and then calculate velocity difference for iterative
   correction


%% estimate the displacement vector and make correction
   in iterations

ux=ux0;
uy=uy0;

k=1;
while k<=no_iteration
   [Im1_shift,uxI,uyI]=shift_image_fun_refine_1(ux,uy,Im1
      ,Im2);

    I1=double(Im1_shift);
    I2=double(Im2);

    % calculation of correction of the optical flow
    [dux,duy,vor,dux_horn,duy_horn,error2]=
       OpticalFlowPhysics_fun(I1,I2,lambda_1,lambda_2);

    % refined optical flow
    ux_corr=uxI+dux;
    uy_corr=uyI+duy;


    k=k+1;
end

%% refined velocity field
ux = ux_corr;     %%%%%
uy = uy_corr;     %%%%%
```

```
%% clean up the edges
ux(:,1:edge_width)=ux(:,(edge_width+1):(2*edge_width));
uy(:,1:edge_width)=uy(:,(edge_width+1):(2*edge_width));

ux(1:edge_width,:)=ux((edge_width+1):(2*edge_width),:);
uy(1:edge_width,:)=uy((edge_width+1):(2*edge_width),:);



%% show the images and processed results
%% plot the images, velocity vector, and streamlines in
   the initail and
%% refined estimations
% plots_set_1;

%% plot the fields of velocity magnitude, vorticity and
   the second invariant Q
 plots_set_2;
```

4. **FFT for Post processing of Data**

```
   % Load data from Excel file
filename = 'fft.xlsx';  % Provide the name of your Excel
   file
sheet =21;  % Specify the sheet number from which you
   want to read data

% Read data from the second sheet
data = xlsread(filename, sheet);

% Assuming the second column contains the signal data
signal = data(:,2); % Extract signal column

% Frame rate (samples per second)
frame_rate = 120;  % Modify this value according to your
   frame rate

% Calculate time values based on frame rate
```

```
num_samples = length(signal);
time = (0:num_samples-1) / frame_rate;

% Smooth the time curve using spline interpolation
time_smooth = linspace(min(time), max(time), 10*
   num_samples);  % Increase the number of points for
   smoothness

% Perform Fast Fourier Transform (FFT)
Fs = frame_rate; % Sampling frequency
N = length(signal); % Number of samples
Y = fft(signal); % Compute FFT
f = Fs*(0:(N/2))/N; % Frequency vector


% Calculate Power Spectral Density (PSD)
P = abs(Y(1:N/2+1)).^2/N; % One-sided PSD
P(2:end-1) = 2*P(2:end-1); % Adjust for two-sided
   spectrum

% Plot original signal
figure;
subplot(2,1,1);
plot(time_smooth, spline(time, signal, time_smooth), 'r',
   'LineWidth',2);
xlabel('Time (s)');
ylabel('Amplitude');
title('Original Signal');
grid on;

% Plot PSD data
subplot(2,1,2);
plot(f, P);
xlabel('Frequency (Hz)');
ylabel('Power/Frequency');
title('Power Spectral Density');
grid on;
```

```
% % Compute the periodogram
% [Pxx_periodogram, f_periodogram] = periodogram(signal,
   [], N, Fs);
%
% % Plot the periodogram
% subplot(2,1,2);
% plot(f_periodogram, 10*log10(Pxx_periodogram));  % Plot
    in dB scale
% xlabel('Frequency (Hz)');
% ylabel('Power/Frequency (dB/Hz)');
% title('Periodogram');
% grid on;


% arbitrary_fft(FFTS19, 120);
arbitrary_fft(signal, 120,3);

% Plot original signal
subplot(1, 2, 1);
plot(time_smooth, spline(time, signal, time_smooth), 'r')
   ;
xlabel('Time (s)');
ylabel('Amplitude');
title('Original Signal');
grid on;

% % Call arbitrary_fft function and plot its result
% subplot(1, 2, 2);
% arbitrary_fft(signal, 50, 1); % Assuming index is 1




%
   %%%%%%%%%%%%%%%%%%%%%%%%%%%%%%%%%%%%%%%%%%%%%%%%%%%%%%%%%%%%%%
```

5. **Arbitrary FFT**

```
% arbitrary FFT

function []=arbitrary_fft(sample_array,sample_freq,index)
% sample_array=dY_lex; sample_freq=2000; index=944;
   string2='';

L = length(sample_array);    % Length of oscillation
   signal
Fs = sample_freq;        % sampling frequency
Y = fft(sample_array,L);

P2 = abs(Y/L);
P1 = P2(1:L/2+1);
P1(2:end-1) = 2*P1(2:end-1);
f = Fs*(0:(L/2))/L;
figure(101)
hold on
plot(f(2:end),P1(2:end),'LineWidth',2)
title(['run ' num2str(index) ' - Single-Sided Amplitude
   Spectrum'])
xlabel('f (Hz)')
ylabel('|P1(f)|')
f=f(2:end);
P1_max=max(P1(2:end));
f_m1=f(P1(2:end)==P1_max);
plot(f_m1,P1_max,'ro')
text(f_m1,P1_max,strcat( ...
    [' first mode frequency = ' num2str(round((f_m1),3,'
       decimals')) ' Hz']))
hold off
grid on
grid minor
  xlim([0 35])
% xlim([0 max(f)])

clear f
```

```
% cd ../afosr_tusq_apr_may/figures
% print('-dpdf',['run_' num2str(index) '
   _sch_model_amplitude_sepectrum.pdf'])
% cd ../../sch_plate_deform


Pyy = Y.*conj(Y)/L;
f = Fs/L*(1:L/2);
figure(102)
hold on
plot(f(1:end),Pyy(1:end/2),'LineWidth',2)
title(['run ' num2str(index) ' - Power spectral density'
   ])
xlabel('Frequency (Hz)')
Pyy_max=max(Pyy(1:end/2));
f=f(1:end);
plot(f(Pyy(1:end/2)==Pyy_max),Pyy_max,'ro') %
f_m1=f(Pyy(1:end/2)==Pyy_max);
text(f(Pyy(1:end/2)==Pyy_max),Pyy_max,strcat(...
    [' first mode frequency = ' num2str(round((f_m1),3,'
       decimals')) ' Hz']))
hold off
grid on
grid minor
 xlim([0 35])
% xlim([0 max(f)])

clear f

% cd ../afosr_tusq_apr_may/figures
% print('-dpdf',['run_' num2str(index) '
   _sch_model_power_spectral_density.pdf'])
% cd ../../sch_plate_deform
```

6. **Post processing data code**

```
% Track TSR1018 ramp deform images
clc
clear
```

```
close all

% dataDir = 'C:\Users\sudip\Documents\MATLAB\exp_post\
   wing_def\PIV';
dataDir = 'D:\8th Semester\Project\PIV\gantry system\
   Openpiv\Medias for analysis\im_post\piv';

run_time_read = 1;    % reading all images


%% Run info
run     = 1;          % run number
load    = 0;          % applied load, as in file name
fps     = 120;        % Sampling rate

% Define run paramters in a lot, if available
i_imo = 1; n_im = 175; cscale = 250;
time=0:1/fps:n_im/fps-1/fps;
% number of tracking profile-xpoints
n_xp    = 3;

% Geom
b       = 400;        % wing semi span

%% Data info

% wd = fullfile(dataDir, ['/daq_load' num2str(load) '
   kg_run' num2str(run)]);
wd=dataDir;
% data_suffix = '_000';    % Time-indexing of images

%% Read sample image

filename=[wd '/frame_' num2str(i_imo,'%04.0f') '.tif'];
[Im,map]=imread(filename);
im_info = imfinfo(filename);
width = getfield(imfinfo(filename),'Width');
height = getfield(imfinfo(filename),'Height');
```

```
imagesc(Im)

%% pixel values and image crop frame

%ppx and ppy with manual calculation
ppmm = 4.6; %pixels per mm
% define boundary (manual assignent)
%  h1 = 200; h2= 950; xstart = 450; xend = 1400;
 h1 = 1; h2= height; xstart = 1; xend = width;

%% Read images, with cropping
if run_time_read

    for n=1:n_im   % read ALL images for database
        [data_map] = read_tif(h1,h2,xstart,xend,wd,n);
        data_maps.(genvarname(['im_' num2str(n)]))=
           data_map;
    end
else
    load(['wing_data/run' num2str(run) '_sch_maps.mat']);
end


%% Sample image
Ims = data_maps.im_175;
f1=figure('Name','Display sample Schlieren image','
   NumberTitle','on');
imagesc(Ims,[0 cscale]);
set(gca,'DataAspectRatio',[1 1 1])
colorbar

%% animate
for j=1:3
    for i=1:175
        imm=data_maps.(genvarname(['im_' num2str(i)]));
        imagesc(imm,[0 cscale]);
        colorbar
```

```
        pause(0.005)
        pt_data(i,j)=imm(height/2,width/2+(j-1)*50);
    end
end

clear imm


%% FFT

interval = 2^6; % window 2e-7 for 2kHz signal
overlap = 2^5;  % overlap  2e-6 for 2kHz signal
nfft = 2^5;     % nfft

% data=def_ydat(:,1)-def_ydat(1,1);
data2=data;
L=length(data); fps=120;
[R,dt]     = xcorr(data-mean(data),L,'coeff'); % autocorr
[E,f2] = cpsd(data-mean(data),data2-mean(data2),interval,
   overlap,nfft,fps);
figure(3)
plot(f2,abs(E),'LineWidth',2); xlim([0 5])
xlabel('Frequency (Hz)')
ylabel('CPSD')
xlim([0 5])
%% FFT

% plot(time,pt_data);
% xlabel('Flow Time (Seconds)');
% ylabel('Pixel Value');
% title('Data Plot for Post processing');
% grid on;
%
```